



PHD

## Modelling Hydrogen Storage in Nanoporous Materials for use in Aviation

Sharpe, Jessica

*Award date:*  
2015

*Awarding institution:*  
University of Bath

[Link to publication](#)

### Alternative formats

If you require this document in an alternative format, please contact:  
[openaccess@bath.ac.uk](mailto:openaccess@bath.ac.uk)

Copyright of this thesis rests with the author. Access is subject to the above licence, if given. If no licence is specified above, original content in this thesis is licensed under the terms of the Creative Commons Attribution-NonCommercial-NoDerivs 4.0 International (CC BY-NC-ND 4.0) Licence (<https://creativecommons.org/licenses/by-nc-nd/4.0/>). Any third-party copyright material present remains the property of its respective owner(s) and is licensed under its existing terms.

#### Take down policy

If you consider content within Bath's Research Portal to be in breach of UK law, please contact: [openaccess@bath.ac.uk](mailto:openaccess@bath.ac.uk) with the details. Your claim will be investigated and, where appropriate, the item will be removed from public view as soon as possible.

# **Modelling Hydrogen Storage in Nanoporous Materials for use in Aviation**

Submitted by Jessica Ellen Sharpe

for the degree of Doctor of Philosophy

University of Bath

Centre for Sustainable Chemical Technologies

Department of Chemical Engineering

January 2015

## **COPYRIGHT**

Attention is drawn to the fact that copyright of this thesis rests with the author. A copy of this thesis has been supplied on condition that anyone who consults it is understood to recognise that its copyright rests with the author and that they must not copy it or use material from it except as permitted by law or with the consent of the author

This thesis may be made available for consultation within the University Library and may be photocopied or lent to other libraries for the purposes of consultation.

Signed:



Date: 31/01/15



## Abstract

There is a growing need for new sources of energy due to the rise in global energy demand, the decline in fossil fuels, and the increasing, negative consequences of climate change. Renewable energy resources are sustainable but they are also intermittent, meaning that they cannot supply energy on demand unless it is stored. Hydrogen is one potential chemical method of storing this energy; however, it has a very low energy density per unit volume, meaning that storage in low mass and volume containers can be problematic. One solution is to adsorb hydrogen onto highly porous materials.

This thesis presents an improved methodology for analysing hydrogen adsorbed inside porous materials, and how it can be utilised to determine the potential use of storing hydrogen *via* physisorption for aviation. Preliminary studies are conducted on pressure and temperature dependencies of both the pore volume and the adsorbate density, and a comparison is also made between the utilisation of different Type 1 isotherms for the fractional filling of hydrogen, with the use of the Tóth equation resulting in the best quality of fit to the isotherms overall. The model is verified using inelastic neutron scattering and computer simulations.

The model is then utilised to calculate the amount of hydrogen within a tank containing varying quantities of adsorbent, and comparing this to the amount of hydrogen that can be stored *via* direct compression at the same conditions. This is then expanded to be compared to alternative energy systems, and a preliminary investigation on the use of adsorbed hydrogen within aviation is conducted. The results show hydrogen adsorption to always have a higher energy density than compressed hydrogen up to a certain pressure, and for both to have a comparable energy density to battery storage at certain conditions, but not to standard jet fuels.

## Acknowledgements

The four years spent on my PhD have been four absolutely amazing years of my life. On top of my studies, I have been fortunate enough to have travelled the world and have met some of the best friends that I could have ever asked for.

None of this would ever have been possible if I had not been accepted into the DTC in the first place, so I must thank Tim, Janet and Matt for seeing past my ditsy interview and giving me the opportunity. Thanks must also be given to the DTC for providing me with the funding and constant support over the past four years. The funding was received from the EPSRC through the DTC, but additional funding was given by Airbus Group to specifically support my PhD project.

Not only did Airbus Group provide additional funding, but they also gave support through my industrial supervisor, Agata Godula-Jopek, and by presenting the opportunity and additional funding for an industrial placement for a month at the Airbus site in Paris. The month in Paris was fantastic, even with my huge deficit of the French language, and the experience of working in industry was immensely valued. Thanks must particularly go to Emmanuel Joubert and Bruno Rechain for the support and help that they provided throughout the month.

Paris was not the only internship undertaken throughout my PhD, I was also fortunate enough to spend ten weeks in Australia, working at the University of Queensland in Brisbane. This was yet another incredible opportunity, and thanks must be given to Suresh Bhatia for allowing me this opportunity, and to Amir Rima and to Lang Liu for all of their support.

Of course, my biggest thanks must go to my lead supervisor, Dr Tim Mays, without whom none of this would have been possible. Tim has always encouraged me to make the most out of my PhD, both in and out of research, and I can't think of a single other supervisor who has allowed their students to do half so many of the invaluable opportunities that Tim has encouraged me to do.

Dr Valeska Ting and Dr Nuno Bimbo have always been there for additional support whenever it has been needed. I have greatly enjoyed working closely with both of them, and really appreciate everything that they have done for me. Thanks

must also go to my second supervisor, Dr Andy Burrows, who helped me through the synthesis side of the project and was always there to help when needed.

On the non-academic side of things, I would not have enjoyed my last four years anywhere near as much without the friends that I have made throughout it. To Sarah Abou-Shehada and Lee Burton, all I can say is thank goodness we did not start our four years together as we have ended it – you two are amazing and I will miss you both so much next year. To Patricia, Anyela, Lisa, Rhod, Ben and everyone else that I have met and valued throughout the last four years, we have had some absolutely incredible times. To Katie and Beth, for continuing to be two of the best friends ever.

And finally, to my family – you have always supported every decision that I have made and I could not be where I am today without you.

## Table of contents

Abstract.....	iii
Acknowledgements.....	iv
List of figures.....	ix
List of tables.....	xv
Nomenclature.....	xvi
Dissemination .....	xx
Journal articles .....	xx
Conference and workshop presentations .....	xxi
Poster presentations.....	xxii
Prizes .....	xxiii
Declaration of authorship .....	xxiv
1 Introduction.....	2
1.1 Scope and motivation .....	2
1.2 Thesis structure .....	4
2 Background.....	6
2.1 Global energy .....	8
2.1.1 Impact of the Industrial Revolution .....	8
2.1.2 Energy sources and the environment.....	10
2.2 Energy storage and hydrogen.....	15
2.3 Applications of hydrogen in energy systems.....	25
2.3.1 Introduction.....	25
2.3.2 Hydrogen in aviation.....	25
2.4 The modelling of hydrogen adsorption.....	29
2.5 Aims and objectives .....	37
2.6 Conclusion .....	38
3 Methodology .....	40

3.1	Materials .....	40
3.1.1	TE7 carbon beads .....	41
3.1.2	AX-21 activated carbon .....	42
3.1.3	MIL-101(Cr) .....	43
3.1.4	MIL-53(Al) .....	44
3.1.5	NOTT-101 .....	45
3.1.6	ZIF-8.....	46
3.1.7	Summary.....	46
3.2	Characterisation equipment.....	48
3.2.1	X-ray diffraction (XRD) .....	48
3.2.2	Thermogravimetric analysis (TGA).....	50
3.2.3	Low pressure volumetric gas sorption .....	51
3.2.4	High pressure volumetric gas sorption .....	52
3.2.5	Helium pycnometry.....	53
3.2.6	Inelastic neutron scattering .....	53
3.3	Analysis .....	55
3.3.1	Statistical analysis .....	55
3.3.2	Computer simulations.....	57
4	Results and discussion .....	60
4.1	Development of the initial model.....	63
4.1.1	Density variation of hydrogen within the pores .....	63
4.1.2	Derivation of the density variation model.....	67
4.1.3	Absolute and total hydrogen uptake .....	70
4.1.4	Conclusion .....	71
4.2	Detailed analysis of the density variation model .....	72
4.2.1	A comparison of isotherm equations, $\Theta_A$ .....	72
4.2.2	Pore volume, $V_P$ , dependence on pressure and temperature .....	85

4.2.3	Adsorbate density, $\rho_A$ , dependence on pressure and temperature .	101
4.2.4	Independence of the density variation model with pressure and temperature .....	108
4.2.5	Conclusion.....	114
4.3	Verification of the density variation model.....	116
4.3.1	Inelastic neutron scattering.....	117
4.3.2	Computer simulations.....	121
4.3.3	Conclusion.....	125
4.4	Comparison of hydrogen adsorption vs. compression in a tank.....	126
4.4.1	History of design curves .....	126
4.4.2	Derivation of the new equation used for design curves .....	127
4.4.3	Design curves per unit volume and per unit mass.....	130
4.4.4	Adsorption vs. compression .....	131
4.4.5	Conclusion.....	136
4.5	Hydrogen adsorption in aviation.....	137
4.5.1	Comparison to alternative energy systems .....	137
4.5.2	Cryo-charging of hydrogen tanks .....	139
4.5.3	Physisorption of hydrogen in aviation.....	143
4.5.4	Conclusion.....	144
5	Concluding remarks .....	146
5.1	Conclusions .....	146
5.2	Future work.....	149
6	References .....	153
	Supplementary information (in electronic format).....	176

## List of figures

Figure 2.1 – A flow chart representing the material discussed in the background..	7
Figure 2.2 – Growth in global annual energy consumption with time.....	8
Figure 2.3 – Growth in world population from 1750 to the present, and expected growth to 2050 using a medium variant. ....	9
Figure 2.4 – Total global energy consumption by fuel type, 1990 – 2014.....	11
Figure 2.5 – Land temperature 10-year running average.....	13
Figure 2.6 – Energy per unit mass and per unit volume for different fuels. ....	16
Figure 2.7 – An example of a MOF, IRMOF-16, with the metal centres (red) linked with organic linkers (blue), and the yellow balls depicting the space available for adsorption. ....	20
Figure 2.8 – An illustration of an activated carbon particle.....	20
Figure 2.9 – A conceptual diagram of a (A) single-walled carbon nanotube and a (B) multi-walled carbon nanotube.. ....	21
Figure 2.10 – An illustration of a synthetic route of a CDC using high-temperature chlorination of a metal carbide.. ....	21
Figure 2.11 – An illustration of pillared graphene.....	22
Figure 2.12 – The framework structure of the zeolite ZSM-5. ....	23
Figure 2.13 – A molecular model of an example PIM structure, PIM-1.....	23
Figure 2.14 – An illustration of adsorption and desorption of A onto a surface of molecules, M.....	30
Figure 2.15 – An illustration of Henry’s law and the Henry pressure.....	32
Figure 2.16 – Types of physisorption isotherms.....	33
Figure 2.17 – An illustration of the excess and absolute quantities of hydrogen...	34
Figure 2.18 – The hydrogen density profile within a pore assumed in in the initial model. ....	35
Figure 3.1 – (Left) The structure of MIL-101(Cr), (right) the inorganic subunit. ....	43
Figure 3.2 – (Left) The structure of MIL-53(Al), (right) the inorganic subunit. ....	44
Figure 3.3 – Representation of the breathing phenomena observed in MIL-53(Al). A large pore, (a), to a narrow pore, (b), transition. ....	45
Figure 3.4 – (Left) the ligand in NOTT-101 and (middle) the space-filling representation of NOTT-101.. ....	45

Figure 3.5 – (Left) the single crystal x-ray structure of ZIF-8, and (right) the largest cage in ZIF-8.....	46
Figure 3.6– An illustration of Bragg’s Law.....	48
Figure 3.7 – XRD patterns of MIL-101(Cr) synthesised in Bath (red), and from literature (black). ....	49
Figure 3.8 – The XRD pattern for MIL-101(Cr) at varying pressures and temperatures.....	50
Figure 3.9 – TGA plot of MIL-101(Cr) with increasing temperature under a nitrogen atmosphere, with a ramp rate of 5 °C min <sup>-1</sup> .....	51
Figure 3.10 – Screen shots from the ASAP showing the BET data for MIL-101(Cr). ....	52
Figure 3.11 – Hydrogen isotherms measured on the HTP-1 for MIL-101(Cr). ....	53
Figure 3.12 – An illustration of the 3-point hydrogen model.....	57
Figure 4.1 – A flow chart showing the different sections within the results and discussion chapter. ....	62
Figure 4.2 – The density profile of hydrogen at 2 MPa and 77 K inside slit pores of infinite width walls of pure graphite with different pore widths.....	64
Figure 4.3 – An illustration of a density profile of hydrogen inside a large pore. ...	65
Figure 4.4 – The density profile of hydrogen in a pore, utilised for the new model. ....	65
Figure 4.5 – An overview of the system, and the nomenclature used for the new model. ....	66
Figure 4.6 – The excess hydrogen uptake with pressure at different temperatures for the TE7 carbon beads.....	69
Figure 4.7 – A comparison of the quality of the fit of the initial and DV models on the TE7 carbon bead isotherms at various temperatures using the Tóth isotherm equation. ....	69
Figure 4.8 – A comparison of the total, absolute, and excess quantities of hydrogen within the TE7 carbon beads at 77 K. ....	71
Figure 4.9 – A continuous uniform distribution with respect to the heterogeneity parameter, <i>b</i> .....	77
Figure 4.10 – Individual fits to the TE7 carbon bead isotherms at different temperatures using the DV model with the Tóth isotherm equation.....	80

Figure 4.11 – Regular residuals for the Tóth fit on the 89 K and 120 K isotherms from the TE7 carbon beads. ....	81
Figure 4.12 - The dependence of (a) the pore volume and (b) the adsorbate density on temperature for the Tóth isotherm equation on the TE7 carbon beads. ....	82
Figure 4.13 - Global Tóth fit to all of the isotherms from the TE7 carbon beads... ..	83
Figure 4.14 - The cumulative RMSR values for global fits of each isotherm equation within the DV model to each material. ....	84
Figure 4.15 - The RMSR values for global fits of each isotherm equation within the DV model to each material. ....	84
Figure 4.16 - A diagram determining the pressures and temperatures required for the pores of MIL-53 to be in narrow form and large form. ....	86
Figure 4.17 - A representation of the potential uniform distribution dependence of pore volume on pressure and temperature, where $X$ could represent either pressure or temperature. ....	87
Figure 4.18 - The low temperature region of the MIL-53 isotherms measured on the HTP-1, indicating potential breathing of the material with hydrogen adsorption. ....	88
Figure 4.19 - The different XRD powder patterns for MIL-53(Al) with large pores (red line, containing water) and narrow pores (blue line, empty), as measured by Dr. Dongmei Jiang at the University of Bath. ....	88
Figure 4.20 – The XRD patterns of MIL-101 at a variety of hydrogen pressures and temperatures. ....	89
Figure 4.21 – The largest peak shift in the quick scans of MIL-53. ....	90
Figure 4.22 – The temperatures and pressures used for the long scan XRD experiments on MIL-53. ....	90
Figure 4.23 – The XRD powder patterns from the MIL-53 long scans. ....	92
Figure 4.24 - The initial pore volume dependencies on temperature for the TE7 carbon beads and MIL-53, assuming a linear-type dependence on pore volume with pressure. ....	95
Figure 4.25 - The dependencies of alpha on temperature for the TE7 carbon beads and MIL-53, assuming a linear-type dependence on pore volume with pressure. ....	95

Figure 4.26 – The predicted linear pore volume dependence on pressure using the values provided from the fitting. ....96

Figure 4.27 - The initial pore volume dependencies on temperature for the TE7 carbon beads and MIL-53, assuming a power-type dependence on pore volume with pressure.....97

Figure 4.28 - The alpha dependencies on temperature for the TE7 carbon beads and MIL-53, assuming a power-type dependence on pore volume with pressure.98

Figure 4.29 - The predicted power pore volume dependence on pressure from the values provided from the fitting. .... 99

Figure 4.30 - The pore volume dependence on temperature for the TE7 carbon beads and MIL-53. .... 100

Figure 4.31 - An illustration of the hydrogen inside a pore with (a) a constant density with increased pressure and decreased temperature and (b) an increased density..... 101

Figure 4.32 – The density profile of hydrogen within a 0.7 nm pore at different pressures and temperatures. .... 101

Figure 4.33 - The initial adsorbate density dependencies on temperature for the TE7 carbon beads and MIL-101, assuming a linear-type dependence on adsorbate density with pressure. .... 104

Figure 4.34 - The dependencies of alpha on temperature for the TE7 carbon beads and MIL-101, assuming a linear-type dependence on adsorbate density with pressure..... 104

Figure 4.35 - The predicted linear adsorbate density dependence on pressure from the values provided from the fitting. .... 105

Figure 4.36 - The predicted linear adsorbate density dependence on pressure from the values provided from the fitting for AX-21, MIL-53, NOTT-101 and ZIF-8..... 106

Figure 4.37 - The pore volume values from fitting the DV model to each adsorbent assuming a constant adsorbate density (black), and assuming a linear dependence of adsorbate density with pressure (red). .... 107

Figure 4.38 - The adsorbate density dependence on temperature, keeping a constant pore volume..... 108

Figure 4.39 - Values for the affinity parameter,  $b$ , without y-error (top left), with y-error from the initial fits to calculate  $b$  (bottom left) and the values from the fitting (bottom right)..... 110

Figure 4.40 - Trends in the heterogeneity parameter dependence on temperature for each material (left) and for each material except MIL-53 (right).....	112
Figure 4.41 - The dependence of the parameters within the compressibility factor with temperature for each adsorbent. ....	113
Figure 4.42 - A comparison between the amount of densified hydrogen detected by INS (red squares), and calculated using the DV model for the TE7 77 K isotherm (blue line).. ....	119
Figure 4.43 – INS spectra, ascending pressures going from lowest to highest intensity in the main panel, and zoomed in the inset (B). (A) INS elastic spectrum at the lowest pressure [220]. ....	120
Figure 4.44 – The density of solid para-hydrogen at 4 K. Data taken from Silvera [206]. ....	121
Figure 4.45 – An illustration of the simulation box when only assuming one layer of carbon either side of the pore. ....	123
Figure 4.46 - The total hydrogen uptake calculated from simulations (“sim” in the legend), assuming only one layer of graphene either side of the pore for the calculation, and from modelling to experimental isotherms (“exp” in the legend). ....	124
Figure 4.47 – Representation of the nomenclature used to calculate the amount of hydrogen in a tank containing adsorbent. ....	128
Figure 4.48 - The energy density (left) and the specific energy (right) in a tank filled with varying quantities of TE7 carbon beads at different temperatures and pressures. ....	133
Figure 4.49 – The break-even pressures for TE7 carbon beads at varying temperatures.....	134
Figure 4.50 – The break-even pressures for a range of materials. ....	135
Figure 4.51 – The design curve for the TE7 carbon beads at 89 K, highlighting the different pressures that would be required to store $0.025 \text{ g cm}^{-3}$ in a tank containing different amounts of adsorbent. ....	136
Figure 4.52 - A comparison of potential aviation energy technologies per unit volume (left) and per unit mass (right), compared to hydrogen storage in a tank containing varying quantities of TE7 carbon beads at 89 K. ....	138
Figure 4.53 - (Left) The energy density and specific energy of various energy storage technologies. The adsorbed hydrogen range contains the same data	

observed in (Right), which is zoomed in to the various hydrogen adsorption materials at 20 MPa in a tank half filled with adsorbent. .... 139

Figure 4.54 – A representation of the nomenclature used to calculate the increase in pressure when allowing an increase in temperature in a tank containing an adsorbent. .... 140

## List of tables

Table 2.1 – Prototypes and demonstrations of hydrogen powered aircraft.....	27
Table 3.1 – A summary of the key parameters for each of the six materials used throughout the thesis. ....	47
Table 4.1 – A summary of the isotherm equations, the surface energy distribution, the type of adsorbent-adsorbate interaction, and the number of parameters in each equation.....	78
Table 4.2 - The different functions chosen to represent the pore volume, and the number of parameters in each. ....	93
Table 4.3 - RMSR values using different pore volume dependencies of pressure on the TE7 carbon beads and MIL-53 to 3 decimal places.....	94
Table 4.4 - The different functions chosen to represent the adsorbate density as a function of pressure. ....	102
Table 4.5 - RMSR values using different adsorbate density dependencies of pressure on the TE7 carbon beads and MIL-101 to 3 decimal places. ....	103
Table 4.6 - The heat of adsorption observed in each material as calculated from the Arrhenius relationship between the affinity parameter, $b$ , and temperature..	111
Table 4.7 - The final pressure reached in a tank charged with hydrogen at 77 K and 0.1 MPa following a rise in temperature to 295 K, the corresponding quantity of hydrogen per unit volume within the tank, and the pressure required to store that same quantity of hydrogen per unit volume <i>via</i> compression in a tank containing no adsorbent at 295 K..	141
Table 4.8 - The initial pressure required in a tank filled with hydrogen at 77 K to produce a pressure of 70 MPa following a rise in temperature to 295 K, the corresponding quantity of hydrogen per unit volume within the tank, and the pressure required to store that same quantity of hydrogen per unit volume <i>via</i> compression in a tank containing no adsorbent at 295 K.....	142
Table 4.9 - The initial and final pressures required in a tank at 77 K and 295 K respectively in order to hold $0.04 \text{ g cm}^{-3}$ hydrogen, and the pressure required to store that same quantity of hydrogen per unit volume <i>via</i> compression in a tank containing no adsorbent at 295 K. ....	143

# Nomenclature

## Acronyms

MOF	metal-organic framework
PIM	polymer of intrinsic microporosity
GDP	gross domestic product
OECD	Organisation for Economic Co-operation and Development
EIA	Energy Information Administration
RF	radiative forcing
DOE	Department of Energy
IUPAC	International Union of Pure and Applied Chemistry
CDC	carbide-derived carbon
HICE	hydrogen internal combustion engine
PEMFC	proton exchange membrane fuel cell
SOFC	solid oxide fuel cell
AFC	alkaline fuel cell
PAFC	phosphoric acid fuel cell
MCFC	molten carbonate fuel cell
BET	Brunauer, Emmett and Teller
DFT	Density Functional Theory
DRK	Dubinin-Radushkevich-Kaganer
ZIF	zeolitic imidazolate framework
MIL	Matériaux de l'Institut Lavoisier
PXRD	powder X-ray diffraction
IGA	Intelligent Gravimetric Analyser
ASAP	accelerated surface area and porosimetry
ESRF	European Synchrotron and Radiation Facility
RMSR	root mean square residual
GCMC	Grand Canonical Monte Carlo
NIST	National Institute of Standards and Technology
DV	density variation
DA	Dubinin-Astakhov
DR	Dubinin-Radushkevich

XRD	X-ray diffraction
INS	inelastic neutron scattering
wt%	weight percent

### **Nomenclature consistent throughout the thesis**

$\Theta_A$	coverage of adsorbed molecules on the surface, also known as the fractional filling	-
$P$	pressure	MPa
$T$	temperature	K
$R$	molar gas constant	MPa cm <sup>3</sup> K <sup>-1</sup> mol <sup>-1</sup>
$\Delta H$	enthalpy of adsorption	kJ mol <sup>-1</sup>
$w$	specific work done	kJ mol <sup>-1</sup>
$V$	volume	cm <sup>3</sup>
$Z$	compressibility factor	-
$M$	molar mass	g mol <sup>-1</sup>
$m_E$	excess quantity of hydrogen	g or wt%
$m_A$	total amount of hydrogen in the adsorbate (absolute)	g or wt%
$m_A^{\max}$	maximum amount of hydrogen able to be adsorbed	g or wt%
$m_B$	bulk hydrogen	g or wt%
$m_S$	mass of the adsorbent	g
$\rho_B$	bulk density	g cm <sup>-3</sup>
$\rho_S$	skeletal density	g cm <sup>-3</sup>
$\rho_A$	adsorbate density	g cm <sup>-3</sup>
$v_P$	specific open pore volume	cm <sup>3</sup> g <sup>-1</sup>
$a_Z$	parameter for the compressibility factor	MPa <sup>-1</sup>
$b_Z$	parameter for the compressibility factor	MPa <sup>-2</sup>
$c_Z$	parameter for the compressibility factor	MPa <sup>-1</sup>
$d_Z$	parameter for the compressibility factor	MPa <sup>-2</sup>

### **Nomenclature for the new model**

$m_T$	total amount of hydrogen in the pore	wt%
$m_{B(A)}$	bulk hydrogen within the adsorbate	wt%

$m_{B(P)}$	bulk hydrogen within the pore	wt%
$V_C$	specific control volume	$\text{cm}^3 \text{g}^{-1}$
$V_S$	specific adsorbent volume	$\text{cm}^3 \text{g}^{-1}$
$V_A$	specific adsorbate volume	$\text{cm}^3 \text{g}^{-1}$
$V_{B(P)}$	specific bulk adsorptive volume	$\text{cm}^3 \text{g}^{-1}$

### **Nomenclature for the design curves**

$m_H$	mass of the hydrogen	g
$V_C$	container volume	$\text{cm}^3$
$V_B$	bulk volume	$\text{cm}^3$
$V_{BP}$	volume of bulk in the pore	$\text{cm}^3$
$V_{BI}$	volume of interstitial bulk	$\text{cm}^3$
$V_{BC}$	volume of bulk outside of the area of the adsorbent	$\text{cm}^3$
$V_D$	displaced volume	$\text{cm}^3$
$V_T$	total volume of adsorbent	$\text{cm}^3$
$V_F$	volume of tank containing adsorbent	$\text{cm}^3$
$V_P$	pore volume	$\text{cm}^3$
$V_A$	adsorbate volume	$\text{cm}^3$
$V_S$	skeletal volume	$\text{cm}^3$
$f$	fill factor	-
$x$	packing factor of adsorbent	-
$m_H^0$	mass of hydrogen in a tank empty of adsorbent	g
$P_B$	break-even pressure	MPa
$m_W$	mass of the contents of the tank	g
$E_H$	energy available from the hydrogen	MJ

### **Nomenclature specific for the isotherm equations**

$b$	affinity parameter	$\text{MPa}^{-1}$
$c$	heterogeneity parameter in the Tóth and Jovanović-Freundlich equations	-
$A$	pre-exponential factor	$\text{MPa}^{-1}$
$Q$	enthalpic parameter	$\text{kJ mol}^{-1}$
$m$	heterogeneity parameter in the Sips and Freundlich	-

	equations	
$k$	parameter within the Freundlich equation	MPa <sup>-1</sup>
$q$	heterogeneity parameter in the Generalised-Freundlich equation	-
$\alpha$	enthalpic parameter within the Dubinin-Astskhov equation	J mol <sup>-1</sup>
$\beta$	entropic parameter within the Dubinin-Astskhov equation	J mol <sup>-1</sup> K <sup>-1</sup>
$P_0$	vapour pressure	MPa
$m$	heterogeneity parameter in the Dubinin-Astskhov equation	-
$P_c$	critical pressure	MPa
$T_c$	critical temperature	K

**Nomenclature specific for the quality of fit**

RMSR	root mean square residual	wt%
RSS, $\chi^2$	residual sum of squares	(wt%) <sup>2</sup>
$R^2$	a method of quality of fit	-
$w_i$	weighted fitting	-
$y_i$	data value	wt%
$\hat{y}_i$	function value	wt%
DOF	degrees of freedom	-
$n$	number of data points	-
$p$	number of parameters	-
TSS	total sum of squares	(wt%) <sup>2</sup>
$\bar{y}_i$	series mean	-
$j$	particular isotherm chosen when fitting to multiple isotherms	-
$m$	number of isotherms when fitting to multiple isotherms	-
$n$	total number of data points when fitting to multiple isotherms	-

## Dissemination

Much of the work presented in this thesis has been disseminated *via* posters, oral presentations and journal articles.

### ***Journal articles***

The author has participated in five manuscripts, three of which are published (1, 2 and 3), one is accepted for publication (4), and one is about to be submitted (5). Publication 1 highlights the main results in the results and discussion Sections 0 and 4.2 of this thesis. Publication 2 introduces the work conducted in the results and discussion Section 4.4. Publication 3 was about the isosteric enthalpies of hydrogen adsorption, of which the author was involved in but which was not fully relevant to the results and discussion presented within this thesis. Publication 4 highlights the work shown in results and discussion Sections 4.4 and 4.5, and publication 5 is related to the inelastic neutron scattering work shown in results and discussion Section 4.3.

1. Sharpe, J. E.; Bimbo, N.; Ting, V. P.; Burrows, A. D.; Jiang, D.; Mays, T. J., Supercritical Hydrogen Adsorption in Nanostructured Solids with Hydrogen Density Variation in Pores. *Adsorption* 2013, 19 (2-4) 643-652.
2. Bimbo, N.; Ting, V. P.; Sharpe, J. E.; Mays, T. J., Analysis of Optimal Conditions for Adsorptive Hydrogen Storage in Microporous Solids. *Colloid and Surfaces A: Physicochemical and Engineering Aspects* 2013, 437, 113-119.
3. Bimbo, N.; Sharpe, J. E.; Ting, V. P.; Noguera Diaz, A.; Mays, T., Isosteric Enthalpies for Hydrogen Adsorbed on Nanoporous Materials at High Pressures. *Adsorption* 2013, 20 (2-3), 373-384.
4. Sharpe, J. E.; Bimbo, N.; Ting, V. P.; Mars, B.; Joubert, E.; Mays, T. J., Modelling the Potential of Adsorbed Hydrogen for use in Aviation. *Microporous and Mesoporous Materials* (accepted).
5. Ting, V. P.; Ramirez-Cuesta, A. J.; Bimbo, N.; Sharpe, J. E.; Mays, T. J., Direct Evidence for Accumulation of Solid-like H<sub>2</sub> in a Microporous Hydrogen Storage Material. *Nature Communications* (to be submitted).

## ***Conference and workshop presentations***

The author has participated in a variety of international conferences and workshops and has been accepted to present a significant amount of the work mentioned throughout the thesis, as well as being involved in similar studies that have been presented. The following are listed in chronological order, and the presenter is underlined.

1. Visit to Airbus Group, Munich, Germany, February 2012.  
*Hydrogen storage in nanoporous materials for aerospace applications.*  
Sharpe, J. E.; Burrows, A. D.; Mays, T. J.
2. Sixth International Workshop on the Characterization of Porous Materials, Delray Beach, Florida, USA, April-May 2012.  
*Novel evaluation of nanoporous hydrogen storage materials using adsorption, nuclear magnetic resonance and inelastic neutron scattering.*  
N. Bimbo, V.P.Ting, R.J.Anderson, A.J. Ramirez-Cuesta, J. Sharpe, A. Kleinhammes, Y. Wu and T.J. Mays.
3. The Eighth International Symposium of the Effects of Surface Heterogeneity in Adsorption and Catalysis on Solids ISSHAC-8, Krakow, Poland, August 2012.  
*Heterogeneity of supercritical hydrogen adsorption in nanostructured solids.*  
Sharpe, J. E.; Ting, V. P.; Bimbo, N.; Burrows, A. D.; Jiang, D.; Godula-Jopek, A.; Mays, T. J.
4. Visit to Airbus Group, Glasgow, UK, March 2013.  
*Modelling of supercritical hydrogen adsorption in nanostructured solids.*  
Sharpe, J. E.; Burrows, A. D.; Godula-Jopek, A.; Mays, T. J.
5. Visit to Airbus Group, Paris, France, April 2013.  
*Modelling of supercritical hydrogen adsorption in nanostructured solids.*  
Sharpe, J. E.; Burrows, A. D.; Godula-Jopek, A.; Mays, T. J.
6. Centre for Sustainable Chemical Technologies, Summer Showcase, Bath, UK, September 2013.  
*Modelling hydrogen adsorption for aviation.*  
Sharpe, J. E.; Burrows, A. D.; Godula-Jopek, A.; Mays, T. J.
7. Visit to Airbus Group, Glasgow, UK, November 2013.  
*Modelling hydrogen adsorption for aviation.*

Sharpe, J. E.; Burrows, A. D.; Godula-Jopek, A.; Mays, T. J.

8. The Hydrogen & Fuel Cell research hub *H<sub>2</sub>FC* Supergen conference, Birmingham, UK, 2013.

*Modelling hydrogen adsorption for aviation.*

Sharpe, J. E.; Burrows, A. D.; Godula-Jopek, A.; Mays, T. J.

9. Tenth International Symposium on the Characterisation of Porous Solids, COPS-X, Granada, Spain, May 2014.

*Modelling hydrogen adsorption for aviation.*

Sharpe, J. E.; Burrows, A. D.; Godula-Jopek, A.; Mays, T. J.

### ***Poster presentations***

The author has also presented, or co-authored, a significant number of poster presentations. The following are listed in chronological order, and the presenter is underlined.

1. Sixth International Workshop for the Characterisation of Porous Materials, CPM-6, Delray Beach, FL, USA, April 2012.

*Metal-organic framework materials for hydrogen storage in aerospace applications.*

Ahmet, I.; Sharpe, J. E.; Ting, V. P.; Bimbo, N.; Burrows, A. D.; Godula-Jopek, A.; Mays, T. J.

2. Airbus Group PhD Student Showcase, May 2012.

*Hydrogen storage in nanoporous materials for aerospace applications.*

Sharpe, J. E.; Burrows, A. D.; Godula-Jopek, A.; Mays, T. J.

3. Centre for Sustainable Chemical Technologies, Summer Showcase, Bath, UK, July 2012.

*Hydrogen storage in nanoporous materials for aerospace applications.*

Sharpe, J. E.; Burrows, A. D.; Godula-Jopek, A.; Mays, T. J.

4. ChemEngDay 2013, London, UK, March 2013.

*Hydrogen Energy Research in the Department of Chemical Engineering, University of Bath, UK.*

Bimbo, N.; Owens, S.; Sharpe, J. E.; Noguera Diaz, A.; Rushworth, A.; Smith, M.; Berry, M.; Hayes, P.; Mays, T. J.

5. 11<sup>th</sup> International Conference on the Fundamentals of Adsorption, FOA-11, Baltimore, USA, May 2013.  
*A new generalised model for supercritical sorption in nanoporous materials.*  
Sharpe, J. E.; Bimbo, N.; Noguera Diaz, A.; Ting, V. P.; Rushworth, A.; Mays, T. J.
6. UK Energy Research Centre Summer School, Warwick, July 2013.  
*The modelling of hydrogen storage in nanoporous materials.*  
Sharpe, J. E., Bimbo, N.; Ting, V. P.; Mays, T. J.
7. The Hydrogen & Fuel Cell research hub H2FC Supergen conference, Birmingham, UK, 2013.  
*Enthalpies of adsorption of hydrogen in carbons and metal-organic frameworks: refining the analysis for improving the design of adsorptive storage systems.*  
Bimbo, N.; Sharpe, J. E.; Noguera Diaz, A.; Physick, A.; Ting, V. P.; Mays, T. J.
8. ChemEngDay 2014, Manchester, UK, April 2014.  
*Fuel Gas Storage: The Challenge of Hydrogen.*  
Bimbo, N.; Sharpe, J. E.; Noguera Diaz, A.; Physick, A.; Holyfield, L.; Rowlandson, J.; Xu, W.; Ladha, A.; Ting, V. P.; Mays, T. J.
9. ChemEngDay 2014, Manchester, UK, April 2014.  
*Fuel Gas Storage: The Challenge of Methane.*  
Pugsley, A.; Bimbo, N.; Physick, A.; Noguera Diaz, A.; Sharpe, J. E.; Ting, V. P.; Mays, T. J.
10. Centre for Sustainable Chemical Technologies, Summer Showcase, Bath, UK, July July 2014.  
*Modelling hydrogen storage in nanoporous materials for aviation.*  
Sharpe, J. E.; Burrows, A. D.; Mays, T. J.

### **Prizes**

The author has won two prizes for presentations. The first was a poster prize presentation at the Airbus Group Student Showcase in May 2012. The second was first place for an oral presentation in the Engineering Faculty Student Showcase at the University of Bath in April 2013.

## **Declaration of authorship**

The author was funded through the Doctoral Training Centre in the Centre for Sustainable Chemical Technologies at the University of Bath, by the Engineering and Physical Sciences Research Council (EPSRC).

The worked presented in this thesis, except where otherwise noted, was done by the author with supervision and guidance from her academic supervisor, Dr Timothy J Mays, Head of Department in the Department of Chemical Engineering at the University of Bath.

Most of the work reported in this thesis has been published in journal articles and presented at conferences, as indicated in the dissemination section.

## **Chapter One**

### **Introduction**

# 1 Introduction

## 1.1 Scope and motivation

As a consequence of population increase and the growth in worldwide gross domestic product (GDP), there has been an enormous rise in global energy demand. Accompanying this increase in energy demand is a need for new, cleaner sources of energy due to the decline in fossil fuel reserves, and the increase in climate change. Aviation is one particular industry within which demand is constantly rising; the current fuels used will eventually run out, and the emissions are required to be reduced as many are released directly into the upper atmosphere causing an increase in radiative forcing. Renewable sources of energy, for example wind power, are one potential solution for this problem; however they do not supply a stored form of energy, thus the energy produced needs to be stored.

Hydrogen shows great potential as an energy store; it is the most abundant element in the universe, has the highest energy per unit mass of any chemical fuel, and only water is produced as a by-product when releasing the energy *via* a fuel cell. However, there are currently two major issues with using hydrogen as an energy store; the lack of a cheap, sustainable method for the production of molecular hydrogen, and the difficulty of storage at high densities due to hydrogen's very low energy per unit volume. Storage can be achieved *via* a number of processes: compression, liquefaction, chemisorption or physisorption. Compression and liquefaction are the current state of the art methods but they require unfavourable conditions, high pressures (70 MPa) and low temperatures (~20 K) respectively, and they do not increase the density to a high enough value to be competitive with current transport fuels. Chemisorption and physisorption are both solid state methods of storage; chemisorption involves chemically absorbing the hydrogen into a material, and physisorption encompasses physically adsorbing the hydrogen into the pores of a material. Physisorption is a very promising method of storing hydrogen, as it only requires a small energy input to discharge the hydrogen back out of the material. However, because physisorption only forms weak interactions between the hydrogen and the material, low temperatures within the range of ~77 K are required to store large quantities of hydrogen.

There are many different nanoporous materials that can be used for physisorption of hydrogen, including metal-organic frameworks (MOFs), zeolites, activated carbons, and polymers of intrinsic microporosity (PIMs). Modelling these systems is very important for two main reasons. Firstly, to calculate the total amount of hydrogen within the system, a quantity which cannot easily be measured experimentally. Secondly to better understand the fundamentals of the hydrogen adsorption process, in order to try to improve the design of the nanoporous materials which are synthesised for this, for example by finding the optimum pore size. The models that are used for these purposes are required to exist in terms of the excess amount of hydrogen, as this is the quantity that is measured experimentally. The excess amount of hydrogen refers to the additional amount of hydrogen in the pore of a material as a result of the interactions between the hydrogen and the surface of the material. The basic model used in the literature assumes a single hydrogen density profile within the pore.

## **1.2 Thesis structure**

Chapter 2 of this thesis consists of a detailed study of the background of the project *via* a critical assessment of the literature, including the motivation behind the work, the alternative solutions to the problem in hand, and other relevant research that has been conducted in the field. This chapter will be concluded with the aims and objectives of the work presented within the report, highlighting what was desired to be achieved throughout. A methodology chapter will follow, which includes details about the materials that were used throughout the study, as well as the characterisation and analysis techniques utilised. Subsequently, Chapter 4 consists of the results and discussion, which comprises the bulk of the thesis and details the work completed, the results obtained, and a detailed analysis of the results. The results and discussion chapter is split into five sections. Within Section 4.1, a development of the basic model used within the literature is presented, introducing a more complex density profile within the pore. The developed model, known as the density variation model or DV model for short, is compared to the original model, and a derivation of the absolute and total quantities of hydrogen is conducted. Section 4.2 expands the DV model in more detail and focusses on the unknown parameters - such as the pore volume, the adsorbate density and the fractional filling term - in order to attempt to improve the model, and to potentially determine more about how the hydrogen adsorbs within the pores of materials. Section 4.3 focusses on the verification of the DV model by comparing the absolute and total quantities of hydrogen calculated using the model to both inelastic neutron scattering results as well as computer simulations. Section 4.4 utilises the DV model to create a direct comparison between the amount of hydrogen stored in a tank *via* adsorption and *via* direct compression, and Section 4.5 focusses the work conducted within Section 4.4 to the use of hydrogen in aviation. This chapter is succeeded by concluding remarks, which comprises the conclusions and the future work.

## **Chapter Two**

### **Background**

## **2 Background**

This chapter gives an introduction to global energy from the 18<sup>th</sup> century through to the present, and introduces the role that hydrogen could have in future global energy scenarios. Hydrogen is then discussed in more detail, focussing on the storage of hydrogen and the types of materials that could be used for this application. The use of hydrogen in aviation is also described in detail, followed by an introduction to the modelling of hydrogen storage. This is highlighted in Figure 2.1.

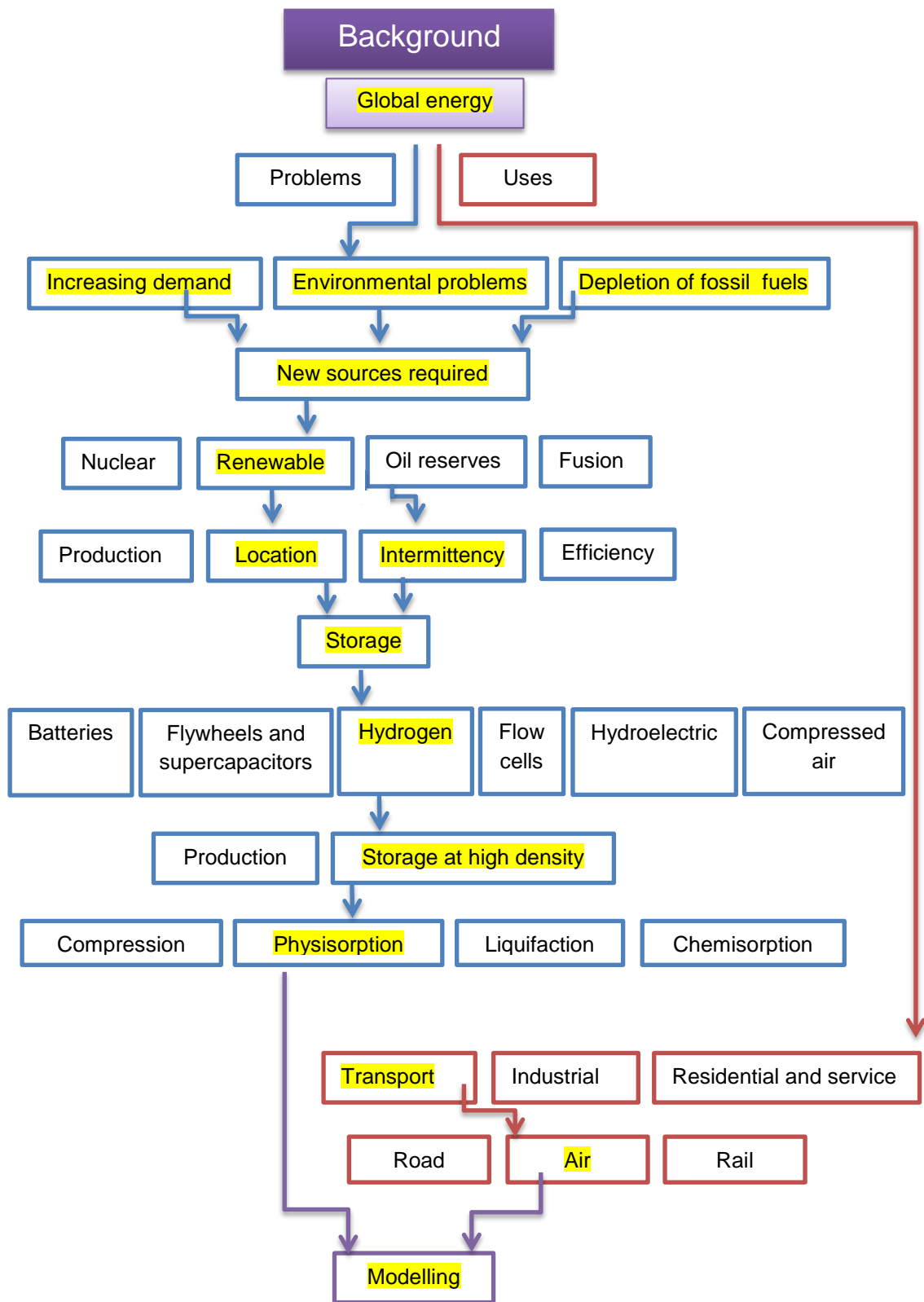
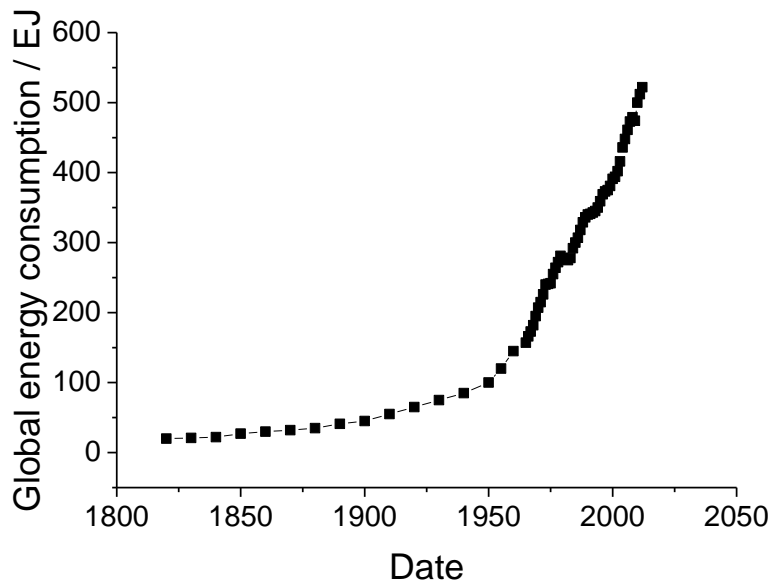


Figure 2.1 – A flow chart representing the material discussed in the background. The highlighted boxes and arrows show the routes that are taken throughout the background study.

## 2.1 Global energy

### 2.1.1 Impact of the Industrial Revolution

The Industrial Revolution of the 18<sup>th</sup> and 19<sup>th</sup> centuries in the United Kingdom, Western Europe, North America and Japan marked an enormous transformation in people's lifestyles. The major sources of energy changed from biomass and muscle power to coal and steam power, thus more energy was able to be easily exploited, consequently increasing the energy use per capita. By the start of the 20<sup>th</sup> century, petroleum and natural gas were also utilised for energy, driving this trend even further. In 2008, nearly 80 GJ of annual energy consumption per capita had been reached, doubling that from 1750 [1], resulting in a huge increase in global energy consumption (Figure 2.2).



**Figure 2.2 – Growth in global energy consumption with time. Lines are drawn to guide the eye. EJ stands for exajoule ( $\times 10^{18}$  joules). Data from [2, 3].**

Another indirect consequence of the industrial revolution was an increase in population, Figure 2.3. The global population in 1750, before the industrial revolution, was estimated from the U.S. Census Bureau to be approximately 790 million, and this has now risen to over seven billion [4, 5]. The majority of this growth (4.5 billion) has occurred since 1950, subsequent to the industrial revolution, and global population is expected to keep increasing to reach approximately nine billion by 2050 [6].

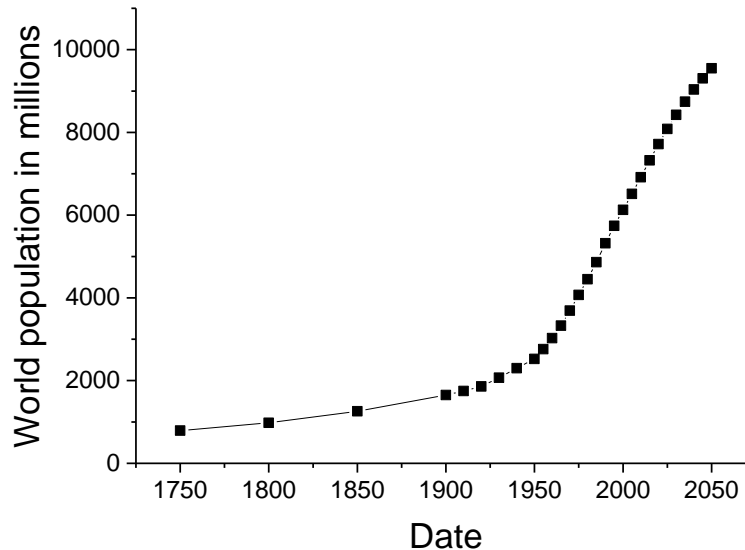


**Figure 2.3 – Growth in world population from 1750 to the present, and expected growth to 2050 using a medium variant. Data from [4, 5, 6].**

This population increase was largely due to the decline in the death rate, which in turn was due to the rise in living standards, a consequence of the industrial revolution, also recognised by increased gross domestic product (GDP) [7]. GDP accounts for many different aspects, such as health care, income, availability of food and educational standards; and, to date, the World Bank has observed a global increase in GDP of over 40 times its 1960 value alone [1].

Assuming an energy consumption per capita of 80 GJ, the expected population growth of approximately two billion people in the next 36 years would require an extra 160 billion GJ of energy per year. However, this value relies upon the energy consumption per capita remaining constant. This is a very unlikely scenario due to the large alteration in the global distribution of wealth as a result of countries involved in the industrial revolution exploiting the available energy to mass produce goods that they sold worldwide. This, along with the many great famines of the 19<sup>th</sup> century, led to a large economic gap between developed and non-developed countries, also now referred to as Organisation for Economic Co-operation and Development countries (OECD) and non-OECD countries respectively [8]. In 2005, OECD countries accounted for 24 % of the population, and yet consumed 65 % of the energy supply [9]. Because of this, it is expected that non-OECD countries will be the major cause of increased energy consumption in the coming years as the national economies in OECD countries

are already mature. The US Energy Information Administration (EIA) has predicted energy use in non-OECD countries to increase by 90 %, but only 17 % for OECD countries [10]. This means that the energy demand per capita is not going to remain steady, but is expected to rise dramatically.

To summarise, the industrial revolution has resulted in more energy becoming easily accessible in OECD countries, to an increased population with a larger demand of energy per capita. This trend is also expected to occur for non-OECD countries in the coming years, resulting in a continuation of the increase in global energy demand. All of this shows that either people's lifestyles are going to have to change radically in order to cope with using less energy, or else the energy supply will need to be dramatically increased in the near future; but most probably a combination of the two.

### **2.1.2 Energy sources and the environment**

In 2010, approximately 84 % of the global energy consumption was provided by fossil fuels (coal, oil and natural gas), amounting to over 460 EJ (Figure 2.4) [10]. Fossil fuels are organic remnants that have been decomposed in the Earth's crust for millions of years. They are currently cheap, widely available, have a high energy density, are simple to transport, and are easy to convert into other forms of energy, such as into heat *via* combustion [11]. However, fossil fuels are non-renewable sources of energy, and the reserves are depleting.

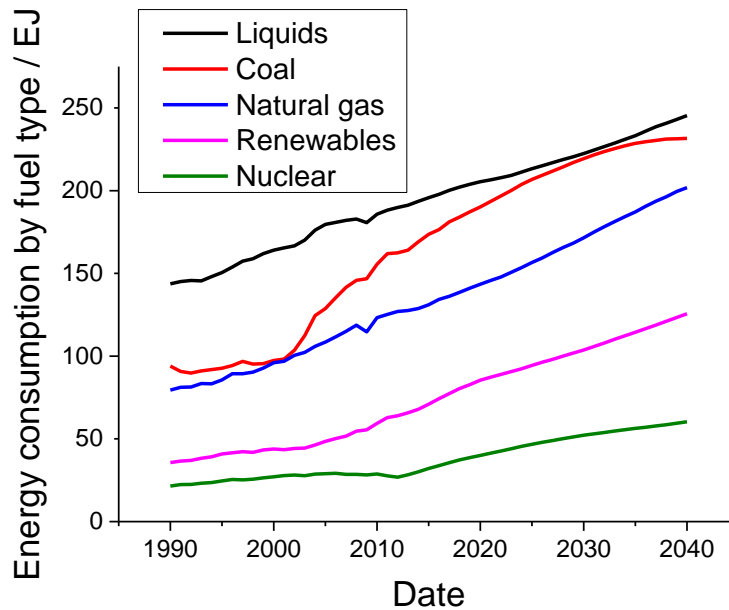


**Figure 2.4 – Total global energy consumption by fuel type, 1990 – 2014. Data from [10].**

It has been calculated that the known reserves of traditional coal, oil and gas will only last up to 2088 at current consumption rates [12]. However, new reserves are being discovered, such as shale oil, and controversial methods of extracting the reserves, that could otherwise not be extracted *via* conventional methods, are currently being used (such as hydraulic fracturing). Shale oil is extracted from oil shale rock fragments *via* pyrolysis, thermal dissolution or hydrogenation [13, 14]. Hydraulic fracturing is a mining technique in which a mixture of liquids and sand are injected at high pressures into a wellbore, causing small fractures in the deep rocks, along which gas or oil can migrate into the well [15]. Both of these methods are environmentally damaging, but are expected to be greatly utilised in the near future.

Due to the reliance that many countries have on fossil fuels and the uneven distribution of fossil fuel sources, the depletion of these sources could also cause major issues with energy security, due to the vast global network of importing energy from other countries [16].

Not only are fossil fuels running out, but the use of fossil fuels for energy is a major contributor to climate change through the production of harmful emissions, including carbon dioxide (CO<sub>2</sub>), carbon monoxide (CO), methane (CH<sub>4</sub>), sulphur dioxide (SO<sub>2</sub>), nitric oxide (NO), nitrous oxide (N<sub>2</sub>O), nitrogen dioxide (NO<sub>2</sub>), ozone

(O<sub>3</sub>) and chlorofluorocarbons (CFCs) [17]. These contribute to various harmful effects on the environment. SO<sub>2</sub> and NO<sub>x</sub> are the cause of acid rain which can have detrimental effect on infrastructure, limestone and other carbonate rocks, plants and aquatic animals [18]. Ozone depletion is caused mostly by CFCs and NO<sub>x</sub> reacting with the ozone causing an increase in the UV radiation reaching the surface of the Earth [17]. Air pollution is caused by particulates in the Earth's atmosphere causing a significant risk to human health, including conditions such as heart disease and respiratory infections [19].

One of the most significant aspects of climate change is global warming. This is caused by changes in radiative forcing (RF), the balance between incoming radiation from the sun and outgoing infrared radiation, which is affected by the different greenhouse gases released into the atmosphere. The gas with the highest impact on positive RF (causing global warming, *c.f.* negative RF which causes global cooling) is carbon dioxide, due to its long atmospheric lifetime and its significantly greater quantities than other high RF gases such as methane. The total net anthropogenic RF value is 1.7 W m<sup>-2</sup>, which is significantly larger than the natural solar RF value of 0.05 W m<sup>-2</sup>, indicating that global warming is caused by anthropogenic sources [20]. In 2012, 82 % of the total greenhouse gas emissions in the United States was carbon dioxide, and its presence in large quantities is thought to have irreversible effects on the global climate [21, 22]. The seriousness of recent global warming can be seen in Figure 2.5, with an average land temperature rise of around 1.5 °C since 1750.

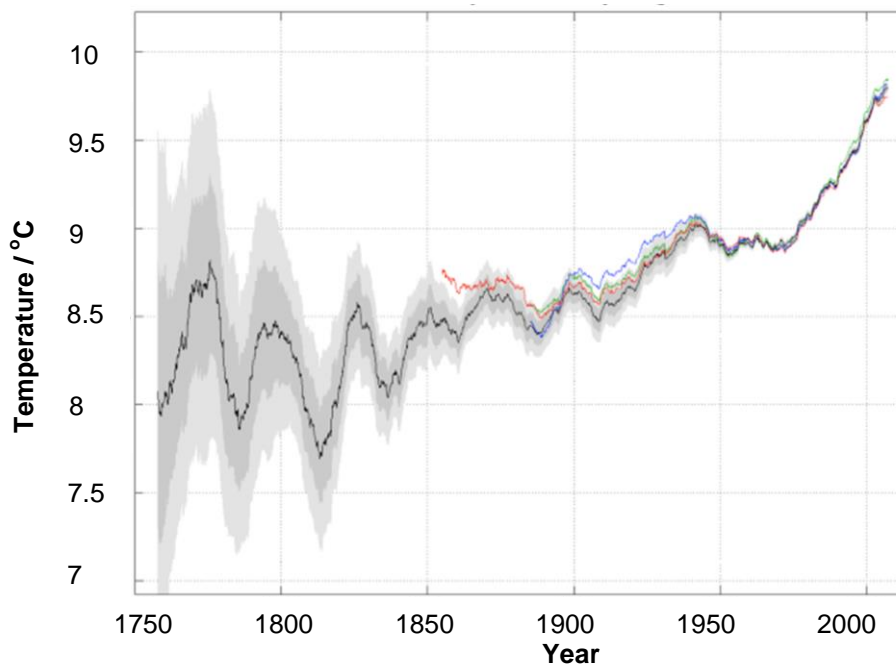


**Figure 2.5 – Land temperature 10-year running average. The shaded regions show the one- and two- standard deviation uncertainties calculated including both statistical and spatial sampling errors. Prior land results from other groups are also plotted in different colours. Figure adapted from [23].**

Concern has been raised about these figures, and governments have started to put several measures in place in order to try to reduce the greenhouse gas emissions. For example, the 2008 Climate Change Act in the United Kingdom aimed to reduce the UK's greenhouse gas emissions by at least 80% from the 1990 baseline by 2050, and was the world's first legally binding climate change target [24].

Global warming has numerous consequences, including sea level rise, oceanic acidification, potential gas hydrate eruptions, more extreme weather conditions, and a decrease in biodiversity [25]. All of these issues will continue to worsen unless clean sources of energy substitute fossil fuels in supplying the majority of the global energy demand. Therefore, not only is there a rapidly rising global demand for energy, but also a need for new, cleaner sources of energy to fulfil this demand.

Potential cleaner sources of energy available include nuclear energy and renewable sources of energy. Nuclear energy provided approximately 12.3 % of the world's electricity production in 2012 [26], and has the potential to be a viable

source of baseload energy in the near future as it is a very mature technology and is not as variable or intermittent as most renewable sources of energy. However, nuclear energy commonly uses uranium which is a finite resource, and there are also issues with the safety and waste disposal from nuclear plants [27]. Public perception is also a problem with nuclear energy, which was only worsened by the Fukushima disaster in 2011 [28]. Despite this, 72 new nuclear plants are currently under construction, particularly in China, and many more are expected to be commissioned in the near future [26].

Renewable sources of energy provided approximately 19 % of global final energy consumption in 2011, although 49 % of this was from biomass, mostly accounted for by the use of firewood in non-OECD countries [29]. However, the total potential capacity of renewable sources of energy is enormous, being able to supply over 3000 times the current global energy consumption, excluding space and technical limits [9].

Renewable sources of energy have many positive attributes, including minimal greenhouse gas emissions, they cannot be depleted, they are generally distributed worldwide and so can enhance energy security, and they are predictable and clean. They also have the capability of increasing energy use in non-OECD countries, and their costs are likely to decrease dramatically as technologies mature [30]. However, there are also some problems with renewable sources of energy, including that most of them are currently very capital-intensive due to the novelty of the technologies, they are intermittent and variable and so need to be used in conjunction with other forms of energy. They also generally rely on very diffuse sources of energy, and the energy they produce needs to be immediately either used or converted into a form which can be stored [30].

The different types of renewable sources of energy include solar energy, biomass, hydroelectric power, wind energy, tidal energy, marine current, wave energy and geothermal energy. The U.S. Energy Information Administration has predicted that, by 2035, the contribution of renewables to global electricity generation will have doubled [31]. It is very likely that there will not be one main source of energy in the future but a complex mixture, with renewable sources of energy contributing to a large sector of this.

## **2.2 Energy storage and hydrogen**

As mentioned previously, renewable sources of energy do not produce a stored form of energy, and so it needs to be stored separately. This is very important as energy is required on demand, not only when it is produced, and it also needs to be transported as many renewable sources of energy are in remote locations such as offshore wind farms. There are many ways in which energy can be stored, such as in batteries (which can leak, are expensive, suffer energy losses during charging and discharging, and have a limited lifetime), in flywheels and supercapacitors (which have a low energy storage potential), as pumped hydroelectric storage (which has large capital costs and is site specific), as compressed air storage (which requires large tanks, introducing geological restrictions), and by the production and storage of molecular hydrogen [32-34].

Hydrogen is the lightest element, consisting of a single proton and electron. At standard temperature and pressure (273 K, 0.1 MPa) molecular hydrogen ( $H_2$ ) is a colourless, tasteless, odourless, non-toxic, highly combustible, diatomic gas. It is the most abundant element in the universe (75 % by mass, 90 % by number of atoms), but on earth is mostly found in combination with other elements, such as with oxygen in the form of water. Hydrogen was named by Antoine Lavoisier in 1783, but it was first identified as a distinct element by Henry Cavendish in 1766 [35]. Hydrogen has been used in various applications in the past, the most widespread being in the manufacture of ammonia based fertilisers, and in petroleum processing [36, 37].

There are many benefits of using hydrogen as an energy store, including that it has the highest energy content of any chemical fuel on a mass basis (Figure 2.6), it is abundant and the methods used to strip it from materials are mature, it only produces water as a by-product when used as a fuel, and there are a wide variety of methods available to retrieve the energy when necessary. Not only does hydrogen have the potential to manage the intermittency of renewables, but it could also be used as an alternative transport fuel, since the transport sector is accountable for approximately 21 % of all global carbon dioxide emissions [38, 39]. However, there are several challenges that need to be overcome before

hydrogen can be considered for use as a viable, commercial energy store; namely, the production and the storage of the hydrogen.

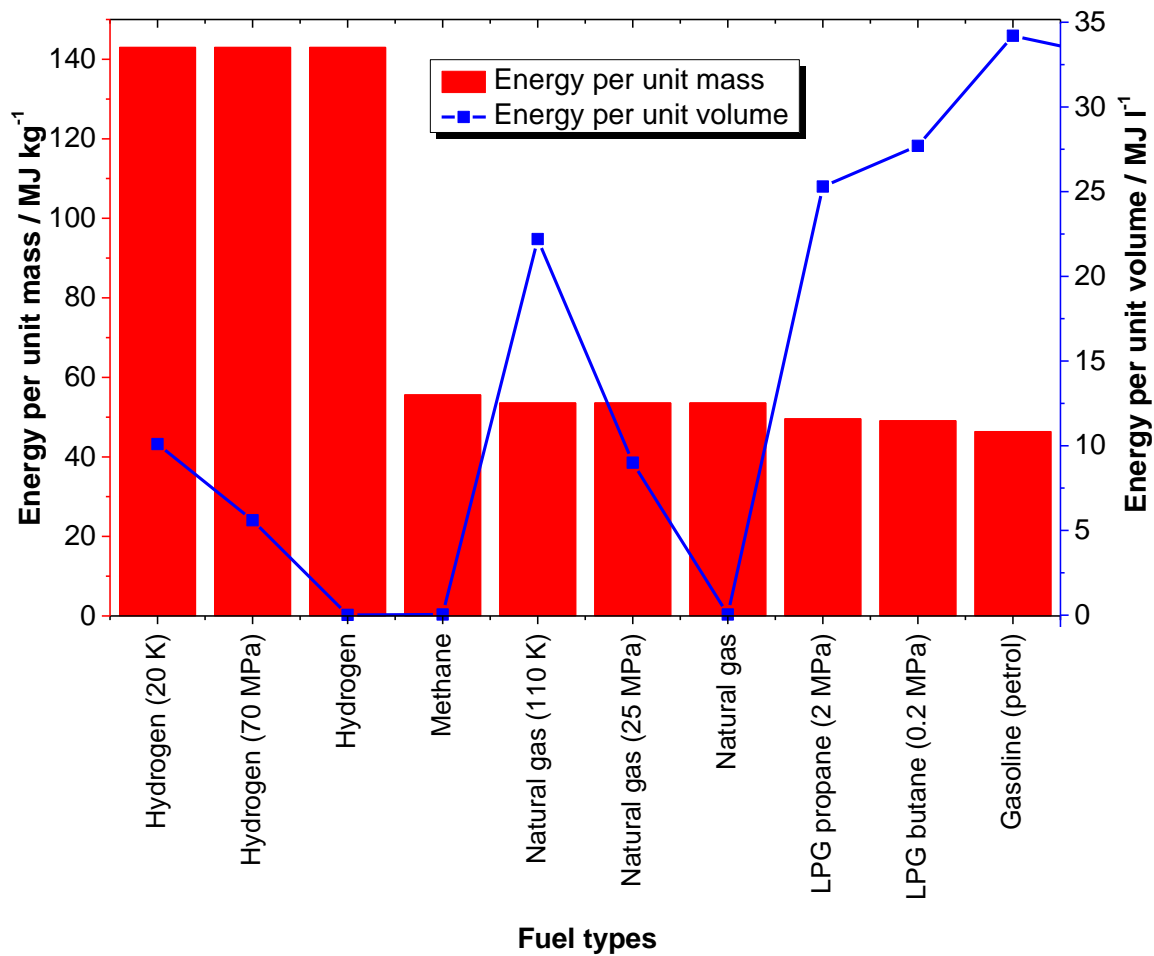


Figure 2.6 – Energy per unit mass and per unit volume for different fuels. LPG stands for liquid petroleum gas. Lines connecting the points are just to guide the eye. All conditions are ambient (298 K, 0.1 MPa) unless otherwise stated. Data received from [40].

Hydrogen rarely exists on earth as gaseous molecular hydrogen, so it needs to be produced. Currently, the most common and least expensive method for producing hydrogen is by steam methane reforming, which is used to produce approximately 50 % of hydrogen globally [41]. However, this is a particularly unsustainable process and produces over 7 kg of carbon dioxide per kg hydrogen produced [41]. Other methods of producing hydrogen include biomass gasification, pyrolysis, electrolysis, photoelectrolysis and thermochemical water splitting [41]. However, these are mostly immature technologies and so are currently quite expensive, though a variety of research is going into improving these technologies in order to make them cheaper and more commercially viable [42].

As previously mentioned, another issue is the storage of hydrogen. This is highly relevant because even though hydrogen has a very high energy per unit mass, it has a very low energy per unit volume ( $10.783 \text{ MJ m}^{-3}$  at ambient conditions, *c.f.* diesel which has  $36,500 \text{ MJ m}^{-3}$ ) [40]. Therefore, the density of hydrogen needs to be vastly increased if it is to be a useful source of stored energy. There are four methods of doing this: compression, liquefaction, chemisorption and physisorption. Compression and liquefaction are the current state of the art methods, but they both require unfavourable conditions; high pressures (up to 70 MPa) and low temperatures ( $\sim 20 \text{ K}$ ), respectively. Compression does not increase the energy density to a high enough value to satisfy the current fuel range of vehicles, and high costs are required for the compression process and the tanks. Another problem is the safety of the highly pressurised tanks. Storing the hydrogen *via* liquefaction has the problems of boil-off, as well as the low efficiency of the liquefaction process, limiting it to applications with a short hydrogen consumption time, and where cost is not an issue [43]. Despite these issues, both liquefaction and compression of hydrogen have been used in commercial transport applications such as the BMW Hydrogen 7 car (limited production, liquid hydrogen tank) [44], the Hyundai ix35 Hydrogen Fuel Cell Vehicle (series production, compressed hydrogen tank) [45], the Honda FCX Clarity (available on lease, compressed hydrogen tank) [46], the Mercedes-Benz B-Class F-Cell (available on lease, compressed hydrogen tank) [47], the London hydrogen buses (limited production, compressed hydrogen tank) [48], and forklift trucks (limited production, compressed hydrogen tank) [49]. One obvious barrier to hydrogen vehicles is the lack of hydrogen infrastructure, although there is a drive to push more fuelling stations and 'hydrogen highways', particularly in Japan, Europe and North America [50].

Chemisorption and physisorption are both solid state methods of storing hydrogen, although chemisorption also offers liquid carrier options, such as ammonia. Chemisorption consists of hydrogen dissociating into atomic hydrogen, and subsequently chemically absorbing into a material forming chemical bonds of the order of  $100 \text{ kJ mol}^{-1}$ , for example  $\text{MgH}_2$ . However, these relatively strong interactions mean that appreciable heat is required in order to extract the hydrogen from the material again, which is a slow process due to reaction kinetics

[51]. Physisorption comprises molecular hydrogen physically adsorbing onto the surface of a material, usually within pores. The process of adsorption can be described in terms of a one-dimensional Lennard-Jones potential energy curve [52]. The attractive forces between the hydrogen and the surface of the material are van der Waals interactions ( $\sim 5 - 10 \text{ kJ mol}^{-1}$ ), caused by resonant fluctuations of the charge distributions between the polarisable hydrogen molecule and several atoms on the surface of the material [53]. Due to the attractive and repulsive terms between the hydrogen molecule and the surface of the material, explained by the Lennard-Jones potential, the hydrogen molecule will be adsorbed at at least one molecular radius away from the material [53]. The weak interactions between the hydrogen and the surface provide ease of hydrogen extraction, but also necessitates low temperatures in order to adsorb significant quantities of hydrogen by slowing down the rate of desorption.

The U.S. Department of Energy (DOE) has set a system gravimetric density target of 5.5 weight percent (wt%) hydrogen by 2015 for light duty vehicles [54], and many different materials are being synthesised and analysed for hydrogen storage in order to try to reach this target. The only solid state hydrogen storage material that is currently close to becoming commercially available is ammonia borane in the form of pellets synthesised by Cella Energy, intended to be used in transport applications [55]. However, the hydrogen from the pellets is obtained by thermolysis which is not a reversible process, and so the pellets would need to be completely removed after use and fresh material reloaded.

Considering current materials that are being studied for hydrogen storage, 10 wt% excess hydrogen uptake in a material at 77 K and  $< 20 \text{ MPa}$  (excluding the system weight) is viewed as superior, 5 wt% is satisfactory, and anything less than 2 wt% is poor, although even the highest uptake materials are still a long way off the DOE systems target. The total hydrogen uptake differs from excess hydrogen uptake in that total uptake is a measure of the total amount of hydrogen in the system, whereas excess is a quantity that is measured experimentally and refers only to the additional amount of hydrogen in the system due to the interactions with the material, explained in more detail later on in the chapter.

Materials are classified according to their pore size by the International Union of Pure and Applied Chemistry (IUPAC), and they can be microporous (with pores narrower than 2 nm), mesoporous (with pore widths between 2 and 50 nm) and macroporous (with pore widths larger than 50 nm) [56]. The material properties required for physisorption of hydrogen are a high micropore volume, a large surface area and good accessibility to the pores. Pores larger than a micropore are not desirable for hydrogen uptake, as the hydrogen density is increased by interactions with the surface of the material. Therefore, pores larger than a micropore result in weaker interactions between the hydrogen and the material, and consequently lower hydrogen densities. There are many different types of porous materials that are researched for hydrogen storage, including metal-organic frameworks (MOFs), nanostructured carbons, zeolites and polymers of intrinsic microporosity (PIMs).

MOFs consist of metal centres strongly bonded to organic linkers (as seen in Figure 2.7), and have been explored since the early 1990s [57, 58]. They can be tailored for specific applications by, for example, changing the shape and size of the linker to alter the pore size, or by choosing different metal centres. MOFs can be synthesised relatively easily, and have been examined for use in catalysis [59, 60], gas separations [61, 62], and gas storage [63, 64]. Another interesting feature of certain MOFs is the structural change that is induced by either introducing guest molecules into the pores or altering the pressure or temperature. These MOFs are known as 'flexible' or 'breathing' MOFs, and this process has been observed as a potentially interesting phenomenon in the study of gas storage [65-67]. Some MOFs have shown very promising hydrogen uptakes, one of the highest being NU-100 ( $[\text{Cu}_3(\text{L})(\text{H}_2\text{O})_3]_n$ , where  $\text{LH}_6$  is 1,3,5-tris[(1,3-carboxylic acid-5-(4-(ethynyl)phenyl))ethynyl]-benzene) with an excess uptake of 9.95 wt% at 7 MPa and 77 K [68].

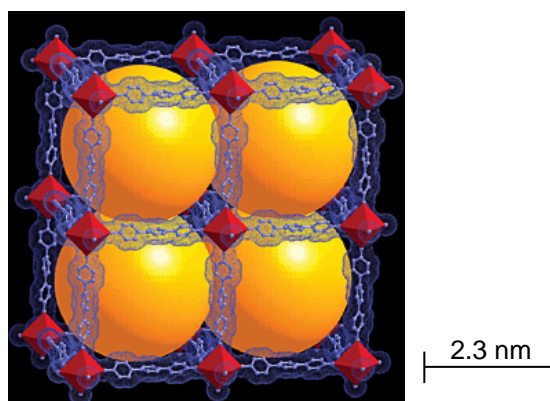


**Figure 2.7 – An example of a MOF, IRMOF-16, with the metal centres (red) linked by organic linkers (blue), and the yellow balls depicting the space available for adsorption [69].**

Many different types of nanostructured carbons can be used for hydrogen adsorption, including activated carbons, nanotubes and carbide-derived carbons (CDCs) [70]. They all have varying structures due to the difference in the packing of the carbon. Activated carbon (Figure 2.8) consists of graphene sheets tightly packed into an amorphous porous structure, and can be synthesised by oxidising a wide variety of precursors. No activated carbons have shown over 1 wt% hydrogen uptake at room temperature up to 20 MPa; however, the AX-21 material displays 5.2 wt% excess hydrogen uptake at 77 K and 2.9 MPa [71].

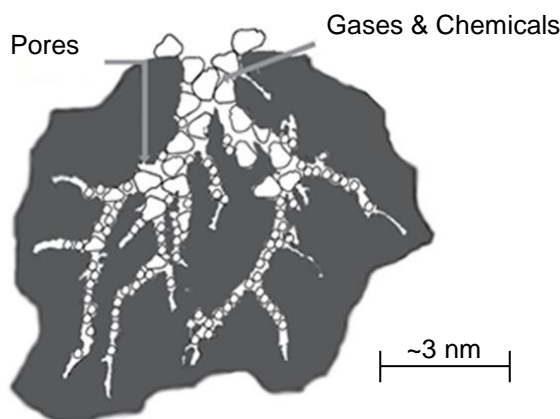


**Figure 2.8 – An illustration of an activated carbon particle. The scale is an estimated value to illustrate the size of activated carbon pores. Adapted from [72].**

Carbon nanotubes are graphene sheets wound into tube structures, and can be either single-walled, or multi-walled (Figure 2.9, A and B respectively). There have been many contradicting hydrogen uptake results in literature for these materials, some showing uptakes of up to 21 wt%, although these were never verified and were attributed to measurement errors [70, 73].

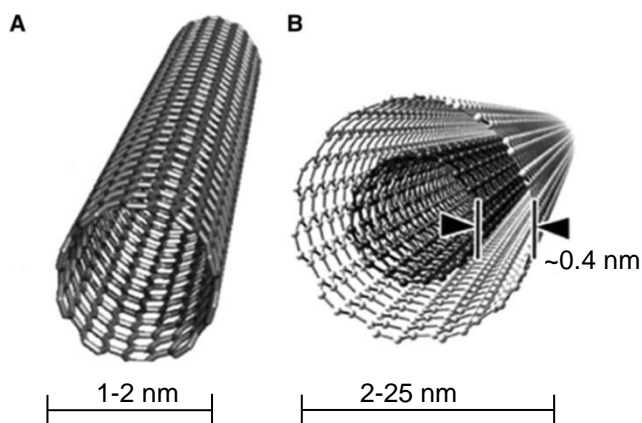


**Figure 2.9** – A conceptual diagram of a (A) single-walled carbon nanotube and a (B) multi-walled carbon nanotube. The arrows in (B) highlight the inter-layer spacing. The scales given are typical dimensions for SWNTs and MWNTs. Adapted from [74].

CDCs are formed from carbide precursors which are transformed into carbon *via* thermal decomposition or halogenation (Figure 2.10). They display a variety of pore sizes, making some of them very interesting potential candidates for hydrogen storage. A superactivated (activated with potassium hydroxide) CDC has been shown to have a large hydrogen uptake of 2.7 wt% at 77 K and 0.1 MPa and up to 6.2 wt% at 77 K and 2 MPa [75].

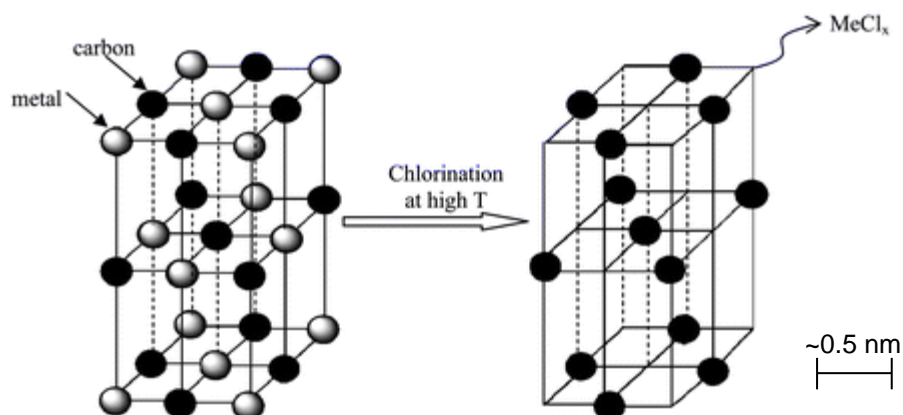


**Figure 2.10** – An illustration of a synthetic route of a CDC using high-temperature chlorination of a metal carbide. The scale given is a representative value for metal carbide lattice spacing. Figure taken from [76].

Pillared graphene consists of graphene sheets linked by carbon nanotubes (Figure 2.11). The carbon nanotubes support the graphene sheets, can optimise the distance between the sheets, and reduce the empty space between the sheets. Computer simulations show a higher uptake than in both pure graphene and carbon nanotubes at 77 K and pressures above 5 MPa [77]. To date, pillared

graphene is mostly mentioned in theoretical studies due to the difficulty in the synthesis; however, attempts have been made at transferring pillared graphene nanostructures onto graphene layers whilst maintaining their 3D architecture [78].

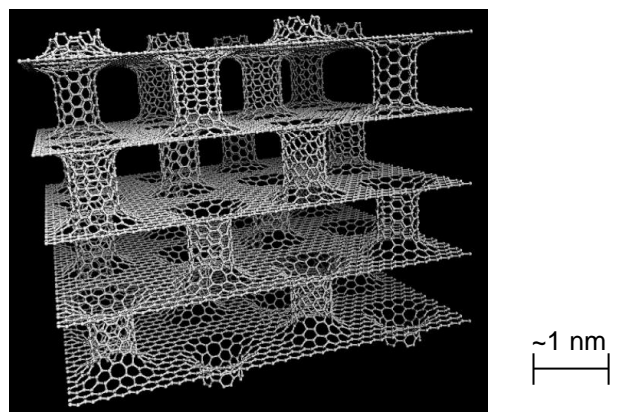


**Figure 2.11 – An illustration of pillared graphene. The scale given is estimated to provide an idea of the approximate size. Figure taken from [77].**

The benefits of carbon-based materials are that they are generally low cost and are lightweight, they have a wide variety of structural forms and good thermal stability, and the structures are easily modified [79]. One very interesting literature example of a high hydrogen uptake carbon is a MOF-derived carbon, which involves pyrolyzing a zinc based MOF, IRMOF-1, at 1,173 K for 3 hours, resulting in a carbon with a high excess hydrogen uptake of 3.4 wt% at 77 K and 0.1 MPa [80].

Zeolites are hydrated aluminosilicates, and were first termed ‘zeolites’ back in 1756 by Axel Cronstedt, from the Greek words *zéō* and *lithíos*, meaning boiling stone [81]. They have been used in a variety of industrial applications, including in detergents, in catalytic processes, and as adsorbents [81, 82]. There are approximately 40 natural zeolites that have been discovered, which were formed over thousands of years in specific geological environments. However, since the 1940s, zeolites have also been synthesised [83], such as ZSM-5 (Figure 2.12). One of the highest hydrogen uptakes in a zeolite to date is the calcium-exchanged zeolite X, which has a reported excess uptake of 2.19 wt% at 77 K and 1.5 MPa [84].

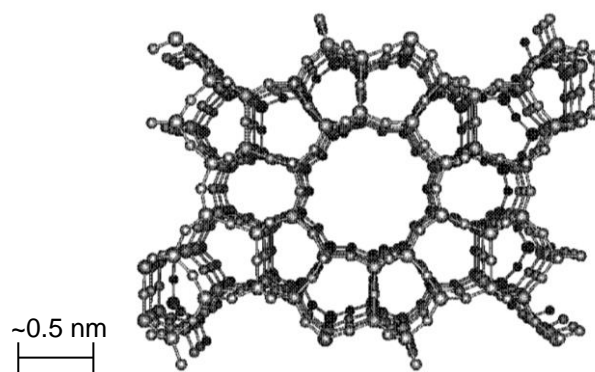


**Figure 2.12 – The framework structure of the zeolite ZSM-5. Figure taken from [85].**

PIMs, for example PIM-1 (Figure 2.13), were only discovered within the last decade, from an initial idea of creating network polymers with microporous and either amorphous or short-range crystalline structures [86]. PIMs possess properties of both polymers and conventional microporous materials, providing them with the advantage of having high surface areas, as well as superior stability and easy processability. The highest hydrogen uptake in a PIM so far is by PPN-4 (Porous Polymer Network 4), with an excess uptake of 8.34 wt% at 77 K and 5.5 MPa [87].

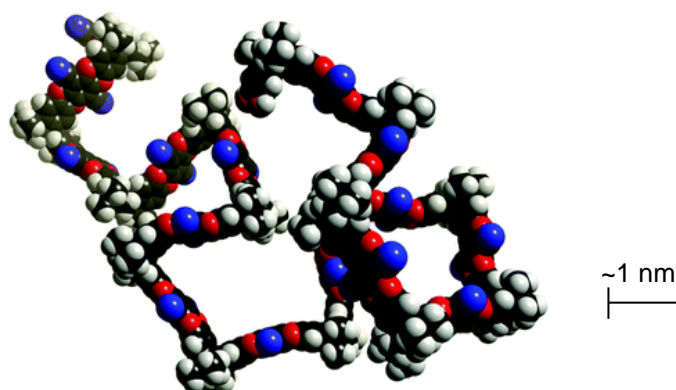


**Figure 2.13 – A molecular model of an example PIM structure, PIM-1. The white spheres represent carbon, blue represents nitrogen, and red represents oxygen. Figure taken from [86].**

Since one of the intended uses of all of these materials for hydrogen storage is to aid in the reduction of climate change, the life cycle of the materials is important in order to determine if they are suitable for this; however, the sustainability of these materials has rarely been addressed in the literature. This is particularly true for MOFs and PIMs, which are still mostly synthesised in relatively small quantities.

However, there have been a few articles published on sustainable synthetic pathways for carbons and zeolites [88-90].

## **2.3 Applications of hydrogen in energy systems**

### **2.3.1 Introduction**

Once hydrogen has been successfully stored, its energy can be converted to electrical energy (*via* a fuel cell or a gas turbine), mechanical energy (*via* an internal combustion engine), or thermal energy (*via* a boiler or a catalytic burner). Two current areas of interest are the hydrogen internal combustion engine (HICE), and the hydrogen fuel cell, both of which have potential applications for transport.

HICEs are very similar to standard petrol-powered internal combustion engines (where 'petrol' here refers to the American term gasoline), but they use hydrogen and air as fuel. The first ever internal combustion engine, constructed in 1806 by De Rivaz, was actually powered by hydrogen, and subsequently there has been adequate development of the HICE, resulting in a well-established technology [91-93]. HICEs have been used in various prototype vehicles, including the BMW Hydrogen 7 car [44], as well as commercially in forklift trucks [49].

Hydrogen fuel cell technology is not as mature as HICE technology, particularly as cold-weather operation is still problematic [94]. There are many classes of hydrogen fuel cells, including proton exchange membrane fuel cells (PEMFC), solid oxide fuel cells (SOFC), alkaline fuel cells (AFC), phosphoric acid fuel cells (PAFC) and molten carbonate fuel cells (MCFC) [95]. One of the most promising hydrogen fuel cell technologies is the PEMFC, which works by ionising the hydrogen into protons and electrons at the anode, followed by the migration of the protons through a membrane and onto the cathode, where they subsequently react with oxygen to produce water [96, 97]. However, the major problem with these fuel cells is that even trace amounts of impurities within the system cause a large decrease in the performance [98]. Therefore, significant research needs to be conducted before they can become commercially viable. However, there have been some prototype cars incorporating hydrogen powered PEMFCs, including the Hyundai ix35 fuel-cell prototype [99], and the Mercedes-Benz B-class F-cell [100].

### **2.3.2 Hydrogen in aviation**

Many of the emissions from aviation are released into the upper atmosphere. Although this does not alter the effect of long-lived emissions such as carbon

dioxide (although the production of these is still significant), it does increase the RF values of short-lived gases, causing even greater impacts on global warming [101-103].

The use of hydrogen in aerospace applications was first proposed in 1766 when Joseph Black suggested that a hydrogen filled balloon would be able to rise into the air, and take objects with it. This was put into practice in 1783 (only a few months after the Montgolfier balloon) when a hydrogen filled balloon carried two passengers nearly 600 m high for over two hours. Then, in 1900, the very first airship, the Zeppelin LZ1, was flown purely on 11,000 m<sup>3</sup> of hydrogen gas [104]. Since these initial applications, hydrogen has been used for various functions within the aerospace industry.

Even though hydrogen has played various roles within aerospace, its use in aircraft has been limited since the era of the Zeppelin-type airships, which ended in 1940. However, more recently there have been some hydrogen-powered aircraft demonstrations, as well as several prototypes. Examples of these are shown in Table 2.1.

**Table 2.1 – Prototypes and demonstrations of hydrogen powered aircraft. Ref stands for reference.**

<b>Institute/model</b>	<b>Conversion of energy</b>	<b>Storage of hydrogen</b>	<b>Year</b>	<b>Stage</b>	<b>Ref</b>
Tupolev Tu-155	HICE	Cryogenic	1988	Test flights	[105]
Cryoplane project (Airbus)	HICE	Cryogenic	2003	Concept study	[106]
NASA - Quiet Green Transport Concept B	PEMFC	Cryogenic	2004	Concept study	[107]
Georgia Institute of Technology fuel cell-powered unmanned aerial vehicle	PEMFC	Compression	2006	Test flights	[108]
Lange Aviation – Antares DLR-H2 - manned	Fuel cell (with Li-ion batteries if needed)	Compression	2009	Test flights	[109]
EADS ZEHST High-Speed Transport Concept Study	Ramjet	Cryogenic	2009	Concept study	[110]
Boeing phantom eye - unmanned	HICE	Cryogenic	2010	Test flights	[111]
ENFICA-FC - Rapid 200-FC	PEMFC, Li-Po battery	Compression	2010	Test flights	[112]
AeroVironment Global Observer - unmanned	HICE	Cryogenic	2011	Test flights	[113]
Lange Aviation – Antares DLR-H3 - unmanned	Fuel cells	Compression	2011	Test flights	[114]

The aircraft mentioned in Table 2.1 have remained as prototypes and have not been successfully commercialised for a number of reasons, including:

- The lack of a sustainable production method of hydrogen, as mentioned previously in Section 2.2.
- The fuel cells currently used in the prototypes are not powerful enough to provide the propulsion that many aircraft require to get off the ground. Even if this initial challenge is eventually overcome, there is the likely further drawback of greater noise pollution, due to the subsequently slower take-offs [107].
- A large change in the infrastructure of current planes would be required; it would not just be the case of taking out the old engines and putting in a fuel cell and hydrogen tank. The new infrastructure would have to account for the gain in weight of the aircraft due to the fuel cells and the large hydrogen storage tanks [115, 116]. This extra weight would also decrease the energy efficiency of the flights, particularly for short distances. The infrastructure would have to account for the additional volumes required to store the hydrogen.
- Water vapour emissions would triple, which would have an unknown effect on radiative forcing at high altitudes [117, 118].

Adsorption has not yet been utilised for hydrogen storage in aviation due to the immaturity of the technology as well as the lack of scale-up technology. There has been limited research conducted on scale-up technology, and those available are only theoretical studies. For example, one study by Ahluwalia *et al.* observed hydrogen adsorbed in activated carbons in a tank at cryogenic temperatures and concluded that the system was not suitable for automotive applications, and therefore even less so for aviation, where mass is a much more significant factor [119]. Another study compared the amount of hydrogen stored in a tank *via* compression to the amount stored *via* adsorption in both a MOF and in a carbon, although the rest of the system was not taken into consideration [120].

## 2.4 The modelling of hydrogen adsorption

Modelling adsorption has been extensively studied in the literature over the past century, although to a lesser extent for hydrogen adsorption. There is currently ongoing research into the modelling of hydrogen adsorption in a number of groups worldwide, the most prominent being the work conducted by a group at the Université du Québec at Trois-Rivières led by Chahine, [120-128], and that led by Dailly and co-workers at the General Motors Chemical and Environmental Sciences Laboratory [129-134].

The modelling is generally conducted by fitting developed equations to experimental hydrogen adsorption data on porous materials, and is vital for numerous reasons. One example of this is that the modelling can be used to determine the total amount of hydrogen within a material, as this cannot easily be measured experimentally. It can also be used to better understand the fundamentals of the adsorption process *via* manipulation of the parameters within the models.

Adsorption has been modelled since the early 1900s, and is still a very popular area of research today. The first recognised equation was derived by Irving Langmuir in 1918, (Equation 2.1), and is aptly named the Langmuir equation [135]. This type of equation is one of many in literature known as an isotherm equation (where isotherms are the most common measurement of adsorption, showing the amount adsorbed at constant temperature with increasing pressure). It calculates the coverage of adsorbed molecules on a surface,  $\Theta_A$  (-), with respect to pressure,  $P$  (MPa), at a fixed temperature,  $T$  (K), also known as the fractional filling.

$$\Theta_A = \frac{bP}{1+bP} \quad 2.1$$

where  $b$  ( $\text{MPa}^{-1}$ ) is the affinity parameter, a constant that relates to the strength of adsorption onto the surface, and is usually assumed to follow an Arrhenius relationship [136],

$$b = A \exp\left(\frac{Q}{RT}\right) \quad 2.2$$

where  $A$  ( $\text{MPa}^{-1}$ ) is the pre-exponential factor and relates to the entropy of adsorption,  $R$  ( $\text{MPa cm}^3 \text{K}^{-1} \text{mol}^{-1}$ ) is the molar gas constant and  $Q$  ( $\text{kJ mol}^{-1}$ ) is a semi-empirical isotherm parameter relating to the heat flow and is correlated to  $\Delta H$  ( $\text{kJ mol}^{-1}$ ), the enthalpy of interaction between the hydrogen and the surface.

The Langmuir equation is kinetic in nature, and is derived by considering the adsorption process as



Where  $A$  is the adsorbate and  $M$  is the surface site.

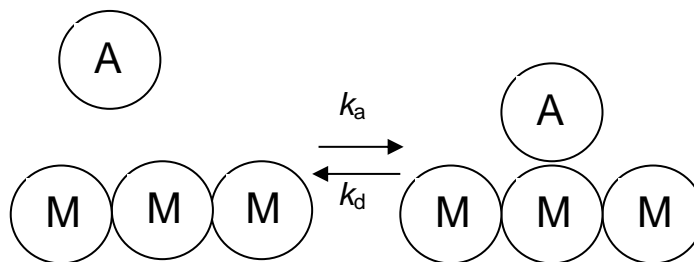


**Figure 2.14 – An illustration of adsorption and desorption of A onto a surface of molecules, M.  $k_a$  and  $k_d$  represent the rate constants of adsorption and desorption respectively.**

$$\text{Rate of adsorption} = k_a [A][M] \quad 2.4$$

$$\text{Rate of desorption} = k_d [AM] \quad 2.5$$

where  $[A]$ ,  $[M]$  and  $[AM]$  are the concentrations of A, M, and AM respectively. At equilibrium, the rate of adsorption is equal to the rate of desorption, so

$$k_a [A][M] = k_d [AM] \quad 2.6$$

However,  $[A]$  is proportional to the pressure,  $P$ ,  $[AM]$  is proportional to the coverage,  $\Theta$ , and  $[M]$  is proportional to the surface not covered ( $1-\Theta$ ).

Therefore, substituting these into Equation 2.6, the following is derived;

$$k_a P(1-\Theta) = k_d \Theta \quad 2.7$$

$$\Theta = \frac{k_a P}{k_d + k_a P} \quad 2.8$$

It is also known that

$$b = \frac{k_a}{k_d} \quad 2.9$$

Therefore, substituting Equation 2.9 into Equation 2.8 results in

$$\Theta = \frac{bP}{1 + bP} \quad 2.10$$

The Langmuir equation is a very simple equation, and has been the basis of many other equations that have been subsequently derived [137-139].

There are two limiting behaviours of the Langmuir isotherm. Firstly, as the pressure tends to 0, the right hand side of Equation 2.10 tends to just  $bP$ , due to the  $bP$  on the denominator being negligible compared to 1. Mathematically, taking the derivative of Equation 2.10

$$\left(\frac{\partial \Theta}{\partial P}\right)_T = \frac{b}{(1 + bP)^2} \quad 2.11$$

$$\lim_{P \rightarrow 0} \left(\frac{\partial \Theta}{\partial P}\right)_T = b \quad 2.12$$

$$\Theta = bP \quad 2.13$$

This is an example of Henry's law, which was first expressed by W. Henry in 1803 and states that *"at a constant temperature, the mass of a given gas dissolved in a given volume of a solvent is directly proportional to its partial pressure in the gas phase in equilibrium with the solution"* as cited in Glasstone and Lewis [140]. Henry's constant here is  $b$ , as shown in Equation 2.13, which is the linear isotherm obtained for a diluted system. Thermodynamically, Henry's law should always be obeyed, but in practice this is not always the case. For example, as seen above the Langmuir equation follows Henry's law, however, some of the other equations which are used for the same purpose, e.g. the Sips equation [141], do not follow

Henry's law, meaning that they are not necessarily valid at very low pressures [137].

Secondly, as  $P$  tends to infinity, the right hand side of Equation 2.10 tends to 1, as the 1 in the denominator becomes negligible compared to the  $bP$ . This is called saturation, and unlike Henry's law it is binding and should always be obeyed.

$$\lim_{P \rightarrow \infty} \Theta = 1 \quad 2.14$$

Therefore, on a graph of coverage vs. pressure, the initial slope of the graph should represent  $bP$ , and the graph should tend to 1, as seen in Figure 2.15. Also, where the extrapolated initial slope intersects the coverage of 1, i.e.  $bP = 1$ , the pressure at that point is equal to  $1/b$ , which is known as the Henry pressure.

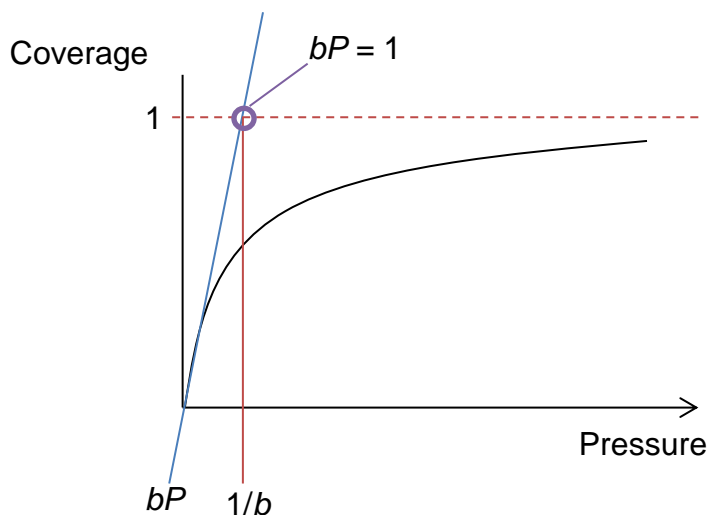


**Figure 2.15 – An illustration of Henry's law and the Henry pressure.  $b$  is the affinity parameter and  $P$  is the pressure.**

The Langmuir equation follows an IUPAC Type 1 isotherm shape (Figure 2.16, part I), which relates to monolayer coverage on a surface; for example, in a microporous solid with a small external surface for supercritical systems.

Consequently, this is very suitable for supercritical hydrogen adsorption which also produces isotherms of a Type 1 shape, as the weak interactions between the hydrogen and the material is thought to result in the majority of the hydrogen molecules being adsorbed in a monolayer. (Note: The adsorbed hydrogen is

referred to as the adsorbate, the bulk hydrogen is known as the adsorptive and the solid material that the hydrogen is adsorbed onto is referred to as the adsorbent.)

The Type 2 isotherm represents multilayer coverage as exists, for example, in a macroporous solid, and Type 3 shows a system with strong adsorbate-adsorbate interactions. Type 4 and 5 are Type 2 and 3 respectively but with hysteresis loops, associated with capillary condensation, and Type 6 represents adsorption on a non-porous solid, as represented in Figure 2.16 [56].

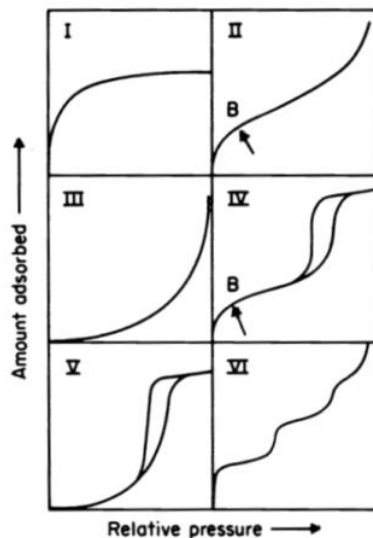


**Figure 2.16 – Types of physisorption isotherms [56].**

There are four assumptions of the Langmuir equation [135]:

- 1) There is only monolayer adsorption onto the surface.
- 2) The adsorption is localised, *i.e.* the molecules do not move around.
- 3) All the surface sites are energetically equivalent.
- 4) The heat of adsorption per molecule is constant.

Therefore, the Langmuir equation is only appropriate for limited systems at low pressures, and even then it is only approximate. The Type 1 isotherm equations that have subsequently been derived account for different surface energy distributions, and some account for other characteristics of the adsorption process, such as lateral interactions between the hydrogen molecules [137-139]. They can be fundamental or empirical, and some well-known examples of these equations include the Tóth equation [142], the Sips equation [141], and the Dubinin-Astakhov equation [121].

These isotherm equations allow calculation of the absolute amount of hydrogen in the system, which, as mentioned previously, differs from the excess hydrogen uptake which is the amount measured experimentally, also known as the Gibbs excess or Gibbsian surface excess due to its introduction by J. Williard Gibbs in 1928 [143, 144]. When experimentally measuring the adsorbed amount of hydrogen, a probe gas, requiring zero interactions with the adsorbent (usually helium), has to be dosed onto the sample initially in order to calculate the available space. Following removal of the probe gas, a known volume of hydrogen is dosed onto the sample, and the additional amount of hydrogen in the system above that of the probe gas volume is calculated. Therefore, the excess is the additional amount of hydrogen in the system due to the interactions with the adsorbent, as highlighted in Figure 2.17.

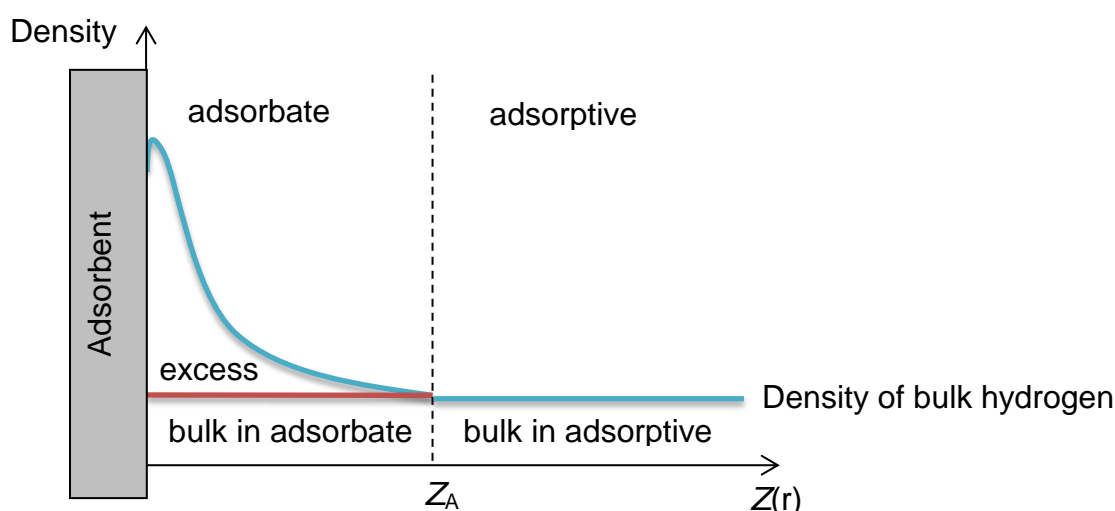


**Figure 2.17 – An illustration of the excess and absolute quantities of hydrogen. The excess is labelled (between the blue and the red lines) and the absolute is the total amount of hydrogen within the adsorbate (the total under the blue and red lines between the adsorbent and the vertical dotted line). The x-axis shows the distance from the adsorbent ( $Z(r)$ ) and the y-axis shows the density of the hydrogen.  $Z_A$  denotes the furthest distance from the adsorbent where there is adsorbate present.**

The difference between excess and absolute uptake is usually ignored at low pressures, but becomes much more significant at higher pressures.

There is one other variable which has recently been highlighted, and that is the total quantity of hydrogen. In Figure 2.17, this is the excess *plus* the bulk amount in the adsorbate *plus* the bulk amount in the adsorptive, *i.e.* the total amount of hydrogen in the system [145].

A methodology was derived in 1997 which uses Type 1 isotherm equations in order to calculate the excess amount of hydrogen in a system, which can be fit to the Gibbs' excess isotherms obtained experimentally using a gas analyser [146]. This method has since been expanded specifically for hydrogen adsorption through the works of Poirier, Dailly and Chahine [120-122, 124-127, 129-134]. These authors generally relate the absolute to the excess quantity of hydrogen, set the absolute quantity as the Dubinin-Astakhov equation, and fit to excess hydrogen isotherms in order to calculate the unknown parameters.

Another expansion has been made on the use of modelling for hydrogen adsorption, but without using the Dubinin-Astakhov approach, resulting in Equation 2.20, derived below [147].

It is a very simple system, assuming a single density within the pores, as seen in Figure 2.18.

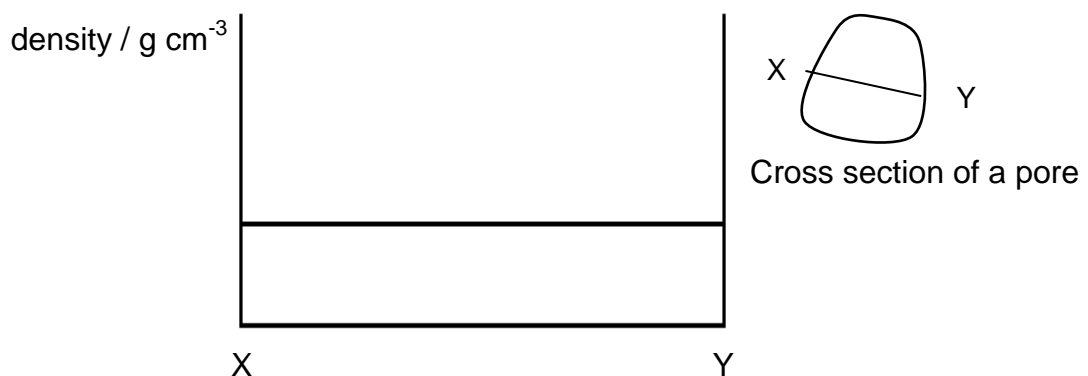


**Figure 2.18 – The hydrogen density profile within a pore, assumed in the initial model.**

As mentioned, the excess relates to any hydrogen in the system that is present over the amount that would have been present without any interactions with the adsorbent, *i.e.* when assuming a single hydrogen density within the pore, the excess hydrogen adsorption,  $m_E$  (wt%), is the absolute quantity of hydrogen,  $m_A$  (wt%), minus the bulk amount,  $m_B$  (wt%), which leads nicely into the derivation of the model. Here, and elsewhere in the thesis,  $m$  refers to the sample-specific quantity and is given in wt%, which is the grams of hydrogen divided by the grams of the hydrogen and the adsorbent, all multiplied by 100.

$$m_E = m_A - m_B \quad 2.15$$

where

$$m_A = m_A^{\max} \Theta_A \quad 2.16$$

and

$$m_B = 100 \rho_B v_P \quad 2.17$$

As seen, the absolute adsorption is equal to the maximum adsorption,  $m_A^{\max}$  (wt%), multiplied by an isotherm equation (fractional filling term),  $\Theta_A$  (-). The bulk adsorption includes a multiplier of 100 in order to balance the units,  $\rho_B$  ( $\text{g cm}^{-3}$ ) is the bulk density found using the gas laws (Equation 2.18), and  $v_P$  ( $\text{cm}^3 \text{g}^{-1}$ ) is the specific open pore volume (for a particular gas).

$$\rho_B = \frac{1}{Z} \frac{PM}{RT} \quad 2.18$$

Where  $P$  (MPa) is the pressure,  $M$  ( $\text{g mol}^{-1}$ ) is the molar mass (given to convert from molar to mass quantities),  $R$  ( $\text{MPa cm}^3 \text{K}^{-1} \text{mol}^{-1}$ ) is the molar gas constant,  $T$  (K) is the absolute temperature, and  $Z$  (-) is the compressibility factor to account for the fact that hydrogen is not an ideal gas.

Therefore, substituting Equation 2.18 into Equation 2.17 results in

$$m_B = 100 \frac{1}{Z} \frac{PM}{RT} v_P \quad 2.19$$

and substituting Equations 2.19 and 2.16 into Equation 2.15, Equation 2.20 is derived

$$m_E = m_A^{\max} \Theta_A - 100 \frac{1}{Z} \frac{PM}{RT} v_P \quad 2.20$$

This type of equation has been used to fit to adsorption isotherms of many different gases, but for hydrogen adsorption it has mostly been used to calculate the absolute amount of hydrogen using the parameters obtained from the fitting [121, 129, 147, 148, 149].

## **2.5 Aims and objectives**

The aim of this project was to further develop the modelling of hydrogen adsorption. This was done by improving the current model used for hydrogen adsorption, and verifying the developed model (or the DV model) *via* inelastic neutron scattering experiments and computer simulations. A comparison was also made between the use of different Type 1 isotherm equations within the model, in order to improve the comparison of the total amount of hydrogen stored within different materials. The pore volume and adsorbate density were analysed in detail with respect to their dependencies on pressure and temperature. This was all completed with the aim that a general model would be derived, which can be used for any adsorbent in a variety of different applications. One application that was studied was the use of the DV model to compare the amount of hydrogen stored *via* adsorption to the amount of hydrogen stored *via* compression, and also to the amount of energy stored *via* other systems such as batteries and standard jet fuel. The DV model was also used for a preliminary investigation into the use of hydrogen adsorption in aviation.

The original project objectives were:

- 1) To improve the current model used for hydrogen adsorption by introducing a more complex and realistic hydrogen density profile within the pore.
- 2) To expand on the parameters within the DV model in order to improve its quality of fit and to try to determine more information about the fundamentals of hydrogen adsorption. This will be done by:
  - a. Calculating the pore volume dependence on pressure and temperature.
  - b. Calculating the adsorbate density dependence on pressure and temperature.
  - c. Comparing the use of different Type 1 isotherm equations within the model on different materials, to see if they can be justly compared, and to see if any of the equations fit to the isotherms of certain materials better than others.
- 3) To verify the absolute amount of hydrogen within the adsorbate of a material, as calculated using the DV model, by inelastic neutron scattering.

- 4) To verify the total amount of hydrogen in the system, as calculated using the DV model, by computer simulations.
- 5) To use the DV model in order to make a direct comparison between the amounts of hydrogen stored in a tank *via* physisorption and direct compression at the same conditions.
- 6) To expand on the comparison between physisorption and compression by determining the amounts of hydrogen stored in a tank per unit volume and per unit mass.
- 7) To expand even further on the comparison by calculating the energy stored in a tank containing hydrogen, either *via* compression or adsorption, and introducing the comparison to other energy systems, such as a standard jet fuel.
- 8) To conduct a preliminary investigation into what needs to be considered before hydrogen adsorption can be used in aviation.

## **2.6 Conclusion**

This chapter has highlighted all of the relevant background to the research conducted in this thesis, starting very generally with the global energy situation, and then focussing on the storage of energy *via* hydrogen, and the modelling of this process. A list of aims and objectives has been provided, giving the specific areas of research that were desired to be conducted throughout the study.

## **Chapter Three**

### **Methodology**

### 3 Methodology

This chapter of the thesis highlights the synthesis and characterisation of the different materials that have been used throughout the work. The equipment that has been used to characterise these materials is also detailed, followed by a description of the analytical tools that have been used and an explanation of the methodology utilised for the molecular simulation study.

#### 3.1 Materials

Six materials have been used throughout this study, each of which is explained in detail in this section, including the source of the material, the synthetic route, the pore sizes, the surface area, the micropore volume, the skeletal density and the range of different temperature isotherms.

The materials were chosen due to the differences in the properties of each one to make sure that the equations shown in Chapter 4 were applicable to a range of materials in order to eliminate bias. They show a broad range of pore sizes, mostly microporous but with some materials also containing mesopores. Certain materials are particularly ordered with a unimodal pore size distribution, whereas some show a few discrete pore sizes and the rest contain a broad range of pore sizes. The Brunauer, Emmett and Teller (BET) surface areas range between 960 and 2,887 m<sup>2</sup> g<sup>-1</sup>, and the micropore volumes between 0.3 and 1.9 cm<sup>3</sup> g<sup>-1</sup>. Two of the materials are carbon based, but the other four are composed of different metals along with carbon and either oxygen or nitrogen. All the materials show differing flexibilities; some are very rigid materials, some slightly flexible, and one very flexible material. They also have a range of different temperature isotherms, with the isotherms from the two materials taken from literature ranging between 50 and 125 K, and the isotherms from the other four materials being produced experimentally in Bath and ranging between 77 and 150 K. They all have different maximum excess hydrogen capacities ranging from 2.5 wt% to 7 wt% at the highest pressure and lowest temperature isotherm measured for each material.

When choosing materials from the literature, the preferred materials were those with isotherms that went up to high pressures and scaled a wide range of temperatures (preferably low temperatures as these have a smaller error, resulting in more accurate fits).

The MIL-53 and MIL-101 materials were synthesised by the author, who also conducted all of the characterisation of the MIL-53 material. The TE7 carbon beads and AX-21 activated carbon were sourced externally, and these plus the MIL-101 material were characterised by colleagues of the author, and where applicable, the values were taken from the literature. The author sourced the isotherms and necessary data of the ZIF-8 externally, and colleagues of the author sourced the isotherms for NOTT-101.

Unless stated otherwise, all of the characterisation methods were conducted as follows:

The surface area measurements refer to the BET nitrogen specific surface area obtained using the 2010 British Standard Method [150] from low pressure nitrogen sorption measurements on a Micromeritics ASAP 2020 volumetric gas sorption analyser, where ASAP stands for Accelerated Surface Area and Porosimetry system, at 77 K with a 60 minute equilibration time (Section 3.2.3) [151] where the uncertainty is the standard error of the BET measurements. This surface area was calculated using the British Standard guidelines for the BET method [150], with the data points relevant to the linear regression in the 0.05 to 0.3  $P/P_0$  relative pressure range.

The micropore volume measurements were calculated using the Dubinin-Radushkevich (DR) method [144, 152] applied to the nitrogen isotherms at 77 K up to 0.1 MPa, and the pore sizes were calculated using Density Function Theory (DFT) [153], both also measured on the Micromeritics ASAP 2020 volumetric gas sorption analyser. All pore sizes mentioned throughout the thesis refer to the available space for the adsorptive.

The skeletal density is necessary to determine the free space (volume in the sample tube not occupied by the sample) for volumetric data corrections, and was generally measured using a Micromeritics helium pycnometer (Section 3.2.5) at room temperature.

### **3.1.1 TE7 carbon beads**

TE7 carbon beads are a well characterised reference material, sourced from MAST Carbon International, Basingstoke, UK. They are produced from a

carbonised phenolic resin-based material activated at 750 °C in a steam atmosphere.

They have a BET area of  $810 \pm 50 \text{ m}^2 \text{ g}^{-1}$  (where the uncertainty here and elsewhere in this chapter refers to the standard deviation), a main pore size of 0.7 nm, a DR micropore volume of  $0.43 \pm 0.03 \text{ cm}^3 \text{ g}^{-1}$ , and a skeletal density of  $1.90 \pm 0.03 \text{ g cm}^{-3}$  [150].

Samples were degassed for 8 hours at 623 K under vacuum, prior to measurement of high pressure hydrogen sorption isotherms at 77 K, 89 K, 102 K, 120 K, 150 K, 200 K and 295 K up to a maximum pressure of 14 MPa. The temperatures were chosen as a random sample within the range of 77 K (the lowest temperature possible for the measurements) to room temperature.

Throughout the report, the TE7 carbon beads have been utilised as a reference material because they are commercially available, the general characterisation data is available from the supplier, they show batch homogeneity, they are high purity (94.9 +/- 0.8 wt% carbon), there is a very high repeatability of hydrogen isotherms for the same sample as well as for different samples, and the hydrogen isotherms for adsorption and desorption are reversible.

### **3.1.2 AX-21 activated carbon**

AX-21 activated carbon (now commercially known as Maxsorb, from Kansai Coke and Chemicals Co, Amagasaki, Japan) was sourced from Anderson Development Company Inc., Michigan, United States. It is synthesised using petroleum coke as the carbon precursor, and potassium hydroxide activation at 973 K; a process patented by Standard Oil Company, Ohio, United States.

This material has a BET area of  $2,448 \pm 40 \text{ m}^2 \text{ g}^{-1}$ , and a relatively broad pore size distribution compared to the TE7 carbon beads, with the majority of pores being around 1.4 nm, but with approximately 20 % of pores in the mesopore region (between 2 and 50 nm) calculated *via* the Dubinin-Radushkevich-Kaganer (DRK) [154] equation [155]. It has a reported DR micropore volume of  $1.03 \text{ cm}^3 \text{ g}^{-1}$  [149], and a skeletal density of  $2.23 \text{ g cm}^{-3}$ .

Samples were degassed for 12 hours at 473 K under vacuum, prior to measurement of high pressure hydrogen sorption isotherms at 90 K, 100 K, 110 K and 120 K up to a maximum pressure of 18 MPa.

### 3.1.3 MIL-101(Cr)

Chromium (III) Terephthalate metal organic framework  $[\text{Cr}_3\text{O}(\text{bdc})_3(\text{OH})(\text{H}_2\text{O})_2]$ , MIL-101(Cr), (Figure 3.1) (where MIL stands for ‘Matériaux de l’Institut Lavoisier’, and bdc is benzene-1,4-dicarboxylate) was prepared by adapting the method reported previously by Jiang *et al.* [156]:

0.33 g of terephthalic acid  $[\text{C}_6\text{H}_4\text{-1,4-}(\text{CO}_2\text{H})_2]$  was added to 0.8 g chromium (III) nitrate nonahydrate  $[\text{Cr}(\text{NO}_3)_3 \cdot 9\text{H}_2\text{O}]$  in a Teflon-lined autoclave, with 10 mL distilled water and a stirrer bar. This was heated to 453 K and left for 8 hours, before cooling overnight to room temperature. The white powder formed was washed with distilled water and vacuum filtered to form a blue/green suspension, which was centrifuged three times in water for 10 minutes each time at 11,000 rpm and left to dry, resulting in a green solid.

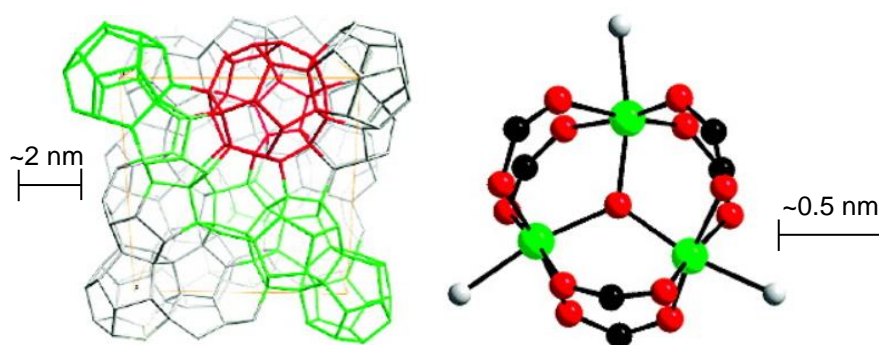


**Figure 3.1 – (Left) The structure of MIL-101(Cr), (right) the inorganic subunit, with the metal (green), oxygen (red) and carbon (black) atoms. Taken from [157].**

Following the synthesis, the material was left with solvent in its pores, rendering it unsuitable for any gas uptake until this solvent is removed. This was achieved by drying in a vacuum oven, and then degassing at 423 K under vacuum for 4 hours, as the structure is stable up to approximately 580 K.

MIL-101(Cr) is a rigid, well studied MOF with benzene-1,4-dicarboxylic acid groups as the linkers, with pore sizes of 0.7 nm, 2.9 nm and 3.4 nm [158], a micropore volume of  $1.9 \text{ cm}^3 \text{ g}^{-1}$  [159], a BET area of  $2,887 \pm 106 \text{ m}^2 \text{ g}^{-1}$  and a skeletal density of  $1.69 \text{ g cm}^{-3}$ . Samples were degassed for 4 hours at 423 K under

vacuum, prior to measurement of high pressure hydrogen sorption isotherms at 77 K, 90 K, 100 K and 110 K up to a maximum pressure of 18 MPa.

### 3.1.4 MIL-53(Al)

Aluminium 1,4-benzenedicarboxylate, [Al(OH)(bdc)] (MIL-53(Al)) (Figure 3.2) was synthesised throughout this project, adapting the synthetic procedure from Loiseau *et al.* [160] using a method derived by Dr. Dongmei Jiang:

0.165 g of terephthalic acid [C<sub>6</sub>H<sub>4</sub>-1,4-(CO<sub>2</sub>H)<sub>2</sub>] was added to 0.376 g aluminium (III) nitrate nonahydrate [Al(NO<sub>3</sub>)<sub>3</sub>·9H<sub>2</sub>O] in a Teflon-lined autoclave, with 10 mL distilled water and a stirrer bar. This was heated to 493 K and left for 8 hours, before cooling overnight to room temperature. The white powder formed was then washed with acetone and vacuum filtered to form a clear liquid, which was centrifuged three times in acetone for 10 minutes each time at 11,000 rpm and left to dry, resulting in a white solid.

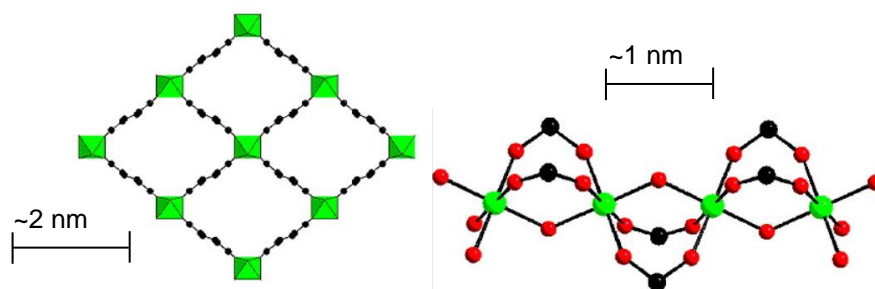


**Figure 3.2 – (Left) The structure of MIL-53(Al), (right) the inorganic subunit, with the metal (green), oxygen (red) and carbon (black) atoms. Taken from [157].**

Similar to the synthesis of MIL-101(Cr) above, the material is left with solvent in its pores, rendering it unsuitable for any gas uptake until this solvent is removed. Solvent removal was achieved by drying in a vacuum oven, and then degassing at 423 K for 4 hours, as the structure is stable up to approximately 560 K.

MIL-53(Al) was chosen due to its propensity for breathing, or pore distortion [161-163]. This behaviour can occur with changes in temperature, pressure, or introduction of a guest molecule, which causes the pores to stretch, reducing the volume within, as seen in Figure 3.3.

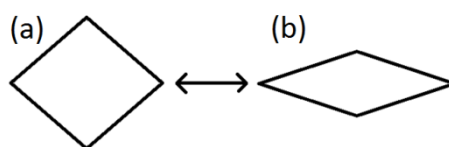


**Figure 3.3 – Representation of the breathing phenomena observed in MIL-53(Al). A large pore, (a), to a narrow pore, (b), transition.**

The pore sizes in MIL-53(Al) vary between 1.7 – 2.1 nm, and 1.3 – 0.7 nm, between the large pore and narrow pore structures respectively, highlighted in the large differences in the XRD patterns of both phases [164], and the material has a BET area of  $1,118 \pm 47 \text{ m}^2 \text{ g}^{-1}$ . It has a micropore volume of  $0.3 \text{ cm}^3 \text{ g}^{-1}$ , and a reported skeletal density of  $1.4 \text{ g cm}^{-3}$  [165]. Samples were degassed for 4 hours at 423 K under vacuum, prior to measurement of high pressure hydrogen sorption isotherms at 77 K, 90 K, 100 K, 110 K and 120 K up to a maximum pressure of 18 MPa.

As the only MIL-53 material used within the study is MIL-53(Al), this will be referred to as just MIL-53 throughout the thesis.

### 3.1.5 NOTT-101

NOTT-101 is a copper based MOF, with the formula  $\text{Cu}_2(\text{tptc})$  (where tptc is terphenyl-3,3',5,5'-tetracarboxylate) (Figure 3.4), and was originally synthesised in Nottingham in 2006 *via* the addition of  $\text{H}_4\text{tptc}$  to copper (II) nitrate [166]. It has an average pore size of 0.7 nm, a BET area of  $2,510 \text{ m}^2 \text{ g}^{-1}$  calculated in the  $P/P_0$  range of 0.05 – 0.15 using a Quantachrome Autosorb-1 gas sorption apparatus at the Chemical and Environmental Sciences Laboratory, General Motors Research and Development Centre, Warren, MI, USA. It has a micropore volume of  $0.9 \text{ cm}^3 \text{ g}^{-1}$  and a skeletal density of  $0.68 \text{ g cm}^{-3}$ .

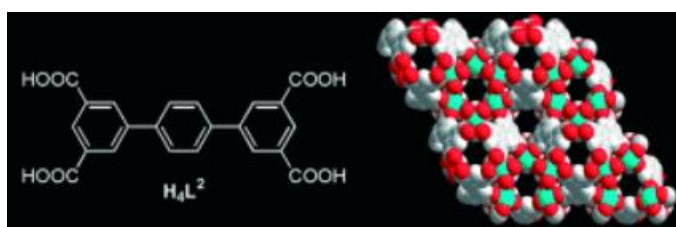


**Figure 3.4 – (Left) the ligand in NOTT-101 and (right) the space-filling representation of NOTT-101. Adapted from [166].**

The hydrogen sorption data was provided by Anne Dailly, also from General Motors Research and Development Centre, in the form of hydrogen isotherm

measurements using a PCT-Pro 2000 from Hy-Energy LLC, at 50 K, 60 K, 70 K, 77 K and 87 K, following activation of the material at 373 K under vacuum [131].

### 3.1.6 ZIF-8

Zeolitic imidazolate framework 8 (ZIF-8) (Figure 3.5) is a MOF that is topologically isomorphous with a sodalite (SOD) zeolite. It is synthesised by adding zinc nitrate tetrahydrate ( $\text{Zn}(\text{NO}_3)_2 \cdot 4\text{H}_2\text{O}$ ) to 2-methylimidazole (H-MeIM,  $\text{C}_4\text{H}_7\text{N}_2$ ) in dimethylformamide (DMF) at 413 K for 24 hours [167]. Chloroform is then added to the vial, resulting in colourless crystals, which are washed with DMF and dried in air.

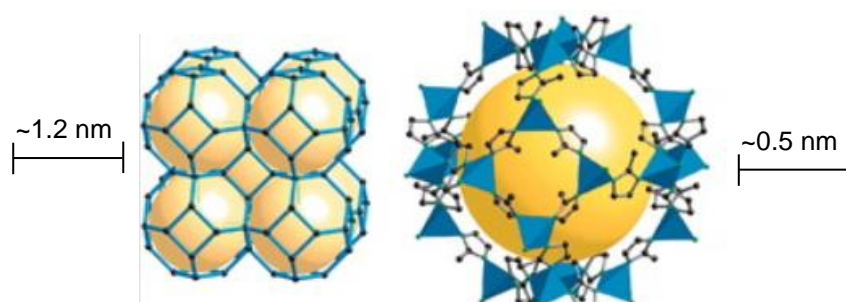


**Figure 3.5 – (Left) the single crystal X-ray structure of ZIF-8, and (right) the largest cage in ZIF-8, with the blue tetrahedral representing  $\text{ZnN}_4$  and the yellow ball depicting the space available for adsorption. Adapted from [167].**

ZIF-8 consists of a tetrahedrally-coordinated zinc centre linked by imidazole, and the pores are 1.2 nm in diameter, connected by small apertures of 0.3 nm. It has a BET surface area of  $1,630 \text{ m}^2 \text{ g}^{-1}$  calculated in the range of  $P/P_0 = 0.01 - 0.1$  [167], a micropore volume of  $0.64 \text{ cm}^3 \text{ g}^{-1}$  [167], and a skeletal density of  $1.4 \text{ g cm}^{-3}$  [165]. It is stable up to 825 K.

ZIF-8 was first reported in 2006 [167], and the hydrogen sorption isotherms were extracted from the literature using EnGauge data-reading software at 50 K, 60 K, 77 K, 100 K and 125 K, following degas at 423 K for 24 hours [168].

### 3.1.7 Summary

Table 3.1 provides a summary of all of the key parameters for each material. As mentioned previously, the measurements for MIL-53 were made by myself, and the rest were either measured by colleagues or received from literature as highlighted individually within sections 3.1.1 to 3.1.6. Errors are included where possible for all values, except where omitted from the literature.

**Table 3.1 – A summary of the key parameters for each of the six materials used throughout the thesis.**

Material	Pore size / nm	BET surface area / m <sup>2</sup> g <sup>-1</sup>	Micropore volume / cm <sup>3</sup> g <sup>-1</sup>	Skeletal density / g cm <sup>-3</sup>
TE7 carbon beads	0.7	810 ± 50	0.43 ± 0.03	1.90 ± 0.03
AX-21 activated carbon	1.4 and 2 to 50	2,448 ± 40	1.03	2.23 ± 0.02
MIL-101(Cr)	0.7, 2.9 and 3.4	2,887 ± 106	1.90	1.69 ± 0.14
MIL-53(Al)	1.7 to 2.1 and 1.3 to 0.7	1,118 ± 47	0.30 ± 0.04	1.40 ± 0.4
NOTT-101	0.7	2,510	0.90	0.68
ZIF-8	1.2 and 0.3	1,630	0.64	1.40 ± 0.4

### 3.2 Characterisation equipment

A variety of equipment was used in order to achieve a full characterisation of the materials. MIL-101(Cr) has been chosen throughout this section to illustrate each characterisation technique, except for the inelastic neutron scattering and helium pycnometry.

#### 3.2.1 X-ray diffraction (XRD)

X-rays are electromagnetic radiation with a wavelength of about 0.1 nm, approximately the same size as an atom, making it suitable for structural studies of materials. XRD is able to measure the spacing between layers of atoms, it can find the crystal structure of an unknown material, it is able to determine the orientation of a single crystal, and it can measure the shape and size of small crystalline regions [169].

XRD utilises Bragg's Law (Equation 3.1) to explain the diffraction of X-rays when hitting the surface of a material [170].

$$n\lambda = 2d\sin\theta \tag{3.1}$$

Where  $\lambda$  is the wavelength of the incident X-ray beam,  $d$  is the spacing between atomic layers in a crystal and  $\theta$  is the angle of the incident X-ray beam, as shown in Figure 3.6. Two incident X-ray beams can either constructively interfere with each other or destructively interfere, all depending on the length of A to B to C in Figure 3.6 and the wavelength of the beam.

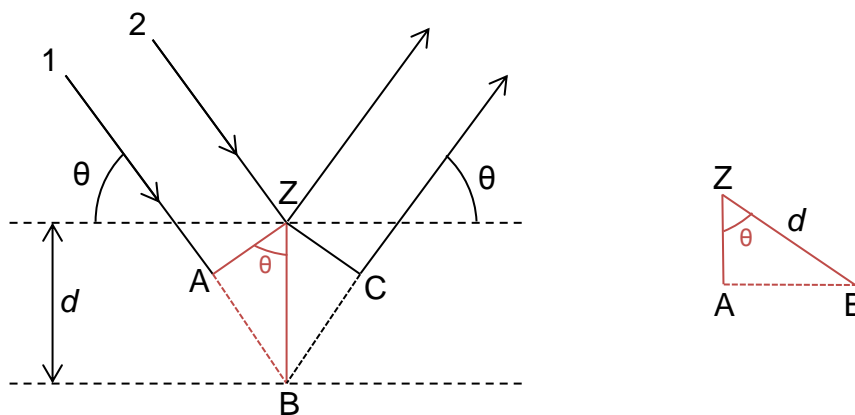
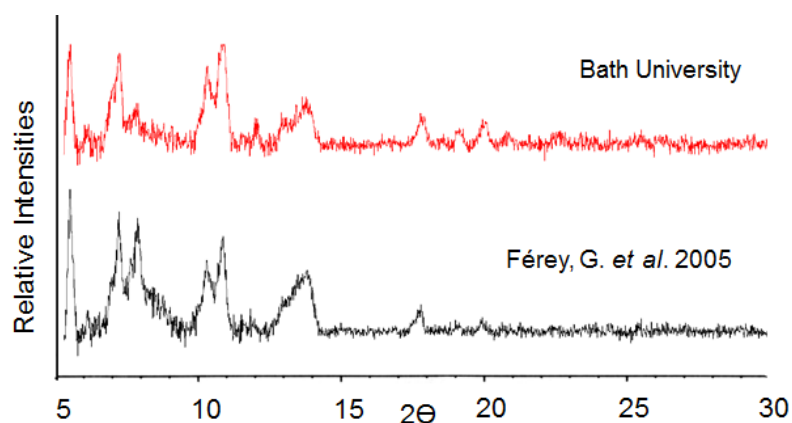


Figure 3.6– An illustration of Bragg's Law. The red triangle on the right is equivalent to the red triangle in the diagram on the left.

In XRD, the diffracted beam is recorded at an angle of  $2\theta$  from the incident beam, which continuously moves to adjust the angle of  $2\theta$  so that a diffraction pattern is recorded at a range of  $2\theta$  values. X-ray diffraction produces an individual pattern for each crystalline solid, making it an effective “fingerprinting” tool.

Two types of XRD experiments were conducted throughout the study.

Powder X-ray diffraction (PXRD) was conducted at the University of Bath. The PXRD machine is used to determine the position of atoms within a crystal. In this study it is of most use in determining whether two different batches of the same material are identical. Measurements were recorded using a Bruker D8 powder diffractometer, fitted with Goebel mirrors, and used  $\text{CuK}\alpha$  radiation at 0.15414 nm. The samples were placed into 0.7 mm diameter Lindemann capillaries and measured with a  $2\theta$  range of 5 to 30 °. The step size was 0.03 ° with a time per step of 0.2 s. An example of the synthesised MIL-101(Cr) XRD against the literature MIL-101(Cr) XRD is shown in Figure 3.7 [158].



**Figure 3.7 – XRD patterns of MIL-101(Cr) synthesised in Bath (red), and from literature (black) [158]. The plots have been separated in y for comparison purposes.**

The other XRD experiments were conducted at high pressures and cryogenic temperatures at the European Synchrotron and Radiation Facility (ESRF) in Grenoble, on machine ID-31. The samples were dried at high temperature and high vacuum ( $10^{-7}$  mbar) prior to collection of synchrotron powder XRD patterns. Samples were held in standard glass capillaries of diameter 0.5 mm. The system was purged with nitrogen before use, and measurements were made at a range of 0 - 60 ° $2\theta$  at a rate of 2°  $\text{min}^{-1}$ . A range of different pressures (0 – 10 MPa) and

temperatures (80 – 300 K) were used throughout the experiment, as observed in Figure 3.8, which shows the spectra for MIL-101(Cr).

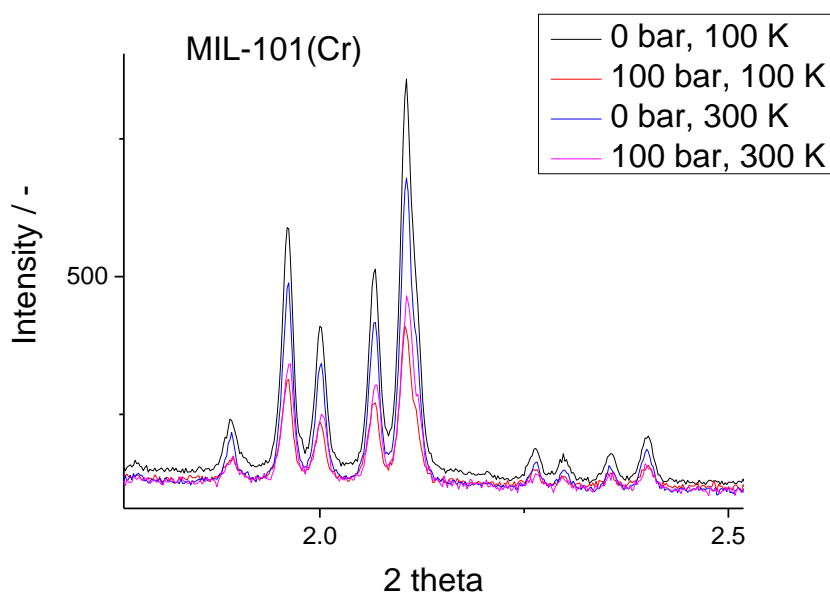


**Figure 3.8 – The XRD patterns for MIL-101(Cr) at varying pressures and temperatures, collected at the ESRF.**

### **3.2.2 Thermogravimetric analysis (TGA)**

The TGA measures the change in mass of a sample as a function of temperature. This is particularly important for porous materials, as it provides the temperature boundaries within which the solvent can be removed from the pores, as well as an indication of the composition and temperature stability of the material. For example, Figure 3.9 shows the TGA for MIL-101(Cr), and it can be observed that the solvent (which is water in this example) has most likely been removed from the pores by 100 °C as the graph starts to level out again, *i.e.* there is a large reduction in the weight loss before 100 °C. It can also be seen that the material most probably decomposes at about 320 °C, due to the large weight loss observed at that temperature. Therefore, from this graph, it can be implied that solvent removal must be between around 120 °C and 300 °C, and that any analysis of the material cannot occur above 300 °C.

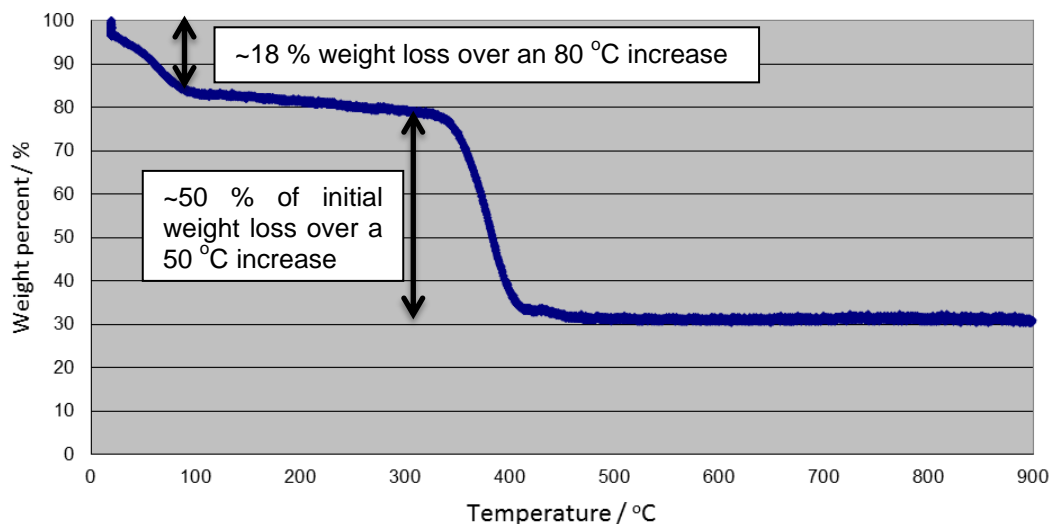


**Figure 3.9 – TGA plot of MIL-101(Cr) with increasing temperature under a nitrogen atmosphere, with a ramp rate of 5 °C min<sup>-1</sup>.**

Thermogravimetric analyses were conducted using a Setaram T92 fitted with a differential thermal analysis head. Samples were heated to 900 °C with a heating rate of 1, 5 or 10 °C min<sup>-1</sup> under an atmosphere of N<sub>2</sub>. Sample sizes of around 0.01 g were used.

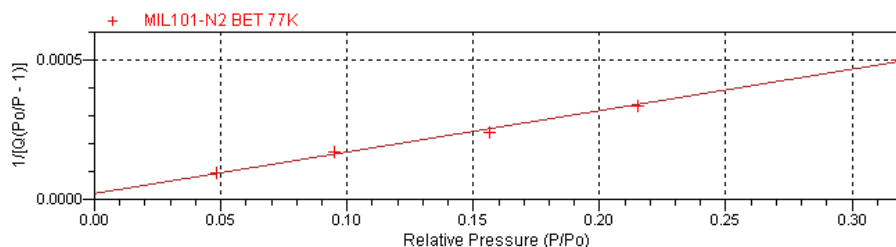
### 3.2.3 Low pressure volumetric gas sorption

Low pressure volumetric gas sorption studies were conducted on a Micromeritics ASAP 2020 (Micromeritics Instrument Corporation, Norcross, GA, USA) volumetric adsorption analyser (up to 0.1 MPa). This machine is particularly useful for measuring the surface area of a sample, by allowing the collection of sorption isotherms over different pressures up to 0.1 MPa. It works by dosing the sample chamber with a known volume of gas at a set temperature and pressure. The amount of gas adsorbed can be calculated by the change in pressure measured. As mentioned previously, the surface area is calculated using the British Standard Method of the BET calculation [150, 171]. The machine has a lower limit of 30 m<sup>2</sup> surface area per sample, and as the minimum surface area of the samples used is 960 m<sup>2</sup> g<sup>-1</sup>, sample sizes of 0.1 g are more than sufficient. Figure 3.10 displays screen shots from the ASAP showing the BET area data for MIL-101(Cr).

Sample: MIL101-N2 BET 77K  
 Operator: VT  
 Submitter: TJM  
 File: C:\2020\DATA\ANNA\000-873.SMP

Started: 25/01/2012 11:50:48PM                      Analysis Adsorptive: N2  
 Completed: 25/01/2012 15:15:06PM                      Analysis Bath Temp.: -195.800 °C  
 Report Time: 26/01/2012 16:11:09PM                      Thermal Correction: No  
 Sample Mass: 0.0551 g                      Warm Free Space: 27.7846 cm<sup>3</sup> Measured  
 Cold Free Space: 86.5741 cm<sup>3</sup>                      Equilibration Interval: 10 s

### BET Surface Area Plot



### BET Surface Area Report

BET Surface Area: 2886.9554 ± 105.8920 m<sup>2</sup>/g  
 Slope: 0.001487 ± 0.000054 g/cm<sup>2</sup> STP  
 Y-Intercept: 0.000021 ± 0.000010 g/cm<sup>2</sup> STP  
 C: 71.235957  
 Qm: 663.1802 cm<sup>3</sup>/g STP  
 Correlation Coefficient: 0.9980034  
 Molecular Cross-Sectional Area: 0.1620 nm<sup>2</sup>

Relative Pressure (P/Po)	Quantity Adsorbed (cm <sup>3</sup> /g STP)	1/[Q(Po/P - 1)]
0.048172369	522.8522	0.000097
0.095089220	615.4765	0.000171
0.156471062	769.5056	0.000241
0.215257243	824.0444	0.000333
0.317569733	926.7022	0.000502

**Figure 3.10 – Screen shots from the ASAP showing the BET data for MIL-101(Cr).**

### 3.2.4 High pressure volumetric gas sorption

High pressure volumetric gas sorption studies were conducted on a Hiden HTP-1 (Hiden Isochema, Warrington, UK) Sieverts-type volumetric gas sorption analyser up to pressures of 20 MPa. High purity hydrogen was used for all of the measurements (99.99996 %, BIP-Plus from Air Products), and a liquid nitrogen bath was used for temperature control for the 77 K isotherms. Prior to each measurement, the samples (typically 0.1 g) were degassed in order to remove impurities from surfaces and pores, applying a minimum equilibration time of 12 minutes. The cryofurnace used was a Hiden liquid nitrogen recirculating cryofurnace with an integral band heater, and was utilised for all temperatures above 77 K. The 77 K isotherms were measured by submerging the sample chamber directly into liquid nitrogen. All isotherms presented in this work

measured using the HTP-1 were fully reversible, and repeat isotherms were reproduced to within 0.3 % of the measured amounts adsorbed. Desorption isotherms were measured for the lowest temperature isotherm of each sample. All isotherms are reported as excess hydrogen uptake in wt% relative to the degassed sample weight. Figure 3.11 shows the isotherms at four different temperatures for MIL-101(Cr).

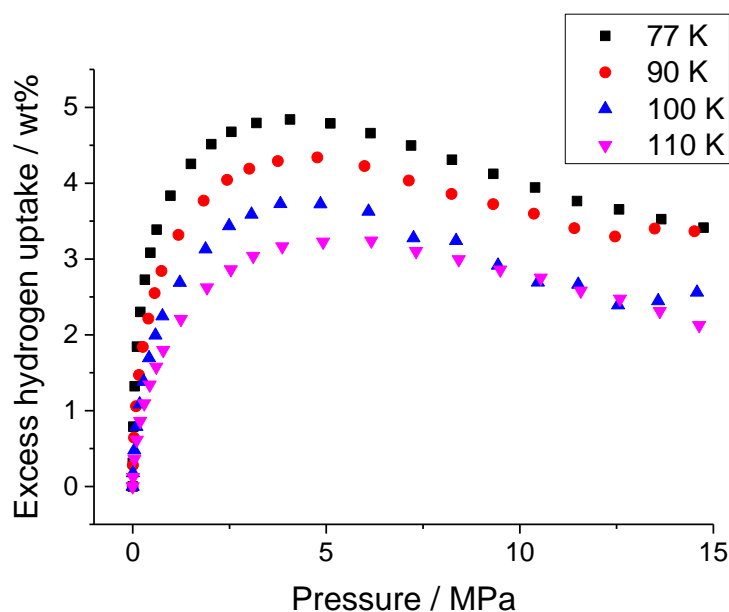


Figure 3.11 – Hydrogen isotherms measured on the HTP-1 for MIL-101(Cr) at different temperatures.

### 3.2.5 Helium pycnometry

The Helium pycnometer (Micromeritics AccuPyc 1330, Micromeritics Instrument Corporation, Norcross, GA, USA) was used to measure the skeletal density of the materials. It works by dosing helium into the sample, and due to the inert nature of the gas, is able to measure the volume unoccupied by the sample, and hence the volume occupied by the sample. The density is determined by dividing the sample mass by the volume occupied by the sample.

### 3.2.6 Inelastic neutron scattering

The inelastic neutron scattering measurements examined in this thesis were conducted on the TOSCA inelastic neutron scattering instrument at ISIS at the Rutherford Appleton Laboratories in Oxfordshire, which has an energy window from -3 meV to 500 meV. The sample (approximately 8 g) was degassed at 623 K for 8 hours at 0.1 MPa, and then loaded into a high pressure (7 MPa) stainless

steel sample can within an argon glovebox. A standard cryofurnace ancillary was used to supply temperature control, and normal hydrogen gas (BOC 99.999 %) was dosed into the sample, where it was thermally equilibrated at 77 K before the pressure was recorded using a baratron and a high-pressure transducer. The data was collected in 700 mA sets, with up to three data-sets being collected at each pressure (0.016, 0.070, 0.160, 0.301, 0.630, 0.998, 2.070 and 3.500 MPa) over collection periods of 8-12 hours. The data was corrected for the presence of terminal hydrogen atoms in the sample by subtraction of 12 hour background scans of the degassed sample at 4 K and 77 K. The data processing was performed using the Mantid software [172].

### 3.3 Analysis

#### 3.3.1 Statistical analysis

All non-linear fitting was performed using Origin 8.5 Pro software (OriginLab Corporation, Massachusetts, United States). This program utilises a Levenberg-Marquardt method of non-linear fitting [173], which combines the steepest-descent method and the Gauss-Newton method to adjust the parameter values to achieve the minimum reduced  $\chi^2$  value (a value relating to the quality of fit). The steepest-descent method uses the gradient of the curve on a graph of  $\chi^2$  vs. parameter to find the nearest local minimum. The problem with this method is that it requires multiple iterations, and may not converge if no local minimum is observed. This is why Origin then goes on to use the Gauss-Newton method, which uses conjugate directions as opposed to the local gradient that the steepest-descent uses, resulting in far less iteration for specific functions [174, 175]. Up to 400 fitting iterations were carried out with a tolerance of  $10^{-9}$ . Origin is also capable of running simplex fitting [176], the method of which was originally published in 1965, and uses an algorithm instead of the gradient, making it a better method for non-smooth functions. There were no limits placed on any of the variables in the fitting conducted throughout this thesis.

The error bars shown in the graphs throughout the results and discussion chapter of the thesis are calculated by an estimate of the standard error, which is the standard deviation of the mean divided by the root of the sample size; representing how well the sample mean approximates the population mean.

Origin allows for a variety of methods for observing the quality of the fitting, including the residual sum of squares (RSS), the reduced  $\chi^2$  value, the root mean square residual (RMSR), the  $R^2$  value and the adjusted  $R^2$  value (both corrected and uncorrected), calculated as seen in Equations 3.2 – 3.7 respectively [158, 159].

$$RSS = \chi^2 = \sum_{i=1}^n w_i (y_i - \hat{y}_i)^2 \quad 3.2$$

$$\text{reduced } \chi^2 = \frac{RSS}{DOF} = \frac{1}{n-p} \sum_{i=1}^n w_i (y_i - \hat{y}_i)^2 \quad 3.3$$

$$RMSR = \sqrt{\text{reduced } \chi^2} = \sqrt{\frac{RSS}{DOF}} = \sqrt{\frac{1}{n-p} \sum_{i=1}^n w_i (y_i - \hat{y}_i)^2} \quad 3.4$$

$$\bar{R}^2 = 1 - \frac{RSS}{TSS} = 1 - \frac{\sum_{i=1}^n w_i (y_i - \hat{y}_i)^2}{\sum_{i=1}^n w_i (y_i - \bar{y})^2} \quad 3.5$$

$$\text{corrected adjusted } \bar{R}^2 = 1 - \frac{RSS / DOF}{TSS / DOF} = 1 - \frac{(\sum_{i=1}^n w_i (y_i - \hat{y}_i)^2)(n-1)}{(\sum_{i=1}^n w_i (y_i - \bar{y})^2)(n-p)} \quad 3.6$$

$$\text{uncorrected adjusted } \bar{R}^2 = 1 - \frac{(\sum_{i=1}^n w_i (y_i - \hat{y}_i)^2)(n-1)}{(\sum_{i=1}^n w_i y_i^2)(n-p)} \quad 3.7$$

where  $w_i$  (-) is the weighted fitting (Origin is able to specify which weighting method can be used for each y data, however for this study no weighting was necessary),  $i$  (-) is the data point,  $y_i$  (unit of data value) is the data value,  $\hat{y}_i$  (unit of data value) is the function value, DOF (-) is degrees of freedom,  $n$  (-) is the number of data points,  $p$  (-) is the number of parameters, TSS (unit of data value squared) is the total sum of squares and  $\bar{y}$  (-) is the series mean.

The RSS shows the discrepancy between the entire fit data and the actual data, and is also known as the  $\chi^2$  value. The reduced  $\chi^2$  value is the RSS divided by the DOF, with the DOF being the number of data points minus the number of parameters. As mentioned before, the reduced  $\chi^2$  is the quantity that is minimized throughout the iteration, however this is not always the best measure of fit, for example if the y-data is scaled, then the reduced  $\chi^2$  will be also scaled. The closer the reduced  $\chi^2$  value is to 0, the better the fit. The RMSR is the square root of the reduced  $\chi^2$  value.

The adjusted  $R^2$  value differs to the standard  $R^2$  by incorporating the degrees of freedom. This stops a scenario occurring where the goodness of fit appears to increase just by adding more parameters, even though it does not increase in a practical sense. The uncorrected adjusted  $R^2$  value does not account for the

mean, whereas the corrected one does. The  $R^2$  value lies between 0 and 1, but the closer to 1 it is, the better the quality of the fit.

### 3.3.2 Computer simulations

Grand Canonical Monte Carlo (GCMC) simulations were used to produce the computational results that are presented in Chapter 4. The specific code used was Simcheque, which was constructed and remodelled by students in the group led by Professor Suresh Bhatia in the University of Queensland. The supercomputer used to run the simulations was called Barrine, also from the University of Queensland, and a network file transfer application, PuTTY [177], was used to transfer the files to Barrine. The program used to test the code was Microsoft Visual Studio 2008 [178], the files were transferred to PuTTY *via* WinSCP [179]. The graphics presented were produced using Visual Molecular Dynamics [180].

The code accounted for quantum effects using the method by Cracknell [181], and the 3-point hydrogen model was used instead of a spherical model, also taken from Cracknell [181]. The 3-point model accounts for 3 different sections of the hydrogen molecule, each hydrogen atom and a centre of mass, as seen in Figure 3.12.

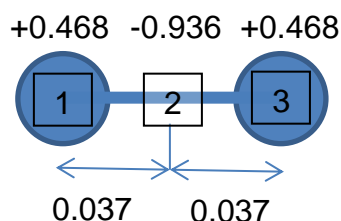


**Figure 3.12 – An illustration of the 3-point hydrogen model. Points 1 and 3 are the hydrogen atoms, and point 2 is the centre of mass. The charges used for each point are labelled above in units of elementary charge, and the distances between the points are labelled below in nanometers.**

The hydrogen molecule was assumed to be rigid, and charge was distributed throughout the molecule as observed in Figure 3.12. The pore width was varied, and the x and y dimensions were set as 4 nm. Simulations were done on both single walled slit pores and infinitely thick pore walls of pure graphite, but due to the low surface area of the TE7 carbon beads (the adsorbent chosen to compare

to the simulation results) the infinite layer pore wall model was deemed more accurate.

The number of simulation steps for each point was 50,000,000, with the chance of creation, deletion and translation set as 0.3, 0.3 and 0.4 respectively. The maximum rotation and translation were set at 0.05 nm, and the cut off radius was 1.95 nm. Each simulation was repeated without the host file in order to get an accurate value of the pressure. Each pore was split into 50 equal segments in order to get the density variation within the pores.

## **Chapter Four**

### **Results and discussion**

## 4 Results and discussion

This results and discussion chapter is split into five sections, as shown in Figure 4.1. The first section (Section 4.1) highlights the development of the model used to fit to the excess experimental isotherms of the six materials mentioned in the methodology (Chapter 3). The development introduces a hydrogen density variation within the pores of the materials, and the model is compared to the initial model found in literature. The developed model, or density variation (DV) model, allows for an estimation of the density of the hydrogen in the adsorbate, a quantity which cannot easily be determined experimentally.

Section 4.2 focusses on improving the DV model by expanding the parameters within it. This is done with the aim of understanding more about the fundamentals of the adsorption process, as well as attempting to make the model independent of pressure and temperature so that it can be used to estimate the hydrogen uptake at conditions that cannot be reached in the laboratory. The expansion specifically includes the pressure and temperature variation of the adsorbate density, the pressure and temperature variation of the pore volume, and a comparison of the use of different isotherm equations within the model.

Section 4.2 results in a final equation which is thought to be suitable for use on all hydrogen isotherms of any material, and Section 4.3 focusses on the verification of this model, both by inelastic neutron scattering and by computer simulation. Both of these techniques are able to estimate the total or absolute amounts of hydrogen within a system, which can then be compared to the total or absolute amounts as calculated *via* the DV model. The inelastic neutron scattering experiments were conducted at the Rutherford Appleton Laboratories in Oxfordshire, and were able to successfully verify the model for the absolute quantity of hydrogen, but also resulted in some unexpected and unusual results about the density of the hydrogen in the pore. The computer simulations were conducted at the University of Queensland in Brisbane, Australia, focusing on hydrogen adsorption in a slit pore, and were compared to the total uptake modelled on the TE7 carbon beads.

Section 4.4 develops the physical science aspect of adsorption into more of an engineering focus, calculating the amount of hydrogen that could be stored *via* adsorption in a tank, but still utilising the DV model. It explains in detail a method

of comparing the amount of hydrogen stored *via* physisorption to the amount of hydrogen stored *via* compression in a tank at the same conditions, and provides the conditions at which more hydrogen can be stored *via* adsorption than *via* compression.

The final section (Section 4.5) expands on the work conducted in Section 4.4 to allow for a comparison between the amount of energy stored *via* hydrogen (stored by both adsorption and compression) to that of other storage systems such as batteries and standard jet fuel. The use of hydrogen stored *via* adsorption for aviation is then briefly reviewed, including the use of adsorbents in “cryo-charging” a tank, and a calculation into the amount of recoverable hydrogen.

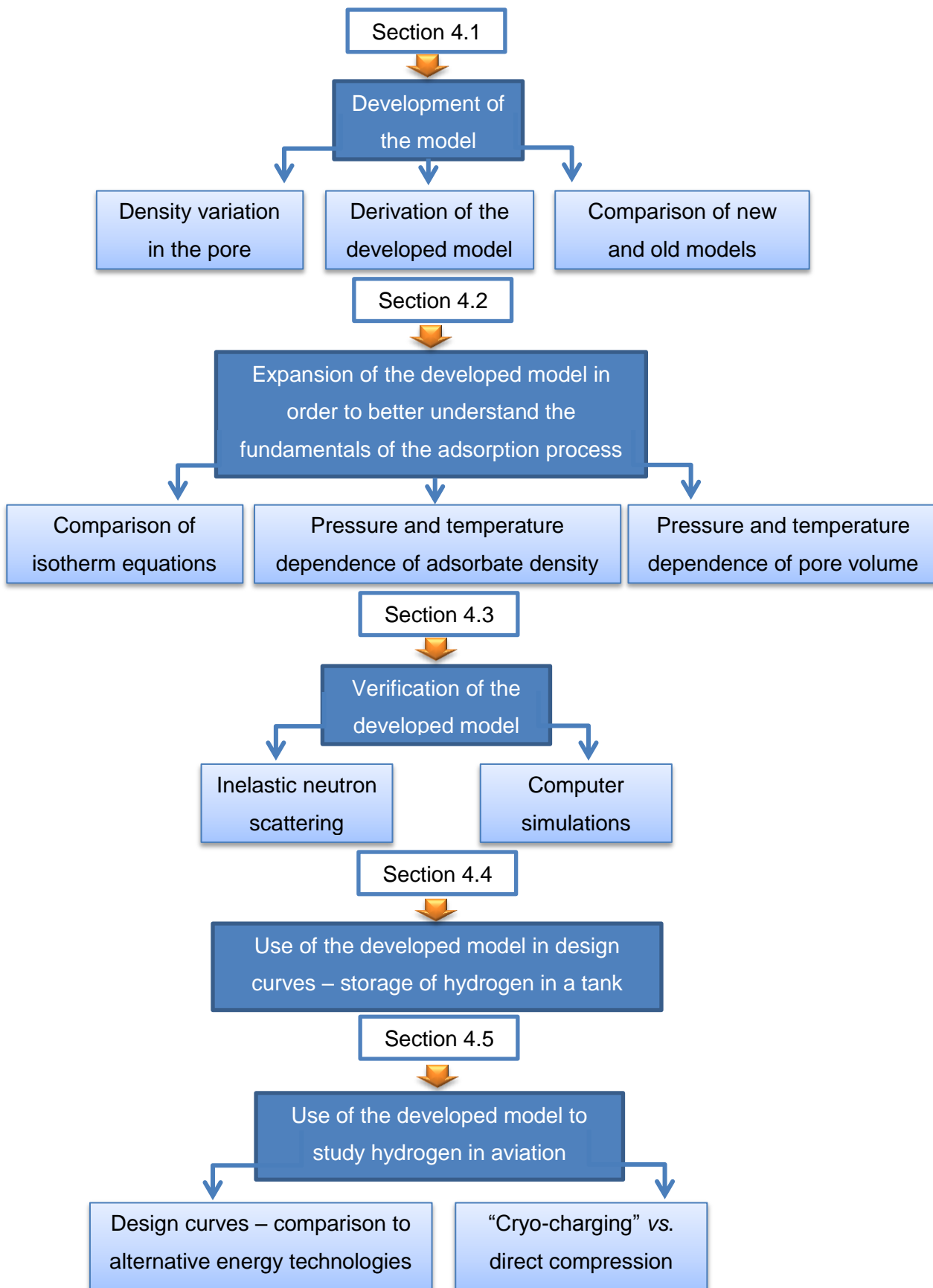


Figure 4.1 – A flow chart showing the content covered within the different sections of the results and discussion chapter.

## **4.1 Development of the initial model**

This section focuses on the development of the initial model (Equation 2.20) used in the literature to fit to experimental excess isotherms, as detailed in the background. The principle behind developing this model is that the hydrogen is thought to have a varying density profile inside the pores of materials due to the different degrees of interaction with the surface of the material. As there are only weak van der Waals interactions between the hydrogen and the material, any more than one layer of hydrogen from the surface would be expected to have very little interaction at all with the surface, as the attractive field would have rapidly diminished. Therefore, pores larger than twice the van der Waals diameter of hydrogen (0.22 nm) [182], would be expected to contain hydrogen both experiencing interaction with the surface at a high density, and hydrogen not experiencing this interaction, or experiencing it to a lesser extent, at a lower density.

The section will include the choice of density variation within the pore used to develop the initial model, the derivation of the developed 'density variation' model and a comparison between the initial and the density variation models. This work has been published in the Journal *Adsorption* [183].

### **4.1.1 Density variation of hydrogen within the pores**

The density variation of hydrogen within the pores of a material is very difficult to accurately determine experimentally, but simulation methods that can be used to estimate it are available.

The simulation method chosen throughout this thesis was Grand Canonical Monte Carlo (GCMC) simulation studies on hydrogen adsorption in slit pores, details of which can be found in Sections 3.3.2 and 4.3. One important outcome of these simulations is that they provide the density variation of hydrogen within the pores at any given volume, pressure and temperature. Simulations were conducted using slit-shaped pores with walls of pure graphene, the pore widths ranging between 0.3 and 0.7 nm, at pressures between 0 and 20 MPa and at temperatures between 77 and 298 K. The density of the hydrogen within the pore is shown in Figure 4.2 for the different pore widths at 77 K and 2 MPa. The same trends are observed at the other pressures and temperatures studied.

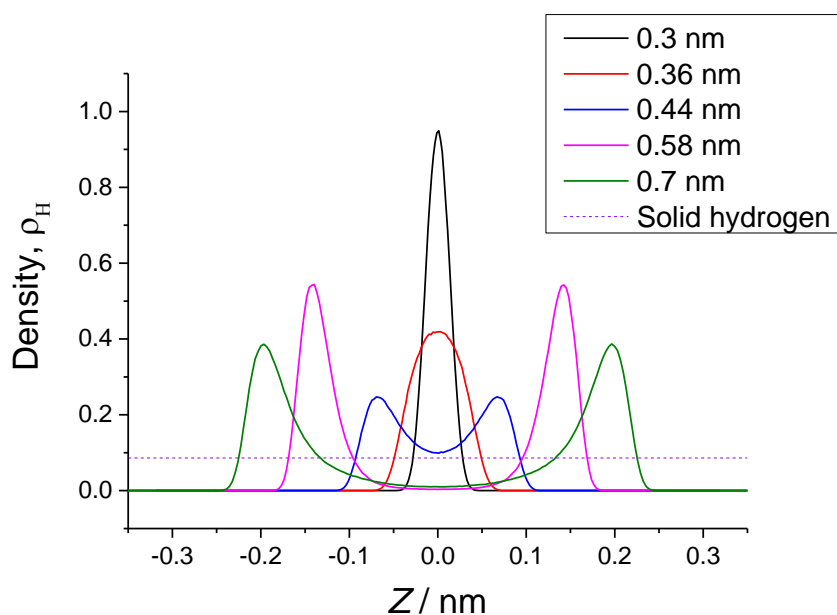


**Figure 4.2 – The density profile of hydrogen at 2 MPa and 77 K inside slit pores of infinite width walls of pure graphite, with different pore widths obtained using molecular simulations. The dotted line represents the density of solid hydrogen.  $Z$  is the distance from the centre of the pore.**

Figure 4.2 shows that for the pores that were simulated to be smaller than 0.44 nm, there is only one layer of hydrogen, with the highest density right in the centre of the pore. For the simulations using pore widths of 0.44 nm and larger, two layers of hydrogen can be observed.

It is also worth noting that the density of the hydrogen within the pores seems to significantly exceed that of the solid density of hydrogen at 0 MPa and 4 K. This phenomenon will be discussed in detail in Section 4.3, and is due to the large number of segments used to calculate the density within the simulation, affecting the absolute density values but not the relative intensities of the peaks.

Larger pore sizes would be expected to contain more than two layers of hydrogen, with the closest layer to the walls of the pore having the highest density, and the density decreasing for each subsequent layer, due to the decrease in interaction between the hydrogen and the surface of the material. This is highlighted by various papers in literature within which computer simulations are used to observe the density of hydrogen in larger pores, for example in pores up to 2.4 nm in single-walled carbon nanotubes [184], up to 3 nm in graphitic nanofibres [185], and up to 2.7 nm in single-walled carbon nanotubes [186]. They all contain more than two layers of hydrogen in the pore, as depicted in Figure 4.3.

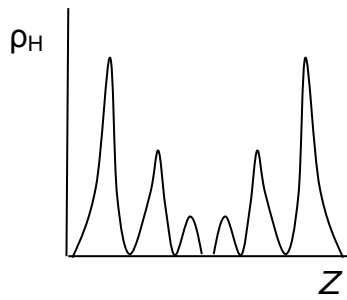


**Figure 4.3 – An illustration of a density profile of hydrogen inside a large pore.  $\rho_H$  is the density of the hydrogen and  $Z$  is the distance from the left-hand pore wall.**

However, even though the large pores show multiple layers of hydrogen at different densities, the pores that are of greatest interest for hydrogen adsorption are less than 1 nm in width [187-189]. Taking this into account, as well as the simplicity required of the derivation, a compromise was made and a density variation allowing for only two different regions of hydrogen in the pore, the adsorbate and the adsorptive, was chosen, as highlighted in Figure 4.4. This shape allows for an accurate determination of the density of the adsorbed hydrogen for one or two layers, as in both these cases there are two main densities of hydrogen, and is a lot more realistic than just assuming a single density within the pores.

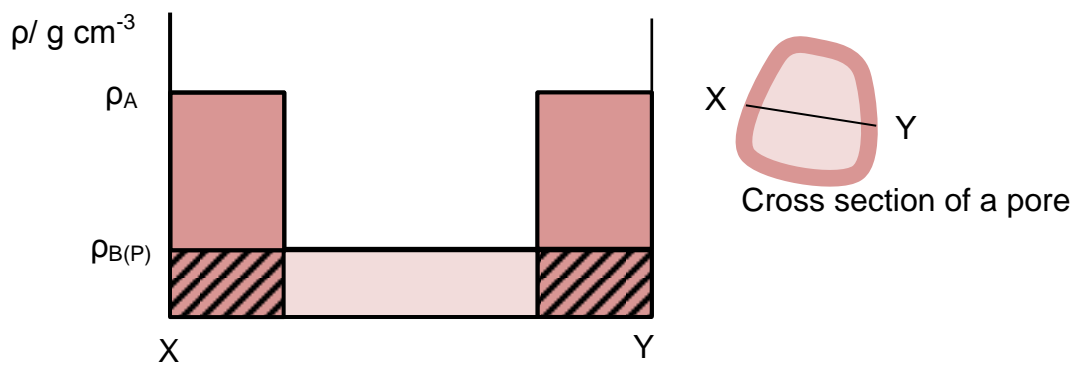


**Figure 4.4 – The density profile of hydrogen in a pore, utilised for the developed model.  $\rho$  ( $\text{g cm}^{-3}$ ) depicts the density,  $\rho_A$  ( $\text{g cm}^{-3}$ ) is the mass density of the adsorbate, and  $\rho_{B(P)}$  ( $\text{g cm}^{-3}$ ) is the mass density of the bulk hydrogen within the pore.**

It can be observed from Figure 4.4 that the density variation allows for two different densities of hydrogen within the pore, a density of the adsorbate,  $\rho_A$  ( $\text{g cm}^{-3}$ ), and a density of the bulk hydrogen,  $\rho_{B(P)}$  ( $\text{g cm}^{-3}$ ). As mentioned in Chapter

2, there are three distinguishable quantities of hydrogen within a pore; the excess, the absolute and the total.

The plain dark pink area in Figure 4.4 indicates the excess uptake,  $m_E$  (wt%), the dark pink area with diagonal lines indicates the bulk amount of hydrogen that would be within the area of the adsorbate with no interactions between the hydrogen and the pore walls,  $m_{B(A)}$  (wt%), and the light pink area plus the dark pink area with diagonal lines indicates the bulk amount of hydrogen in the pore,  $m_{B(P)}$  (wt%). The total amount of hydrogen within the pore ( $m_T$  (wt%)) is the dark pink, plus the dark pink with diagonal lines, plus the light pink areas, and the total amount of hydrogen within the adsorbate (absolute amount,  $m_A$  (wt%)), incorporates the areas which are dark pink plus the dark pink with diagonal lines.

The following diagram gives a detailed description of the system used in the new model as a whole, including the key nomenclature. The new model will be referred to as the density variation model, or the DV model for short.

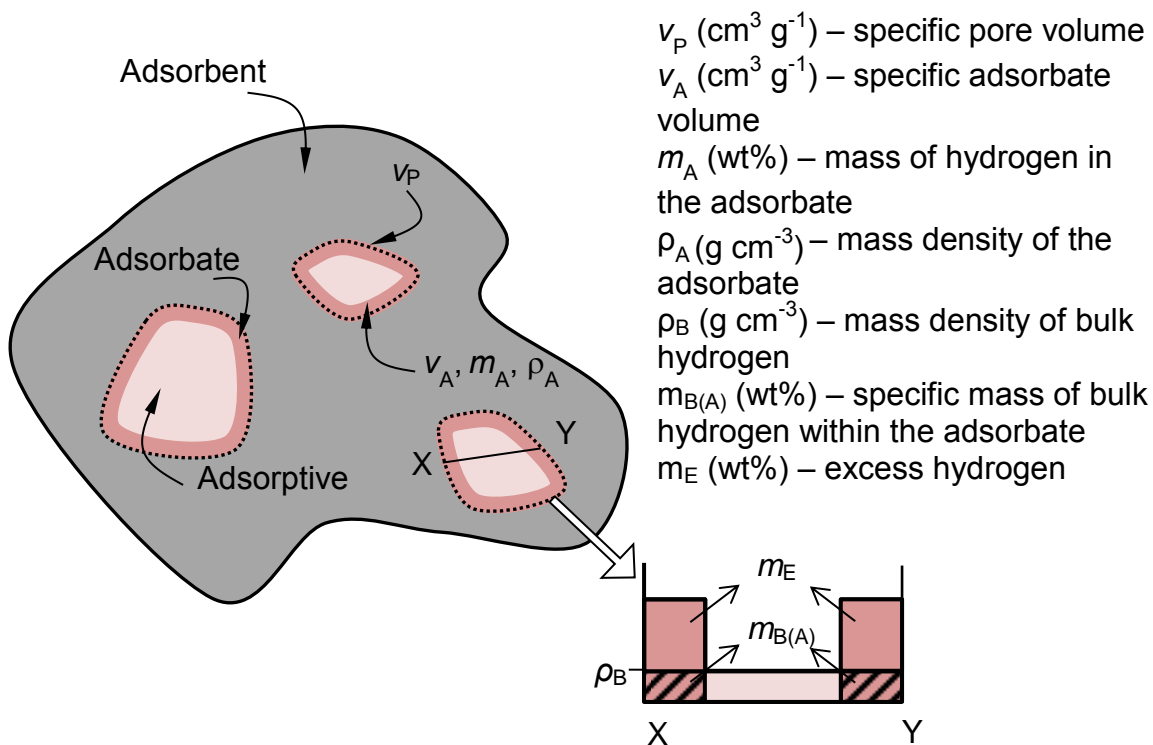


Figure 4.5 – An overview of the system and the nomenclature used for the new model. The dark grey area represents the adsorbent. The smaller diagram at the bottom shows the density of the hydrogen within the cross-section of a pore and highlights the other nomenclature required for the derivation of the new model.

#### 4.1.2 Derivation of the density variation model

Because the excess hydrogen is a section of the adsorbate, it can be stated that the excess is equal to the absolute amount of hydrogen in the adsorbate,  $m_A$  (wt%), minus the bulk amount of hydrogen in the adsorbate,  $m_{B(A)}$  (wt%). Therefore,

$$m_E = m_A - m_{B(A)} \quad 4.1$$

where

$$m_A = 100\rho_A v_A \quad 4.2$$

and

$$m_{B(A)} = 100\rho_B v_A \quad 4.3$$

Therefore, substituting Equations 4.2 and 4.3 into 4.1 gives

$$m_E = 100\rho_A v_A - 100\rho_B v_A \quad 4.4$$

$$m_E = (\rho_A - \rho_B)100v_A \quad 4.5$$

The bulk density,  $\rho_B$  ( $\text{g cm}^{-3}$ ), can again be substituted by using Equation 2.18 as done for the original equation

$$\rho_B = \frac{1}{Z} \frac{PM}{RT} \quad 2.18$$

and  $Z$  is found using a rational approximation to the Leachman 2009 equation of state, currently the best available for hydrogen [190]. It is implemented in the REFPROP software [191], and is available through the National Institute of Standards and Technology (NIST) Chemistry Webbook [192]. The rational approximation uses a ratio of two quadratics with respect to pressure, as done previously [193], more information on which can be found in Supplementary Information A.

The fractional filling can be estimated as a ratio of the adsorbate volume and the pore volume, assuming that the density of the adsorbate does not increase with pressure

$$\Theta_A = \frac{v_A}{v_P} \quad 4.6$$

Therefore, substituting Equation 4.6 and 2.18 into Equation 4.4 gives

$$m_E = \left(\rho_A - \frac{1}{Z} \frac{PM}{RT}\right) 100 v_P \Theta_A \quad 4.7$$

A comparison between the initial model (Equation 2.20) and the DV model (Equation 4.7) was then conducted, shown here using the TE7 carbon beads and the Tóth isotherm equation (observed in Section 4.2.1.2, Equation 4.11) as an example. For the initial model,  $m_A^{\max}$  (wt%),  $v_A$  ( $\text{cm}^3 \text{g}^{-1}$ ) and  $b$  ( $\text{MPa}^{-1}$ ) and  $c$  (-) (the heterogeneity parameter within the Tóth equation, explained in Section 4.2.1.2) from the Tóth equation were allowed to vary with temperature. For the DV model,  $\rho_A$  ( $\text{g cm}^{-3}$ ),  $v_P$  ( $\text{cm}^3 \text{g}^{-1}$ ) and  $b$  ( $\text{MPa}^{-1}$ ) and  $c$  (-) from the Tóth equation were allowed to vary with temperature. Only the 89 – 150 K isotherms were included in this study, as preliminary fits of the model to isotherms at the higher temperatures showed very unlikely values for the pore volume and the adsorbate density. This is because at high temperatures the bulk density is negligible, meaning that the equation reduces down to approximately

$$m_E \approx \rho_A v_P \Theta_A \quad 4.8$$

where  $\rho_A$  ( $\text{g cm}^{-3}$ ) and  $v_P$  ( $\text{cm}^3 \text{g}^{-1}$ ) are both variables in the fit, allowing them to take an infinite number of values. The 77 K isotherm was not used due to the unexpected cross-over of the 77 K isotherm with three of the higher temperature isotherms for the TE7 carbon beads (Figure 4.6). This is likely to be due to the different set-up required for the collection of the 77 K isotherm on the volumetric gas analyser, due to the requirement of submersion into liquid nitrogen, necessary for temperature control (as detailed in Section 3.2.4). A correction has been made to account for this difference in set up, however it clearly has not been fully successful.

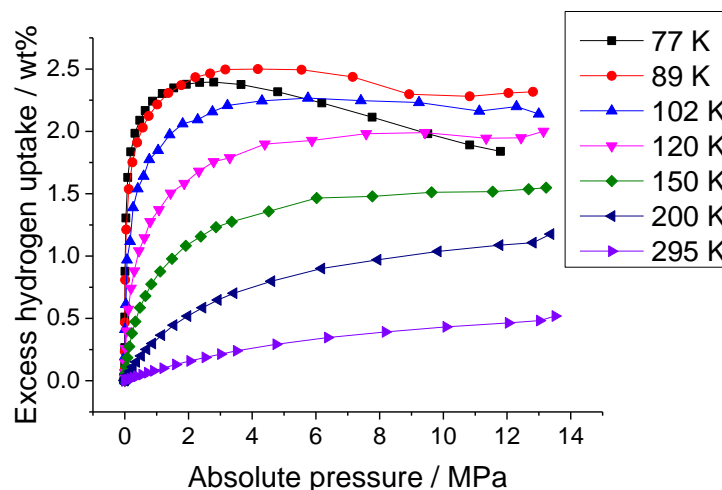


**Figure 4.6 – The excess hydrogen uptake with pressure at different temperatures for the TE7 carbon beads. Lines joining the points are to guide the eye.**

The root mean square residual (RMSR (wt%)), which is explained in detail in the methodology (Section 3.3.1), was used as a method of observing the quality of fit for the comparison, with lower values indicating a better quality of fit.

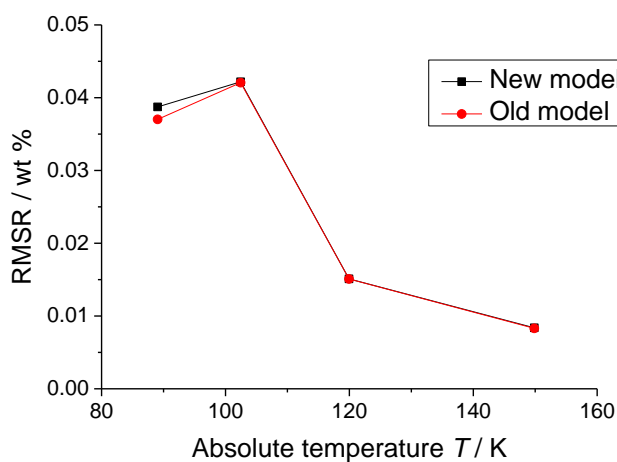


**Figure 4.7 – A comparison of the quality of the fit of the initial and DV models on the TE7 carbon bead isotherms at various temperatures using the Tóth isotherm equation. Lines joining the points are to guide the eye.**

The same comparison was conducted on the other materials discussed in the methodology (Section 3.1), and bias was examined for all of the fits, as well as the use of other isotherm equations within the model. The results of all of these fits can be found in Supplementary Information B. As observed in Figure 4.7 and Supplementary Information B, both models appear to show very similar quality of fits for all isotherm equations (particularly as the scale is so small) as well as

having very similar bias. The initial model appears to show a slightly better fit to some of the materials over the DV model.

However, the DV model does have some major advantages over the initial model. The chief advantage of the DV model is its ability to distinguish between the density of the adsorbate and the density of the bulk hydrogen within the pore, as opposed to the initial model which amalgamates these two values into one. This results in a far more detailed understanding of the density of the adsorbed hydrogen, a value which is difficult to accurately determine experimentally. Another advantage of the DV model is the ability to use it to calculate the absolute and the total amounts of hydrogen in the system (as defined in Sections 2.4 and 0), as opposed to the initial model from which only the total amount of hydrogen can be calculated. This is because for the subsequent conversion of the excess to the absolute amount of hydrogen, an estimate of the adsorbate density is required [194]. As this cannot be calculated in the initial model, the limiting density is generally approximated to that of liquid hydrogen (about  $70 \text{ kg m}^{-3}$ ) within literature [53, 195].

Therefore, even though the quality of the fits are marginally worse for some materials using the DV model, the additional advantage gained from being able to determine the density of the adsorbate is more significant for this work, and so the DV model will be used for all subsequent studies.

#### 4.1.3 Absolute and total hydrogen uptake

As mentioned previously, the DV model can also be used to calculate the absolute and the total amounts of hydrogen. An example is shown below using the TE7 carbon beads. The DV model was fit to the TE7, 89 K excess isotherm using the Tóth isotherm equation and without placing any limits on the variables. The parameters from the fit were then used in the equations for  $m_T$  and  $m_A$  (Equations 4.9 and 4.10 respectively), which were derived fundamentally.

$$m_T = m_E + 100\rho_B v_P \quad 4.9$$

$$m_A = 100\rho_A v_P \Theta_A \quad 4.10$$

The difference between  $m_T$  (wt%),  $m_A$  (wt%) and  $m_E$  (wt%) can be observed in Figure 4.8. The trends observed in Figure 4.8 are exactly what would be expected,

with the total uptake being higher than the absolute amount in the adsorbate, which is higher than the excess.

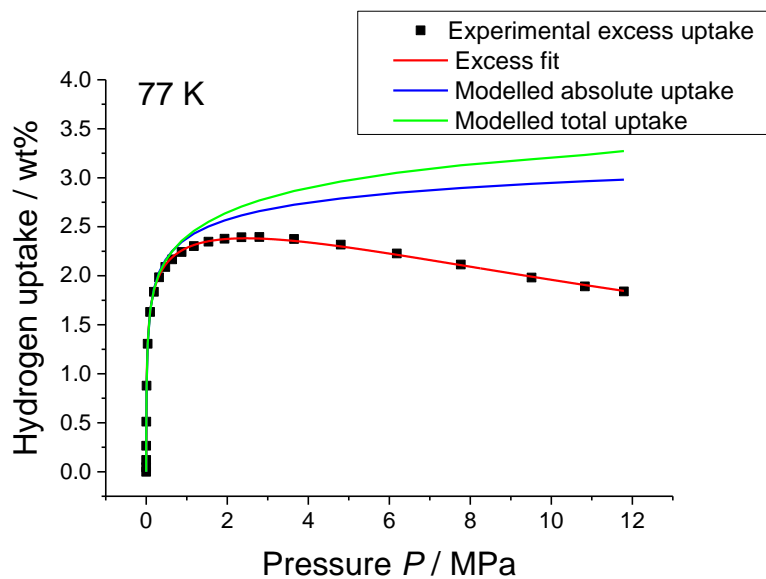


Figure 4.8 – A comparison of the total, absolute, and excess quantities of hydrogen within the TE7 carbon beads at 77 K.

#### 4.1.4 Conclusion

A new model has been derived to fit to experimental hydrogen excess isotherms that accounts for a density variation within the pores of materials. The quality of the fits of this model to experimental isotherms has been shown to be comparable to the original model used in literature, as well as allowing for an estimated value of the density of the adsorbate. The excess, absolute and total amounts of hydrogen have been distinguished and compared.

From here onwards in the thesis, only the DV model will be utilised for fitting to excess hydrogen isotherms.

## 4.2 Detailed analysis of the density variation model

This section will concentrate on each parameter within the DV model in detail to ascertain if the hydrogen adsorption process inside the pores of the materials can be better understood. The trends in pressure and temperature of each parameter will be observed, in an attempt to set each parameter within the model independent of both pressure and temperature, so that the DV model can be used to predict the uptake at conditions that cannot be reached experimentally.

$$m_E = \left(\rho_A - \frac{1}{Z} \frac{PM}{RT}\right) 100 v_P \Theta_A \quad 4.7$$

In Equation 4.7, the known parameters are the pressure,  $P$  (MPa), the molar mass,  $M$  ( $\text{g mol}^{-1}$ ), the molar gas constant,  $R$  ( $\text{MPa cm}^3 \text{K}^{-1} \text{mol}^{-1}$ ), the temperature,  $T$  (K) and the compressibility factor,  $Z$  (-), although  $Z$  is specific for each temperature. That leaves the adsorbate density,  $\rho_A$  ( $\text{g cm}^{-3}$ ), the pore volume,  $v_P$  ( $\text{cm}^3 \text{g}^{-1}$ ) and the fractional filling,  $\Theta_A$  (-) for more detailed consideration.

The results for the comparison of the isotherm equations shown in this section are published in a paper in the Journal *Adsorption* [183].

### 4.2.1 A comparison of isotherm equations, $\Theta_A$

#### 4.2.1.1 Introduction

As mentioned in the background, there are many different isotherm equations which can be input into the DV model. Various studies have been conducted comparing a few isotherm equations to the isotherms of a small number of materials; for example, Saha *et al.* used both the Langmuir and the Freundlich equations in the study of MOF-177 [196], and again compared the Langmuir, Freundlich, Sips and Tóth equations (detailed later in the section) in the study of metal benzenetribenzoate MOFs [197]. However, there has been no complete comparison of the inclusion of these equations into a model, and then individually being fit to a variety of different types of materials in order to see if the results of the fits can be justly compared. This is particularly important, as in literature different isotherm equations are chosen, seemingly randomly, in order to calculate the total uptake. For example, Lin *et al.* use the Tóth equation in order to calculate the total uptake in the NOTT MOFs [198], whereas Kaye *et al.* use the Sips

equation in a study to calculate the total uptake in a Prussian blue analogue [199]. Consequently, the total uptake of these materials might not be comparable if the Tóth equation and the Sips equation display vastly different results.

Therefore, an initial review of the isotherm equations used in literature was conducted, and a choice of the top 8 most suitable for the study was made, based on the suitability of the equations for hydrogen adsorption, and the differences between the equations to ensure a broad comparison. Initial fits were then conducted on every isotherm of each material mentioned in the methodology (Section 3.1) individually, using each isotherm equation within the DV model, and the quality of the fits was observed. Following this, the temperature dependence of the adsorbate density and pore volume from each individual fit was considered in order to allow global fits of the inclusion of each isotherm equation within the DV model to every material. The global fits allowed for a direct comparison of the suitability of the isotherm equations to each different material, and conclusions were drawn from these results.

#### **4.2.1.2 Variables chosen for the comparison of isotherm equations**

For this study, the six different materials described in the methodology (Section 3.1) were all used, and eight different isotherm equations, all of which have a finite limit at very high pressures. Preliminary work displayed the ability of the eight equations within the DV model to fit to the isotherms of each material, that they are mostly well known equations, that they all advocate different surface energy distributions and that they have a range of numbers of parameters. The number of parameters is an important quantity as the most successful equation to use for fitting to hydrogen isotherms would be one that fits the data well but with the least number of parameters, all of which must display realistic values. This follows Occam's razor, which states that when choosing between hypotheses, the one with the fewest assumptions should be chosen [200].

1) Langmuir equation [135]

$$\Theta_A = \frac{bP}{1+bP} \quad 2.1$$

The Langmuir equation is described in detail in the background in Section 2.4. It assumes a homogeneous adsorbate surface, and accounts for only a monolayer formation of hydrogen. It has one unknown parameter,  $b$  ( $\text{MPa}^{-1}$ ), describing the affinity that the hydrogen has for the surface, aptly named the affinity parameter. The larger the value of  $b$ , the greater the affinity that the hydrogen has to the surface, and  $b$  is thought to follow an Arrhenius relationship with temperature (Equation 2.2) as mentioned in Section 2.4, and which will be studied in detail later on in the section.

2) Tóth equation [142]

$$\Theta_A = \frac{bP}{\left(1+(bP)^c\right)^{\frac{1}{c}}} \quad 4.11$$

The Tóth equation was first introduced by Jozsef Tóth in 1962 [142]. It is an empirical expansion to the Langmuir equation, accounting for a heterogeneous surface; in particular an asymmetrical quasi-Gaussian distribution of adsorption energies, skewed to low adsorption energies. It assumes monolayer coverage of the adsorbate,  $b$  ( $\text{MPa}^{-1}$ ) is the affinity parameter as in the Langmuir equation, and  $c$  (-) accounts for the heterogeneity of the surface, either structural or chemical. When  $c$  is equal to one, the Tóth equation is reduced to the Langmuir equation, implying a homogeneous surface. The Tóth equation contains two unknown parameters and it follows Henry's Law.

3) Sips equation [141]

$$\Theta_A = \frac{(bP)^{\frac{1}{m}}}{1+(bP)^{\frac{1}{m}}} \quad 4.12$$

The Sips equation, also known as the Langmuir-Freundlich equation, is an empirical equation assuming a surface with a symmetrical quasi-Gaussian energy distribution. It was developed by Robert Sips as an extension to the Freundlich equation and at low pressures reduces to the Freundlich equation (Equation 4.13) [201].

$$\Theta_A = kP^{\frac{1}{m}} \quad 4.13$$

where  $k$  ( $\text{MPa}^{-1}$ ) and  $m$  (-) are temperature dependent parameters. The Sips equation also assumes monolayer coverage, has two unknown parameters, and does not obey Henry's Law. Parameter  $m$  relates to the heterogeneity of the system, and is usually larger than 1, so the higher the value of  $m$ , the more heterogeneous the system. When  $m$  is equal to 1, the Sips equation reduces to the Langmuir equation.

4) Generalised Freundlich equation [202]

$$\Theta_A = \left( \frac{bP}{1+bP} \right)^q \quad 4.14$$

The Generalised Freundlich equation is another empirical expansion on the Langmuir equation, introduced by Robert Sips in 1950 [202]. It assumes an exponentially decreasing surface energy distribution and monolayer coverage, it has two unknown parameters and it does not follow Henry's Law. The  $q$  (-) parameter refers to the heterogeneity of the system, and when  $q$  is unity, the Generalised Freundlich equation reduces to the Langmuir equation.

5) Jovanović-Freundlich equation [203]

$$\Theta_A = 1 - \exp\left(- (bP)^c\right) \quad 4.15$$

The Jovanović-Freundlich equation is a semi-empirical equation for single component adsorption, assuming an asymmetrical quasi-Gaussian skewed to high adsorption energies, first published by Igor Quiñones and Georges Guiochon in 1996 [203]. It reduces to the Jovanović equation (Equation 4.16) when  $c$  (-) is unity, relating to a homogeneous surface [204].

$$\Theta_A = 1 - \exp(-bP) \quad 4.16$$

The Jovanović-Freundlich equation is applicable to mobile and localised adsorption, it does not follow Henry's Law and it has two unknown parameters.

6) Dubinin-Astakhov equation [121]

$$\Theta_A = \exp\left(\frac{RT}{\alpha + \beta T}\right)^m \ln\left(\frac{P_0}{P}\right)^m \quad 4.17$$

The Dubinin-Astakhov (DA) equation is a semi-empirical equation following a pore filling mechanism, although it does not follow Henry's law. It is represented in Equation 4.17 in its modified form, extended to the supercritical region, first published in 2009 by Marc-Andre Richard *et al.* [121]. Parameter  $m$  (-) is the heterogeneity parameter in the DA equation, and if  $m$  is equal to 2 then this equation is known as the Dubinin-Radushkevich (DR) equation. The parameter  $\alpha$  ( $\text{J mol}^{-1}$ ) is the enthalpic factor, and  $\beta$  ( $\text{J mol}^{-1} \text{K}^{-1}$ ) is the entropic factor.  $P_0$  (MPa) is the vapour pressure, inapplicable to a supercritical fluid such as hydrogen above its critical point of 33 K, but despite this the DA has still been widely used for supercritical hydrogen in literature [121, 130, 205] by empirically relating the vapour pressure to the critical pressure and temperature, as observed in Equation 4.18 [206].

$$P_0 = P_C \left(\frac{T}{T_C}\right)^k \quad 4.18$$

Where  $P_C$  (MPa) is the critical pressure,  $T_C$  (K) is the critical temperature, and  $k$  (-) is a parameter determined from the fit.

7) Unilan-Q equation [207]

$$\Theta_A = \frac{RT}{Q_2 - Q_1} \ln \left( \frac{1 + A \exp\left(\frac{Q_2}{RT}\right) P}{1 + A \exp\left(\frac{Q_1}{RT}\right) P} \right) \quad 4.19$$

The Unilan-Q equation (known as the Unilan equation in literature, but expanded here to Unilan-Q to avoid confusion with the Unilan- $b$  equation below) is an empirical equation using a uniform surface energy distribution with respect to  $Q$  ( $\text{kJ mol}^{-1}$ ), the enthalpic factor. The term Unilan refers to uniform Langmuir, and was first published in 1993 by Xijun Hu and Duong D. Do [207].  $Q$  is related to the

affinity parameter  $b$  ( $\text{MPa}^{-1}$ ) by Equation 2.2, mentioned in Section 2.4. The Unilan-Q equation follows Henry's law and has three unknown parameters.

8) Unilan- $b$  equation [183]

$$\Theta_A = 1 - \frac{1}{P(b_2 - b_1)} \ln \left( \frac{1 + b_2 P}{1 + b_1 P} \right) \quad 4.20$$

The Unilan- $b$  equation is a relatively new equation derived by the author in previous studies. It has a derivation similar to that of the Unilan-Q equation, but uses a uniform surface energy distribution with respect to  $b$ , the affinity parameter. The equation assumes monolayer coverage, and only has two unknown parameters.

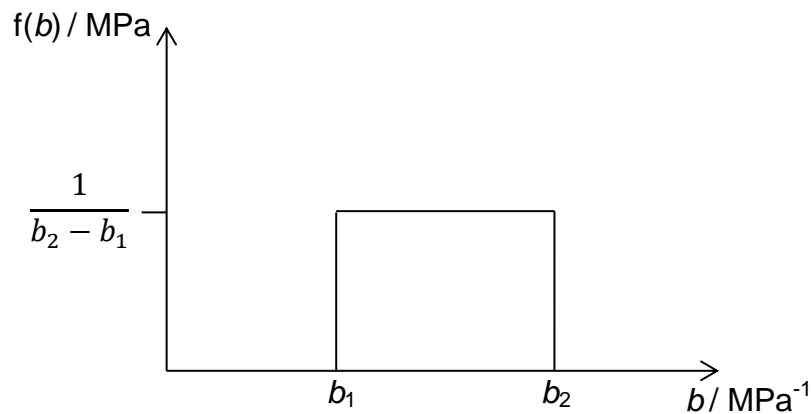


**Figure 4.9 – A continuous uniform distribution with respect to the affinity parameter,  $b$ .**

The Unilan- $b$  equation follows Henry's Law and saturation, and it reduces to the Langmuir equation when  $b_2$  ( $\text{MPa}^{-1}$ ) approaches  $b_1$  ( $\text{MPa}^{-1}$ ) (as seen in Supplementary Information C).

There are three benefits of using  $b$  for the energy distribution instead of  $Q$ . Firstly, it is easier to comprehend the interactions between the adsorbate and adsorbent than it is to comprehend the enthalpy of a system. Secondly,  $b$  is considered as a single parameter, whereas it has been observed that  $A$  and  $Q$  (in Equation 4.19) are correlated, known as the 'compensation effect' [208], and  $b$  takes both  $A$  and  $Q$  into account. Thirdly, the Unilan- $b$  equation is a lot simpler and has fewer parameters than the Unilan- $Q$  equation. The Unilan- $b$  equation was derived and tested in a scientific paper which was published in the journal Adsorption [183].

The main differences in the equations detailed above are highlighted in Table 4.1.

**Table 4.1 – A summary of the isotherm equations, the surface energy distribution, the type of adsorbent-adsorbate interaction, and the number (no.) of parameters in each equation.**

<b>Name</b>	<b>Surface energy distribution</b>	<b>Interaction</b>	<b>No. of parameters</b>
Langmuir	Homogeneous	Monolayer	1
Tóth	Asymmetrical quasi-Gaussian skewed to low adsorption energies	Monolayer	2
Sips	Symmetrical quasi-Gaussian	Monolayer	2
Generalised Freundlich	Exponentially decreasing	Monolayer	2
Jovanović-Freundlich	Asymmetrical quasi-Gaussian skewed to high adsorption energies	Monolayer, considers vertical interactions bulk/surface	2
Dubinin-Astakhov	Weibull distribution	Pore filling mechanism	4
Unilan-Q	Uniform distribution with respect to $Q$	Monolayer	3
Unilan- $b$	Uniform distribution with respect to $b$	Monolayer	2

#### **4.2.1.3 Individual fits**

The initial stage of the study was to fit each isotherm equation within the DV model to every different temperature isotherm from each material separately. The 89,

102, 120 and 150 K isotherms of the TE7 carbon beads and the Tóth equation have been selected here as an example to represent the methodology and results. The results established using the other materials and equations are all very similar, and do not provide any further information. The other temperature isotherms for the TE7 carbon beads were not chosen for use in this study due to the reasons as mentioned in Section 0. Figure 4.10 displays the individual fits for the Tóth equation to each separate isotherm of the TE7 carbon beads. Included in the plots are the regular residuals, which are the wt% hydrogen uptake from the actual data, minus the predicted wt% hydrogen uptake from the fit for each data point. These differ from standardised residuals, which convert each regular residual by dividing by the standard deviation of all the residuals, and allows for outliers to be found as well as patterns in the data [209].

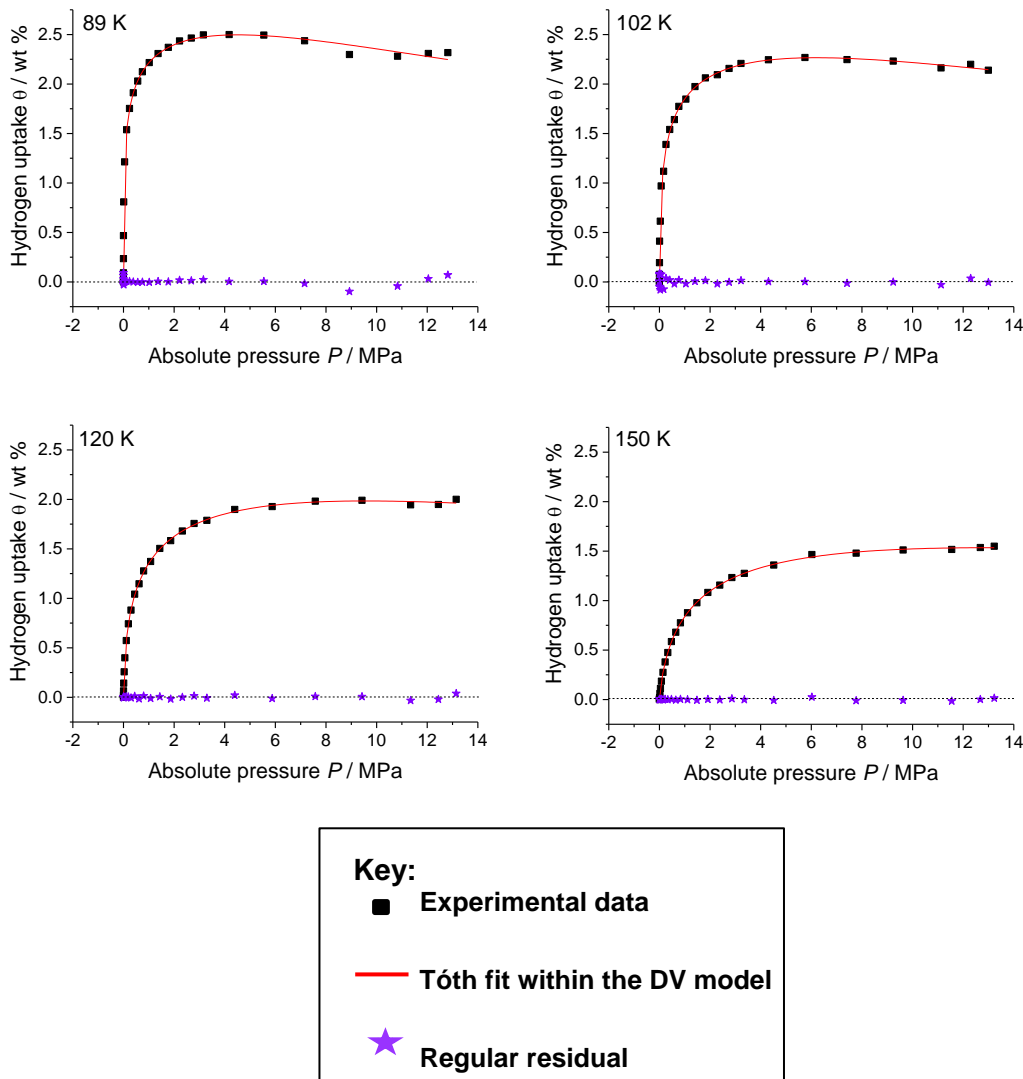
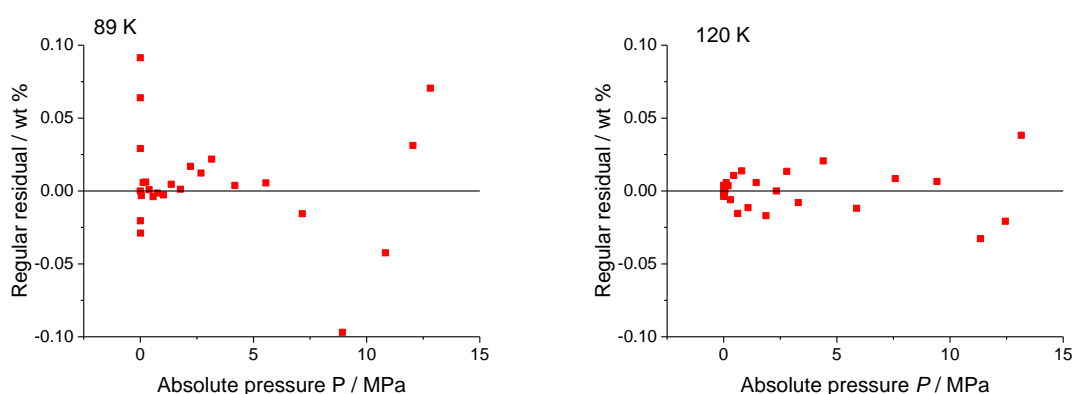


Figure 4.10 – Individual fits to the experimental TE7 carbon bead isotherms (black squares) at different temperatures using the DV model with the Tóth isotherm equation (red line). The dotted black line is at zero wt% hydrogen uptake, to highlight the trends in the regular residuals (purple stars).

There are a few points to note from Figure 4.10. The model appears to fit well to all of the experimental isotherms, apart from the unexpected rise in uptake observed in some of the isotherms at high pressures, for example above 10 MPa on the 89 K isotherm. This apparent rise in uptake is not thought to be a real phenomenon of adsorption, but is most likely due to the fact that in the volumetric gas sorption apparatus (detailed in the methodology), at very high pressures the system contains a lot more hydrogen than at low pressures. As hydrogen conducts heat very well, it is significantly more difficult for the machine to maintain a constant temperature, and so there are more fluctuations within the temperature, as observed by the sample temperature recorded on the apparatus.

The residuals, as observed in Figure 4.10, are a method of looking at the bias of a fit. If there is a random distribution of residuals both above and below zero, then the fit is not biased, whereas a group of adjacent residuals either above or below zero suggests bias in the fit. The Tóth fits vary in bias between temperatures, as seen in Figure 4.11, and it can be observed that at 89 K the fit indicates this type of bias, but at 120 K it does not. This is very similar for the trends observed using the other isotherm equations, examples of which can be found in Supplementary Information D, and is more likely to be due to the shapes of the isotherms as opposed to the isotherm equation chosen. The residuals observed for the other materials also appear to be similar between isotherm equations, emphasising the point that they depend on the shape of the isotherms more than the model.



**Figure 4.11 – Regular residuals with pressure for the DV model fit using the Tóth isotherm equation on the 89 K and 120 K experimental hydrogen isotherms from the TE7 carbon beads.**

The other method of bias that can be observed from the residuals is called heteroscedasticity, and is a measure of increasing or decreasing scatter in residuals with the independent variable. The 120 K residuals could indicate this type of bias (Figure 4.11), but it is most likely due to the unexpected apparent rise in the experimental data at high pressures as previously mentioned.

#### **4.2.1.4 Global fits**

Following the initial fits, studies on the pore volume and adsorbate density dependence on temperature from the individual fits were completed in order to be able to perform global fits on the isotherms, as these parameters are independent of the isotherm equation chosen. Global fits were conducted by fitting the DV model to all of the isotherms of one material at the same time, keeping certain

parameters constant for each temperature. In this way, only one RSMR value is produced for each isotherm equation used within the DV model fit to each material, so that an easy, direct comparison can be made.

Graphs were plotted for the values of adsorbate density and pore volume that were output from the individual fits at different temperatures, versus the temperature, such as those observed in Figure 4.12.

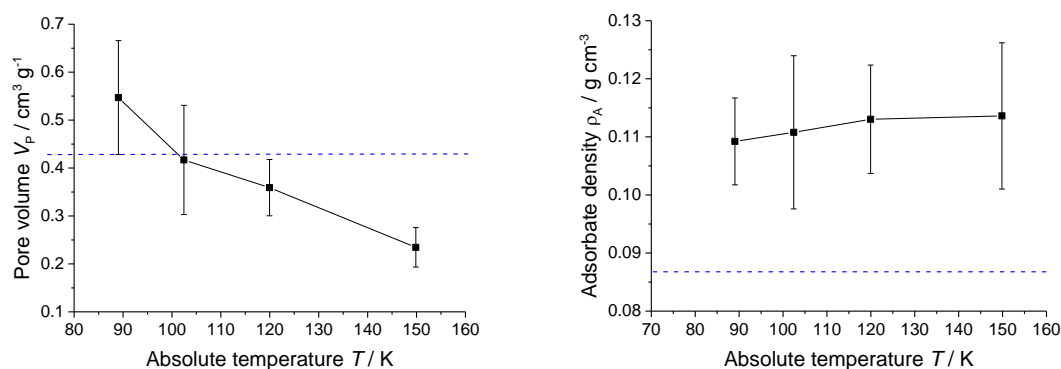


**Figure 4.12 - The dependence of (a) the pore volume and (b) the adsorbate density on temperature, found by fitting the DV model including the Tóth isotherm equation on the experimental isotherms of the TE7 carbon beads. Lines linking the data points are just to guide the eye. The dotted line at  $0.43 \text{ cm}^3 \text{g}^{-1}$  in (a) represents the micropore volume of the TE7 carbon beads determined experimentally using the Dubinin-Radushkevich method. The dotted line at  $0.087 \text{ g cm}^{-3}$  in (b) represents the density of solid hydrogen at 0 Pa and 4 K. The error bars are calculated by standard error.**

There are a few things to note about the graphs in Figure 4.12. The pore volume appears to result in a fairly linear negative trend with temperature. However, realistically for a rigid material like the TE7 beads, there should be no change in pore volume with temperature, and so it is unclear as to whether this trend is real, or just an artefact of the analysis. Therefore, it was decided to set the pore volume as constant with temperature, although this is examined further later on in the section.

The adsorbate density (Figure 4.12 (b)) is fairly constant with temperature, although with a slight positive trend. For simplicity, the adsorbate density is also going to be set as a constant value with temperature at this stage, but will also be examined further on in the section.

There is something else interesting to note about Figure 4.12 (b). The dotted line at  $0.087 \text{ g cm}^{-3}$  is the solid hydrogen density at 0 Pa and 4 K [210], indicating that

the hydrogen within the pores has a density commensurate to that of solid hydrogen. If this is not an artefact of the data, then the result is fascinating, and this concept will be discussed further in Section 4.3.

Following the decision to set the pore volume and adsorbate density as constant with temperature, a global fit was completed on the isotherms of the TE7 carbon beads. This was achieved by keeping the pore volume and adsorbate density constant with temperature, but allowing the parameters within the Tóth equation,  $b$  and  $c$ , to vary between the isotherms.

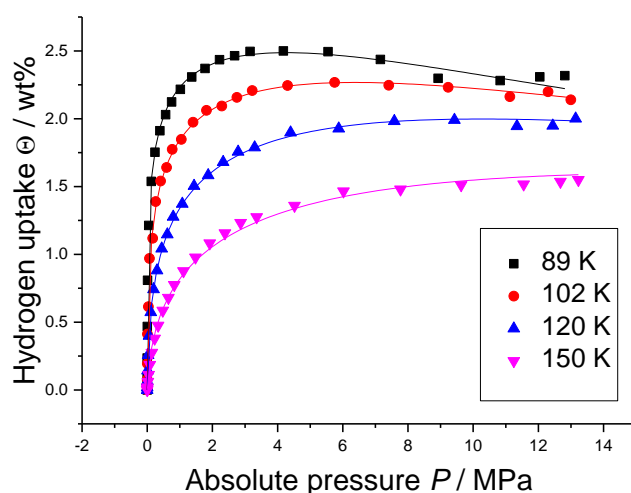


**Figure 4.13 - Global fit of the DV model including the Tóth isotherm equation to all of the isotherms from the TE7 carbon beads. The corresponding coloured line is the Tóth fit to the experimental data points.**

It can be observed from Figure 4.13 that the model still appears to fit the isotherms well, even after restricting the pore volume and adsorbate density to remain constant with temperature. As mentioned previously, this was completed for all of the isotherm equations and materials, examples of which can be found in Supplementary Information E.

#### **4.2.1.5 Comparison of the quality of the global fits**

A comparison between the global fits of all of the equations on all of the materials was then made. As mentioned in the methodology, there are many different ways of assessing the quality of fit. The method that was chosen to compare the results of this study was the RMSR, due to the fact that it has units of wt%, and so could be put into context with respect to the overall isotherms. However, because in this

case it was necessary to calculate the quality of fit for multiple isotherms at the same time, the equation was adjusted slightly to:

$$RMSR = \sqrt{\text{reduced } \chi^2} = \sqrt{\frac{\sum_{j=1}^m RSS}{DOF}} = \sqrt{\frac{1}{n-p} \sum_{j=1}^m \sum_{i=1}^n (y_i - \hat{y}_i)^2} \quad 4.21$$

where  $j$  (-) is the particular isotherm,  $m$  (-) is the number of isotherms, and  $n$  (-) in this case includes all of the data points.

Using this equation, the following graphs were produced.

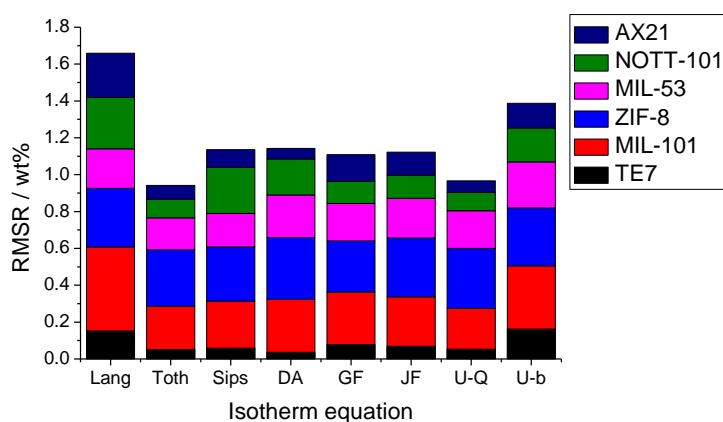


**Figure 4.14 - The cumulative RMSR values for global fits of each isotherm equation within the DV model to each material. Lang refers to the Langmuir equation, DA to the Dubinin-Astakov, GF to the Generalised-Freundlich, JF to the Jovanović-Freundlich, U-Q to the Unilan-Q and U-b to the Unilan-b.**

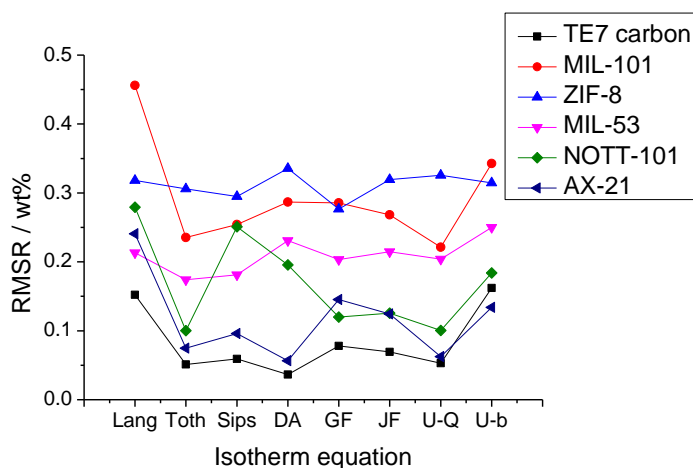


**Figure 4.15 - The RMSR values for global fits of each isotherm equation within the DV model to each material. Lang refers to the Langmuir equation, DA to the Dubinin-Astakov, GF to the Generalised-Freundlich, JF to the Jovanović-Freundlich, U-Q to the Unilan-Q and U-b to the Unilan-b.**

Both Figure 4.14 and Figure 4.15 show the same information, but plotted differently in order to emphasise different trends. Figure 4.14 shows the cumulative RMSR from the materials, for each equation. It shows that overall, utilising the Langmuir or the Unilan-*b* equations within the DV model exhibit the worst fits to the data (highest RMSR values), using the Tóth or the Unilan-Q equations result in the best fits to the data, with the use of the other four equations demonstrating relatively similar quality of fits.

However, Figure 4.15 shows that even though the Tóth has the best fit overall to the data, it is not the best equation to use for each individual material. For example, using the Sips equation and the Generalized Freundlich equation within the DV model both result in better fits to the ZIF-8 isotherms than using the Tóth equation. Figure 4.15 also shows that generally, all of the equations fit better to the isotherms of the carbon materials (TE7 and AX-21) than the MOFs, and worst of all to the ZIF. This result could be skewed as the RMSR does not take into account the capacity of the materials, and higher capacities could result in higher RMSR values [211], which would not affect the trends within each material, but could in a comparison between materials. Another point to note from Figure 4.15 is that some equations show much higher or lower RMSRs for certain materials than would be expected from observing general trends. For example, the Sips and the Dubinin-Astakhov equations show much higher RMSRs for NOTT-101 in comparison to the other equations than they do for other materials.

Overall, this shows that the comparison between materials when using different isotherm equations within a model is not accurate, although the Tóth equation appears to be the best isotherm equation to use overall, as it fits well to the isotherms from all materials and only has two parameters. Therefore, for all following studies, the Tóth equation is used to represent the fractional filling.

#### **4.2.2 Pore volume, $V_p$ , dependence on pressure and temperature**

The subsequent parameter to be studied was the pore volume. The pore volume is a particularly important quantity as it is required when calculating the total amount of hydrogen in the system, and so is vital to estimate accurately. As mentioned in the methodology, certain adsorbent materials are known to be flexible, thus the pore volume can change with either pressure, temperature, or inclusion of a guest

molecule within the pore. It has even been discovered that materials that were thought to be rigid do change structure slightly at very high pressures, such as zeolites [212]. Therefore, to see if it could be determined how the pores flex with pressure and temperature, and also to make the DV model accessible to all adsorbent materials, pore volume dependence on pressure and temperature was examined.

This research was conducted by introducing different pore volume dependencies into the DV model and observing the quality of fit for the six different adsorbent materials, as well as the values of the parameters from the fits and their trends with temperature.

Literature studies highlight how flexible materials are thought to breathe with pressure and temperature, particularly using MIL-53(Al) (referred to in this section as MIL-53). An example of MIL-53 breathing with temperature can be found in literature by Liu *et al.* [164] who observe structural hysteresis with temperature. An example of MIL-53 breathing in the presence of guest molecules can be observed in Figure 4.16, but with xenon, methane and carbon dioxide adsorption [213].

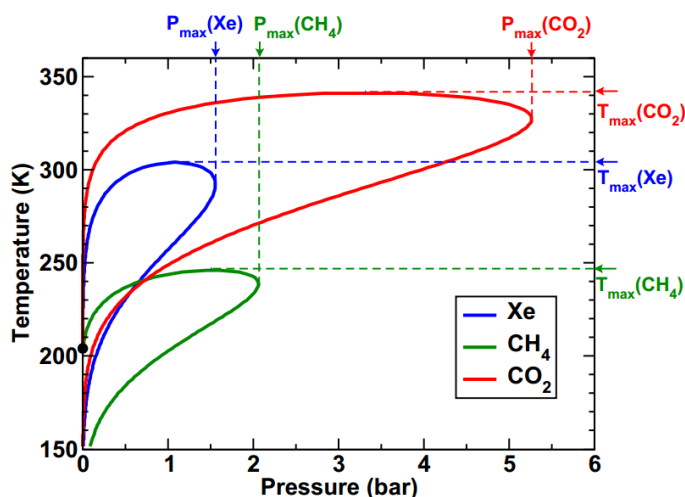


**Figure 4.16 - A diagram determining the pressures and temperatures at which the pores of MIL-53 are in narrow form or large form. Everything within the bubbles represents the conditions within which the narrow pores exist, and everything outside are the conditions required for the large pores. This was determined by an osmotic thermodynamic model as well as a series of adsorption experiments [213].**

If a similar trend was observed for the pores of MIL-53 with hydrogen adsorption then the pressure and temperature dependencies of pore volume would be a

uniform distribution (Figure 4.17), where  $T_1$  and  $T_2$  depend on pressure and  $P_1$  and  $P_2$  depend on temperature.

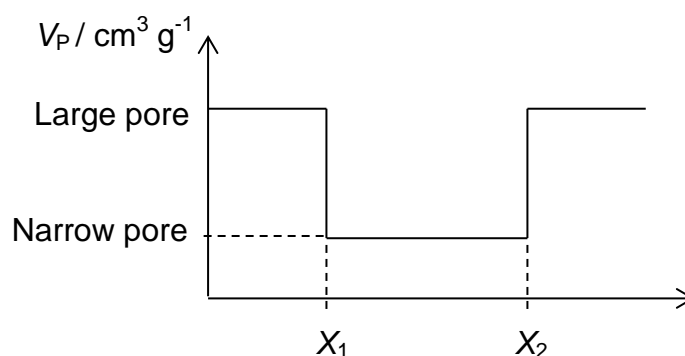


**Figure 4.17 - A representation of the potential uniform distribution dependence of pore volume ( $V_p$ ) on pressure and temperature, where  $X$  could represent either pressure or temperature.**

At the time of writing this thesis, there had been no suggested method for how, or if, MIL-53 breathes with hydrogen adsorption in literature. The breathing behaviour with hydrogen adsorption could differ to that from other adsorptives due to the very weak interaction of hydrogen with the adsorbent, and is even thought to potentially not induce MIL-53 to breathe at all [214].

However, the majority of studies still believe that through the process of hydrogen adsorption some change in structure of the pores is observed, due to the anomalies seen in the isotherms at low pressures, as observed in the isotherms measured in Figure 4.18, and which has also been observed elsewhere in literature [164]. However, the desorption isotherm measured for MIL-53 using the gas sorption apparatus highlighted in Section 3.2.4 was not able to go to a low enough pressure to show the same hysteresis as observed in literature [164].

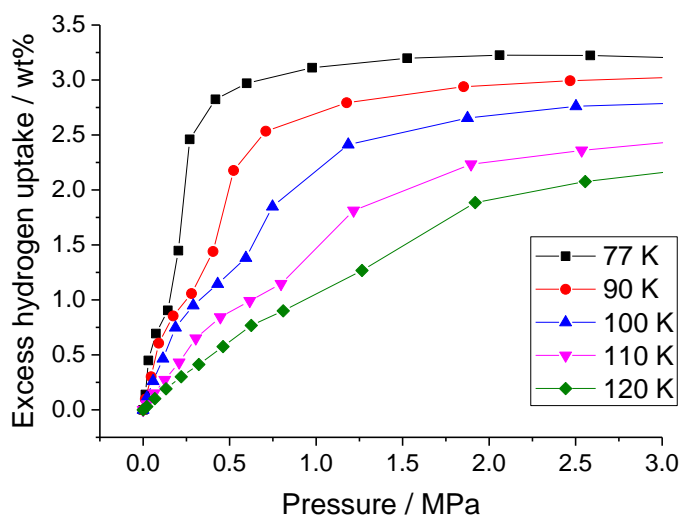


**Figure 4.18 - The low temperature region of the MIL-53 hydrogen isotherms measured on the HTP-1, indicating potential breathing of the material with hydrogen adsorption by the kinks observed in the isotherms.**

The most successful experimental method of observing this phenomenon is *via* x-ray diffraction (XRD) at a variety of temperatures and pressures. Using this technique, it can be observed at what conditions the large pore XRD powder patterns and the narrow pore XRD powder patterns are found, as they differ for both as observed in Figure 4.19.

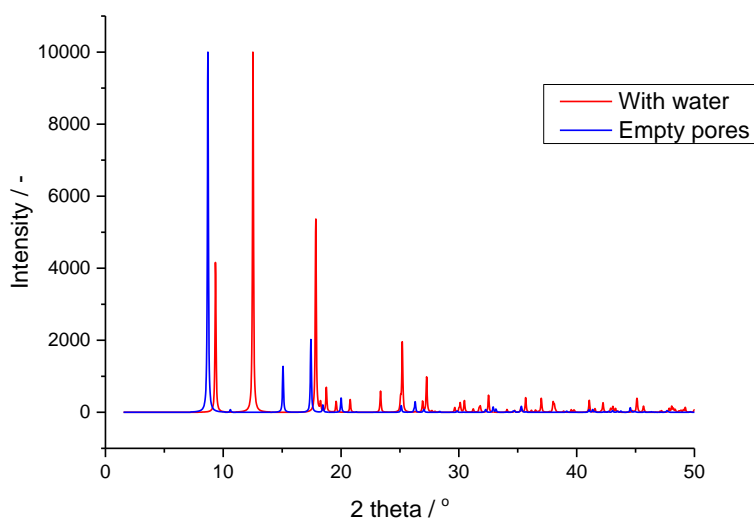


**Figure 4.19 - The different XRD powder patterns for MIL-53(Al) with large pores (red line, containing water) and narrow pores (blue line, empty), as measured by Dr. Dongmei Jiang at the University of Bath.**

Therefore, beam time on the European Synchrotron and Radiation Facility (ESRF) in Grenoble (details of which can be found in the methodology) was applied for by Dr. Valeska Ting at the University of Bath and granted, in order to study the XRD

patterns of adsorbents with hydrogen adsorption at various pressures and temperatures. The use of this machine was necessary due to the high pressure and cryogenic temperatures required which are not accessible on a routine laboratory XRD.

Two different materials were chosen to be tested at the ESRF, MIL-53, a known flexible MOF, and MIL-101, a rigid MOF (detailed in Section 3.1).

The temperature dependence of MIL-101 was tested first at 0 MPa and 80, 90, 100, 120, 150, 200 and 300 K, following degas of the sample at 293 K under vacuum for 5 hours. XRD patterns were conducted from 0 - 60 °2θ at a rate of 2° min<sup>-1</sup> and each repeated three times. No structural change was observed at these conditions, and so more readings were done at 10 MPa and 80, 100 and 300 K in order to get a broad range of hydrogen pressures and temperatures. Again, no structural change was observed, indicating a pore volume independent of both pressure and temperature with hydrogen adsorption (Figure 4.20).

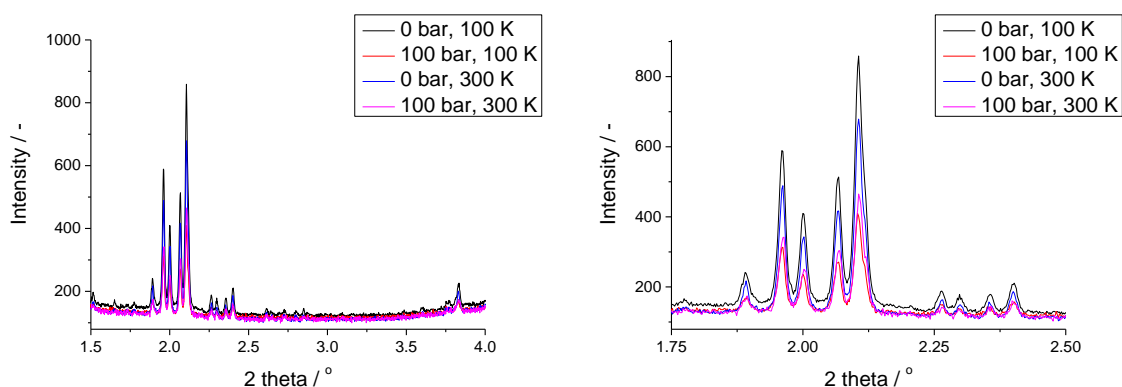


**Figure 4.20 – The XRD patterns of MIL-101 at a variety of hydrogen pressures and temperatures.**

The MIL-53 sample was then degassed at 423 K for 8 hours before a range of quick scans were conducted at a variety of temperatures and pressures in order to try to gauge the conditions at which the material might flex. These were conducted at 0 to 20 °2θ at a rate of 2° min<sup>-1</sup> and not repeated. The results of the scans were fairly inconclusive, only showing exceptionally small shifts of approximately 0.02 ° 2θ in some peaks, the largest shift of which can be observed in Figure 4.21. However, Figure 4.21 does show that the peak shift appears to be dependent on temperature, with the 80 K scans showing a slight difference to the 173 and 273 K

scans. Because the shift was so small, longer scans were conducted at the temperatures and pressures shown in Figure 4.22.

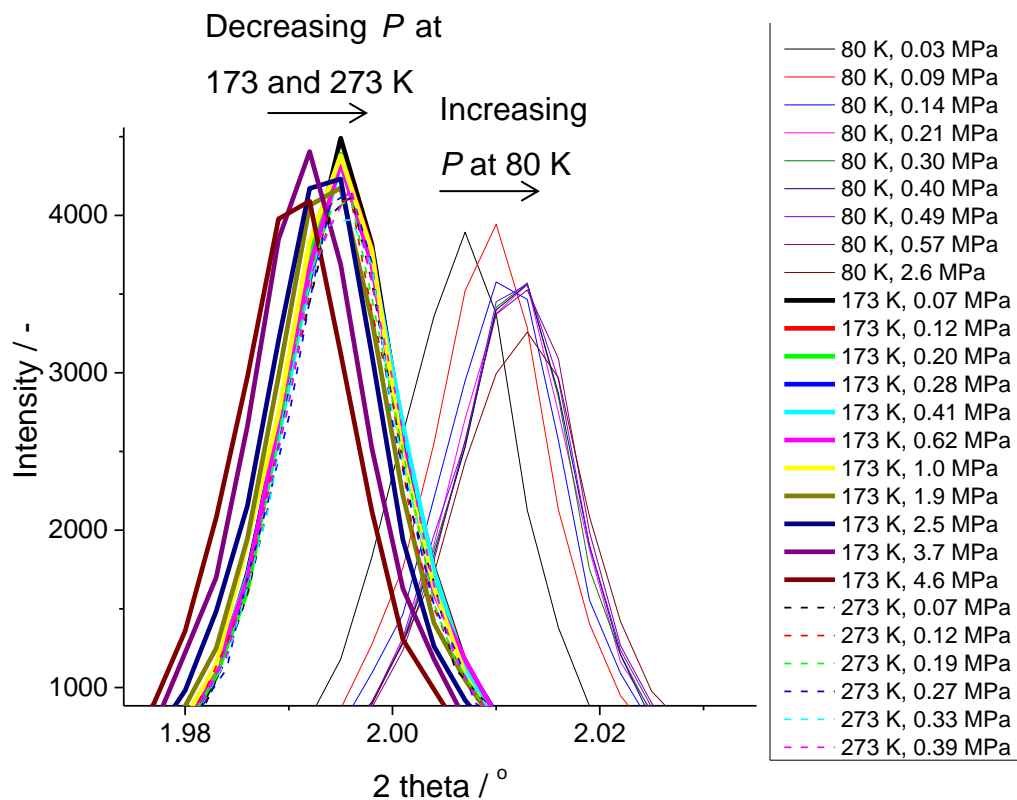


Figure 4.21 – A zoomed in region of the XRD quick scan patterns of MIL-53 showing the largest peak shift.

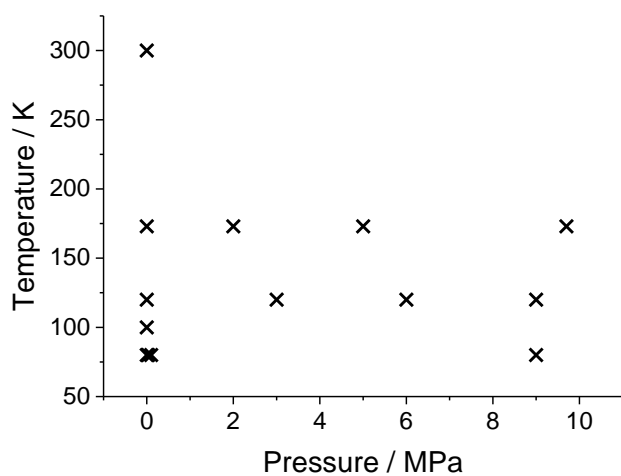
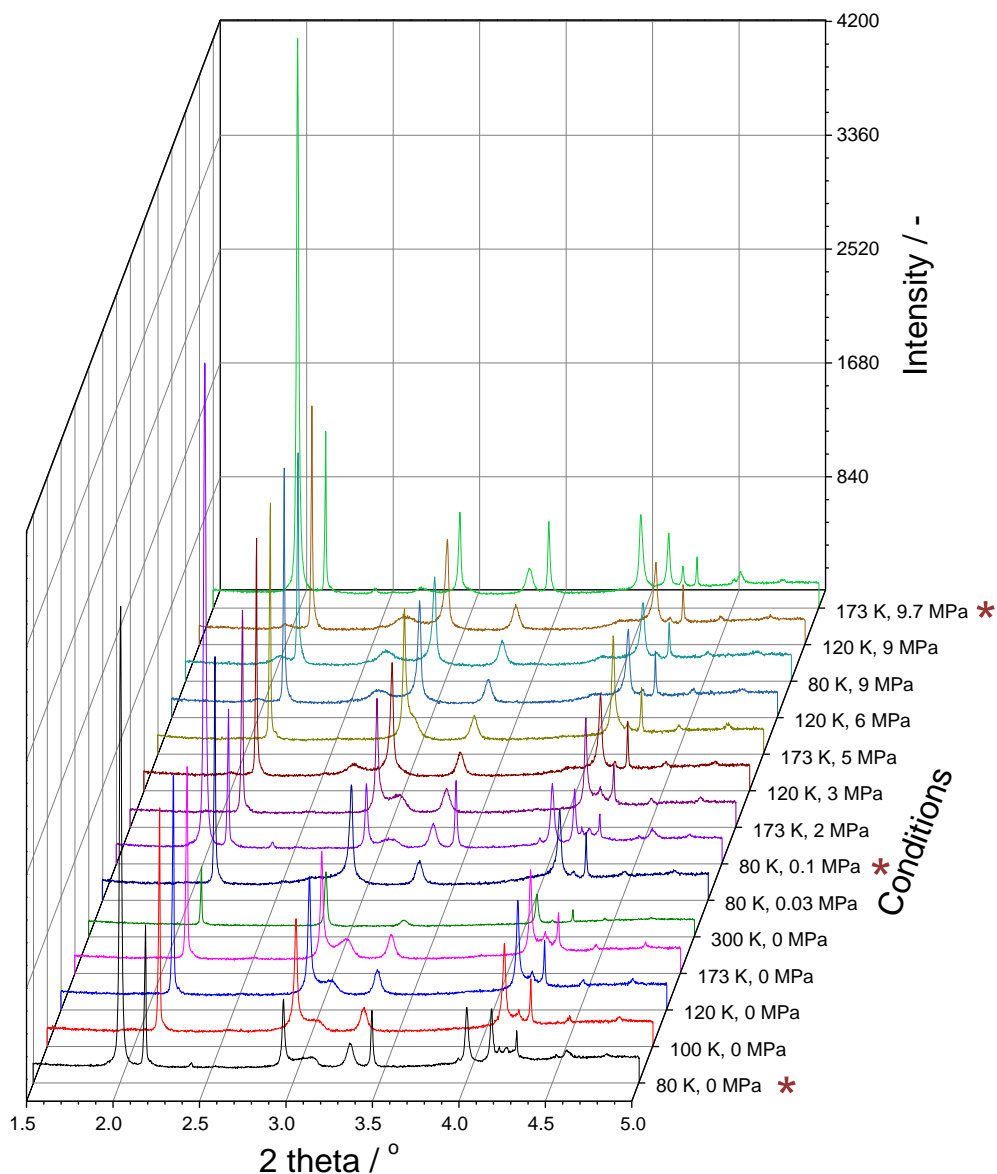


Figure 4.22 – The temperatures and pressures used for the long scan XRD experiments on MIL-53.

The long scans showed two different XRD powder patterns over the range of temperatures and pressures chosen, as observed in Figure 4.19, potentially indicating the breathing of MIL-53. However, further investigation into the XRD powder patterns showed no real trend with either pressure or temperature, indicating that there might have been a contaminant, such as water, in either the hydrogen used, or in the system itself. This theory was validated when it was discovered that all of the XRD patterns taken after the hydrogen bottle was changed showed MIL-53 in what appears to be a combination of the narrow pore and the large pore phase, whereas all of the XRD powder patterns before showed MIL-53 in just the large pore phase. On returning to the University of Bath, the sample was degassed once more at 423 K for 4 hours and an atmospheric XRD scan showed the pattern of MIL-53 with narrow pores, showing that the error was not in the material itself.



**Figure 4.23 – The XRD powder patterns from the MIL-53 long scans at the ESRF. The brown stars highlight the conditions within which different XRD patterns are observed to the rest, and also show the patterns that were made following the change in the hydrogen cylinder.**

The peaks cannot be directly compared to those measured at the University of Bath without a conversion of the  $2\theta$  scale, due to the difference in the wavelengths of the X-ray beams. However by simply looking at the corresponding peaks in both Figure 4.19 and Figure 4.23, it can be observed that only the powder patterns taken at 80 K and 0 MPa, 80 K and 1 MPa, and 173 K and 9.7 MPa (highlighted with brown asterisks on Figure 4.23) show the powder pattern of MIL-53 with a combination of large and narrow pores, the patterns taken after the hydrogen tank was changed.

Unfortunately, due to the unreliability of the results, it was not possible to determine experimentally how the pore volume changed with temperature and pressure.

#### 4.2.2.1 Pore volume dependence on pressure

Due to the lack of experimental evidence for how the pore volume varies with pressure and temperature upon hydrogen adsorption, it was decided to choose simple pore volume dependencies on pressure to see how they affected the quality of the fits, and to see if the results could be used to determine how the pore volume changed with pressure and temperature. For the simple functions, a linear, rational and power type function were chosen, but a Langmuir type function was also chosen which could comprehensively be a realistic function for the pore volume dependence on pressure. Due to the reasons mentioned previously in the section, functions with small numbers of parameters were decided upon. The pore volume dependencies on pressure were chosen as listed in Table 4.2.

**Table 4.2 - The different functions chosen to represent the pore volume, and the number of parameters in each. The equation numbers are given in brackets after the equations.**

Type of dependence	Equation	Number of parameters
Linear	$V_P = V_P^0 (1 + \alpha P) \quad (4.22)$	2
Rational	$V_P = V_P^0 \frac{1 + \alpha P}{1 + \beta P} \quad (4.23)$	3
Power	$V_P = V_P^0 (1 + P^\alpha) \quad (4.24)$	2
Langmuir type	$V_P = V_P^0 + (V_P^{\max} - V_P^0) \left( \frac{\beta P}{1 + \beta P} \right) \quad (4.25)$	3

They were each input into the DV model, and the RMSR was observed from global fits on the isotherms of the TE7 carbon beads (the reference material), and MIL-53, due to its flexibility. The adsorbate density was assumed constant, the Tóth

isotherm equation was used for the fractional filling, and all other parameters were allowed to vary with temperature. The fits can be found in Supplementary Information F, and Table 4.3 shows the results of this study.

**Table 4.3 - RMSR values using different pore volume ( $V_p$ ) dependencies of pressure on the TE7 carbon beads and MIL-53 to 3 decimal places (dp).**

$V_p$ function	RMSR values / wt%	
	TE7 carbon beads	MIL-53
Linear	0.030	0.095
Rational	0.030	0.090
Power	0.030	0.091
Langmuir type	0.039	0.147
Constant with pressure and temperature	0.036	0.174

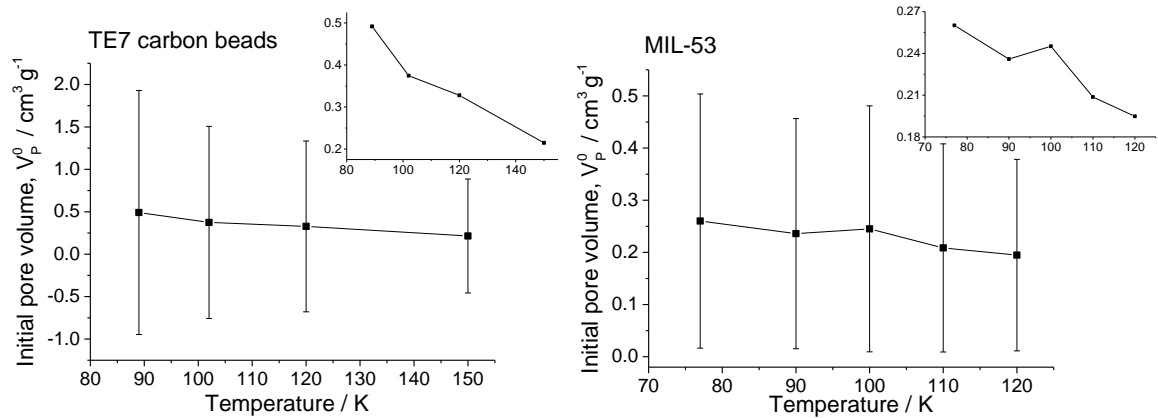
Table 4.3 highlights that the linear, rational and power functions of pore volume with pressure improve the RMSR of the global fits compared to a constant pore volume for both the TE7 carbon beads and MIL-53, whereas the Langmuir type function only improves it slightly for the MIL-53 and not at all for the TE7 carbon beads. These improvements would be expected due to the increase in the number of parameters in the overall DV model. Considering that the difference in the RMSR values for the linear, rational and power functions of pore volume with pressure are the same to 3 dp for the TE7 carbon beads, and very similar for MIL-53, it was decided that the temperature dependence of the parameters in the linear and the power functions would be observed in detail, as both of these functions only have two parameters whereas the rational function has three. The temperature dependence of the parameters was selected to be studied in order to ascertain if realistic values were found from the fits, and consequently to determine how realistic the linear and power pore volume dependencies on pressure are.

#### **4.2.2.1.1 Linear pore volume dependence on pressure**

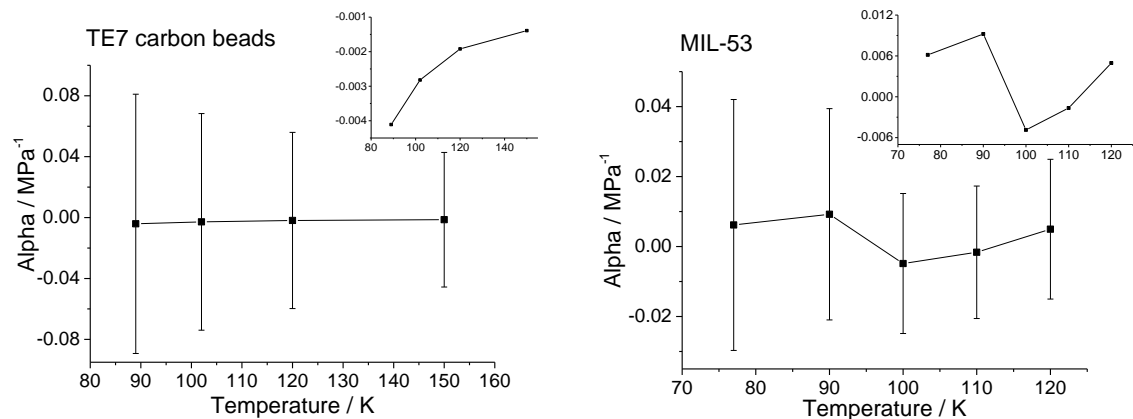
For the linear dependence of the pore volume on pressure, the two unknown parameters are the initial pore volume,  $V_p^0$ , and alpha,  $\alpha$ , which can be thought of

as the incremental change in pore volume with pressure, over the initial pore volume, as observed in Equation 4.26.

$$\alpha = \frac{1}{V_p^0} \frac{dV_p}{dP} \quad 4.26$$



**Figure 4.24 - The initial pore volume dependencies on temperature for the TE7 carbon beads and MIL-53, assuming a linear-type dependence on pore volume with pressure. The y-error from the fitting is shown for each point, and the insets show the same data without the y-error. Lines joining the points are to guide the eye.**



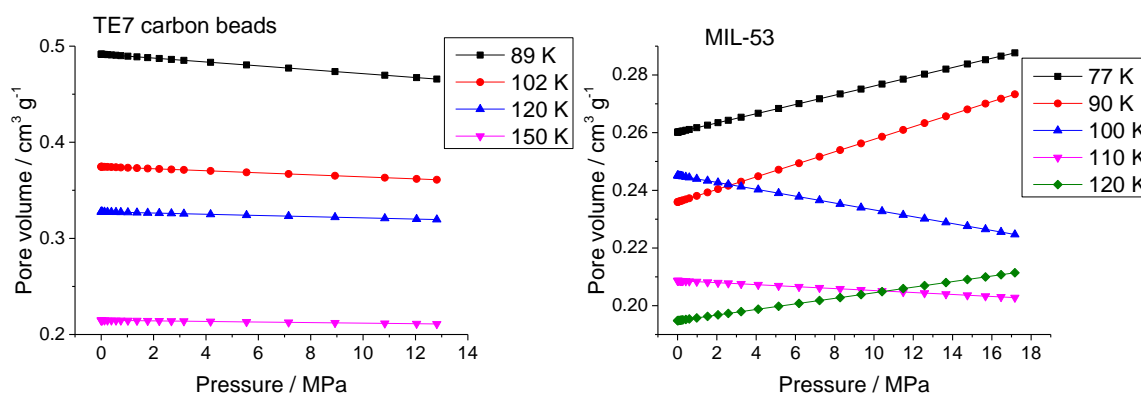
**Figure 4.25 - The dependencies of alpha on temperature for the TE7 carbon beads and MIL-53, assuming a linear-type dependence on pore volume with pressure. The y-error from the fitting is shown for each point, and the insets show the same data without the y-error. Lines joining the points are to guide the eye.**

Figure 4.24 and Figure 4.25 show that the error in the data from the fitting is very large for both the initial pore volume and alpha, indicating that the trends observed may not be reliable. From Figure 4.24, if the error is ignored it can be observed that the TE7 carbon beads show an initial pore volume decrease of nearly 0.3 cm<sup>3</sup> g<sup>-1</sup> from 89 K to 150 K, whereas MIL-53 only shows an initial pore volume decrease of approximately 0.07 cm<sup>3</sup> g<sup>-1</sup> from 77 K to 120 K. A small change may

be expected for the initial pore volume of MIL-53 with temperature as it is a flexible material, however no noticeable change would be expected from the TE7 carbon beads, indicating that this result may just be an artefact of the fitting and not a representation of the actual initial pore volume dependence on temperature.

Ignoring the error bars in Figure 4.25, it can be observed that there is an upward trend in alpha with temperature for the TE7 carbon beads, although all the alpha values are negative, implying that the pore volume decreases with pressure at all temperatures, but at a less rapid rate the higher the temperature. For MIL-53, there is no obvious trend in alpha with temperature, although it can be observed from Figure 4.25 that at 77 K, 90 K and 120 K the pore volume increases with pressure whereas at 100 K and 110 K the pore volume decreases with pressure. This is a very unlikely scenario, suggesting even more that a linear dependence of pore volume with pressure is not accurate.

When the values for the initial pore volume and alpha are both considered at each temperature, the predicted linear pore volume trends with pressure can be observed using Equation 4.22 (Figure 4.26).



**Figure 4.26 – The predicted linear pore volume dependence on pressure using the values provided from the fitting for the TE7 carbon beads and MIL-53.**

Realistically, the initial pore volume for the TE7 carbon beads would be expected to be constant at around  $0.43 \text{ cm}^3 \text{ g}^{-1}$  (as measured experimentally), and alpha would be expected to be zero. The initial pore volume for MIL-53 might be expected to vary slightly with temperature but be approximately  $0.3 \text{ cm}^3 \text{ g}^{-1}$ , and alpha would be expected to be either positive or negative at all temperatures, not a combination of both. The value of  $0.3 \text{ cm}^3 \text{ g}^{-1}$  can only be considered as a rough

guideline as this is the experimentally measured value of narrow pore MIL-53, whereas that of the large pore would be greater. Figure 4.26 shows the range of pore volumes as calculated for the TE7 carbon beads to straddle the expected value, but to cover an unrealistically large range of pore volumes. Figure 4.26 also shows a very sporadic and improbable linear pore volume relationship for MIL-53.

Even though the RMSR value was improved with the inclusion of a linear pore volume dependence on pressure, the unrealistic parameter values in conjunction with the large error bars observed for each parameter indicates that the RMSR value was only improved due to the increase in the number of parameters, and not by representing a real physical phenomenon within adsorption. Therefore, a linear pore volume dependence on pressure was not included within the DV model.

#### 4.2.2.1.2 Power pore volume dependence on pressure

For the power dependence of the pore volume on pressure, the two unknown parameters are the initial pore volume,  $V_P^0$ , and alpha,  $\alpha$ , which is a complex value that cannot be considered as representing a comprehensible real phenomenon such as the alpha in the linear scenario.

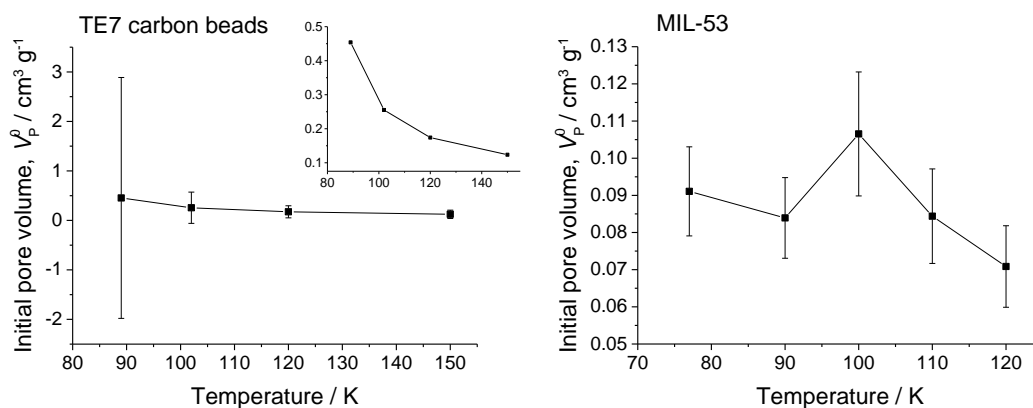


**Figure 4.27 - The initial pore volume dependencies on temperature for the TE7 carbon beads and MIL-53, assuming a power-type dependence on pore volume with pressure. The y-error from the fitting is shown for each point, and the inset shows the same data without the y-error.**

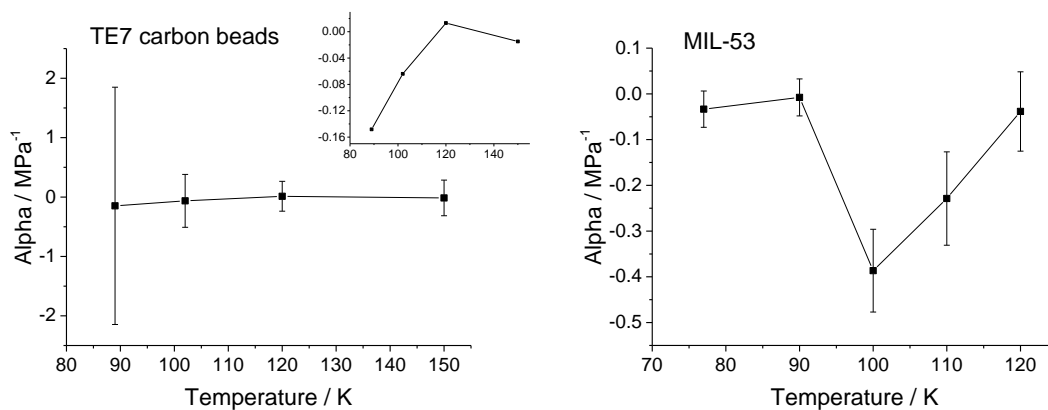


**Figure 4.28 - The alpha dependencies on temperature for the TE7 carbon beads and MIL-53, assuming a power-type dependence on pore volume with pressure. The y-error from the fitting is shown for each point, and the inset shows the same data without the y-error.**

Figure 4.27 and Figure 4.28 generally show smaller error bars than when a linear dependence of pore volume on pressure was assumed. From Figure 4.27, if the error is ignored then it can be observed that the TE7 carbon beads again show an initial pore volume decrease of approximately  $0.3 \text{ cm}^3 \text{ g}^{-1}$  from 89 K to 150 K, although MIL-53 shows a sporadic trend in initial pore volume with temperature, within the range of  $0.07$  to  $0.11 \text{ cm}^3 \text{ g}^{-1}$ , nearly a tenth of the range of values observed for the TE7 carbon beads. Again, this differs from what would be expected to happen; no change in the initial pore volume for the TE7 carbon beads, but potentially a slight change for MIL-53. Yet again, this might indicate that the results may just be an artefact of the fitting and not a good representation of the actual initial pore volumes.

Ignoring the error bars in Figure 4.28, it can be observed that there is a general upward trend in alpha with temperature for the TE7 carbon beads, although it drops again at 150 K. Three of the values for alpha are also negative, with one positive value, which appears to be a very unlikely situation as the values of alpha should have the same sign for each temperature, or else different functions of pore volume with pressure would be suggested for different temperatures. For MIL-53 there is no trend in alpha with temperature, and a combination of positive and negative values. Again, this is very unlikely to be realistic, suggesting even more so that a power dependence of pore volume with pressure is not representative of the actual scenario.

When the values for the initial pore volume and alpha are both considered at each temperature, the predicted power pore volume trends with pressure can be observed using Equation 4.24 (Figure 4.29).

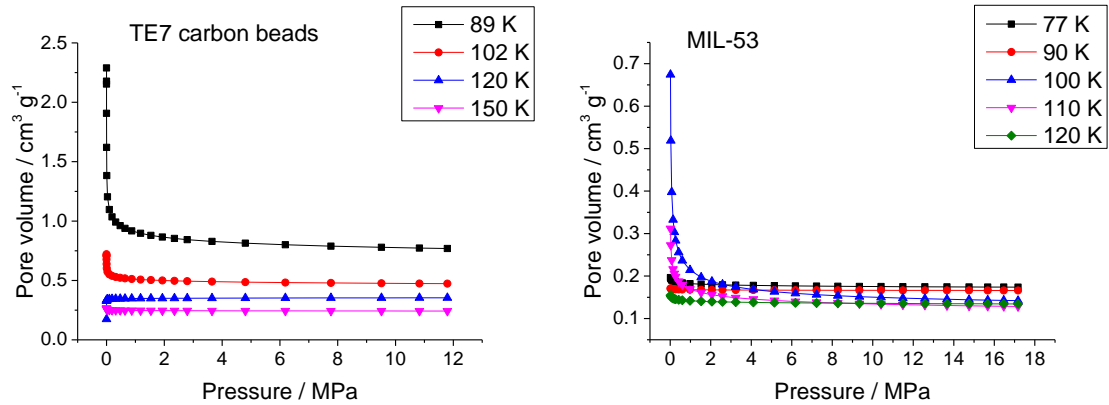


**Figure 4.29 - The predicted power pore volume dependence on pressure from the values provided from the fitting for the TE7 carbon beads and MIL-53.**

As mentioned previously, the initial pore volume for the TE7 carbon beads would be expected to be constant at around  $0.43 \text{ cm}^3 \text{ g}^{-1}$ , and alpha would be expected to be zero. The initial pore volume for MIL-53 might be expected to vary slightly with temperature but be approximately  $0.3 \text{ cm}^3 \text{ g}^{-1}$  (with the same caution required for large pore versus narrow pore values), but the predicted values of alpha are unknown. Figure 4.29 shows that the pore volumes calculated for the TE7 carbon beads and MIL-53 cover an unrealistically large range of pore volumes. Figure 4.29 also shows a very sporadic and improbable power pore volume relationship for the TE7 carbon beads, and very unrealistic values of the pore volume at low pressures for certain temperatures for MIL-53.

Just as with the linear pore volume dependence on pressure, even though the RMSR value was improved with the inclusion of a power pore volume dependence on pressure, the unrealistic parameter values in conjunction with the large error bars observed for some parameters indicates that the RMSR value was only improved due to the increase in the number of parameters, and not by representing a real physical phenomenon within adsorption. Therefore, a power pore volume dependence on pressure was not included within the DV model.

#### 4.2.2.2 Pore volume dependence on temperature

The pore volume was then kept constant with pressure to see if there was any trend in temperature. Again the adsorbate density was kept constant with temperature but all other parameters were permitted to vary.

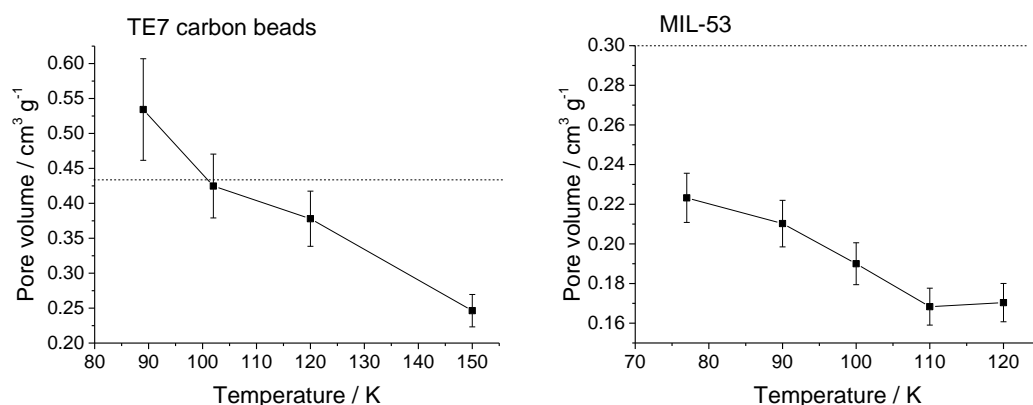


**Figure 4.30 - The pore volume dependence on temperature for the TE7 carbon beads and MIL-53. The horizontal dotted lines represent the experimentally measured pore volumes (described in Section 3.1).**

It can be observed from Figure 4.30 that both materials show a negative trend in pore volume with temperature. The pore volume range provided in Figure 4.30 for the TE7 carbon beads is unrealistically large considering that it is not expected to change in a rigid material, although the range does span the experimentally measured value of the pore volume. The range of pore volume values with temperature is lower for MIL-53, however, all values are significantly lower than the experimentally measured narrow pore volume.

Therefore, it was decided that allowing the pore volume to vary with temperature was not necessary due to the resulting unrealistic values.

Including a pressure and temperature dependence of the pore volume to the known flexible material, MIL-53, does not appear to be an accurate method to determine how the pore volume varies with pressure and temperature, although this would potentially be solved by expanding the number of dependencies studied. The results presented also indicate that it is not worth including a pressure and temperature dependence of the pore volume in the DV model due to the inaccuracy of the parameters, and so the pore volume was kept constant with pressure and temperature.

### 4.2.3 Adsorbate density, $\rho_A$ , dependence on pressure and temperature

The following parameter to be observed as a function of pressure and temperature was the adsorbate density, as it is yet unknown what happens to the density of the hydrogen within the adsorbate with increased pressure and decreased temperature once a monolayer has been formed, as illustrated in Figure 4.31. This would be affected by whether the hydrogen in the adsorbate behaves more like the highly compressible supercritical fluid that it is, or as an incompressible subcritical fluid as has been previously suggested in literature [215]. The density of the hydrogen would be expected to always increase until the monolayer has been formed.

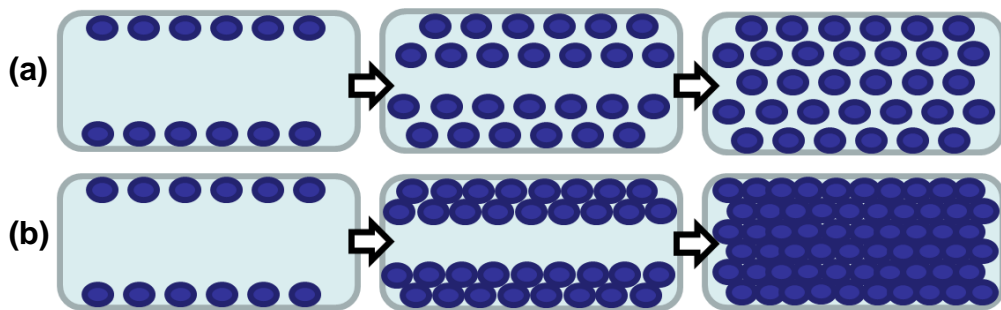


Figure 4.31 - An illustration of the hydrogen inside a pore with (a) a constant density with increased pressure or decreased temperature and (b) an increased density with increased pressure or decreased temperature. The blue balls represent hydrogen molecules and the light blue box represents a pore.

From the computational studies conducted at the University of Queensland (detailed in Sections 3.3.2 and 4.3), the density of the hydrogen within the pore can be calculated, as observed in Figure 4.32.

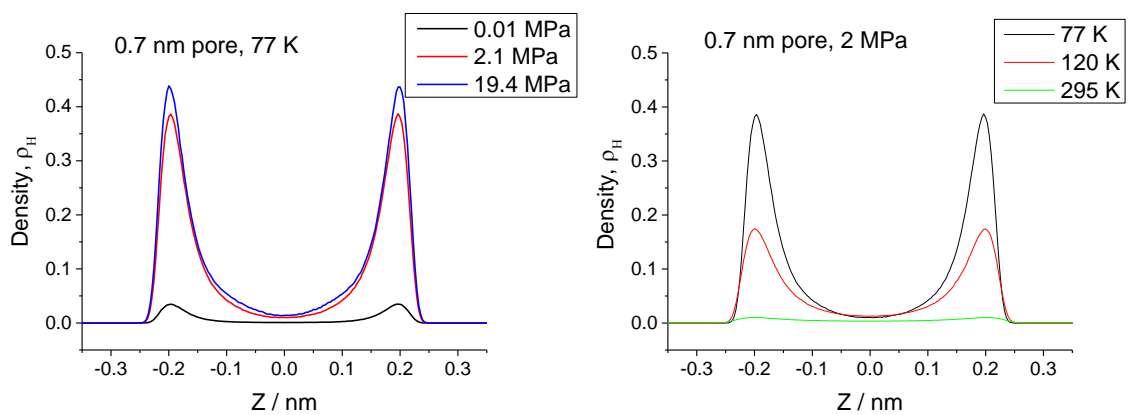


Figure 4.32 – The density profile of hydrogen within a 0.7 nm slit pore with graphene walls at different pressures and temperatures.  $Z$  represents the distance from the centre of the pore.

Figure 4.32 indicates that the density of hydrogen in the adsorbate increases with pressure, but decreases with temperature. The values shown in Figure 4.32 are exceptionally high because the number of bin widths used to calculate the density in the simulations was very large, with the width of each bin being equal to 0.014 nm. Thus, the trends in temperature and pressure could just represent the filling of the monolayers on either side of the pore, instead of the increase in density of the hydrogen post monolayer filling.

#### 4.2.3.1 Adsorbate density dependence on pressure

Therefore, a similar study was conducted to that of the pore volume dependence of pressure and temperature, but this time keeping the pore volume constant, and setting different functions of the adsorbate density. Initially the adsorbate density dependence on pressure was observed using the same functions chosen for the pore volume dependence on pressure, as listed in Table 4.4.

**Table 4.4 - The different functions chosen to represent the adsorbate density as a function of pressure.**

Type of dependence	Equation	Number of parameters
Linear	$\rho_A = \rho_A^0 (1 + \alpha P) \quad (4.27)$	2
Rational	$\rho_A = \rho_A^0 \frac{1 + \alpha P}{1 + \beta P} \quad (4.28)$	3
Power	$\rho_A = \rho_A^0 (1 + P^\alpha) \quad (4.29)$	2
Langmuir type	$\rho_A = \rho_A^0 + (\rho_A^{\max} - \rho_A^0) \left( \frac{\beta P}{1 + \beta P} \right) \quad (4.30)$	3

Again, the functions were each input into the DV model and the RMSR was observed from global fits. This time, the isotherms from the TE7 carbon beads and the MIL-101 materials were used due to the large difference in pore sizes, as this is likely to make a difference to the behaviour of the adsorbate, and potentially its

dependence on pressure and temperature. The TE7 carbon beads have an average pore size of 0.7 nm, and MIL-101 contains pores of 0.7 nm, 2.9 nm and 3.4 nm as stated in Section 3.1. The pore volume was assumed constant and all other parameters were allowed to vary with temperature. The fits can be found in Supplementary Information G, and Table 4.5 highlights the results of the study.

**Table 4.5 - RMSR values using different adsorbate density dependencies of pressure on the TE7 carbon beads and MIL-101 to 3 decimal places.**

$\rho_A$ function	RMSR values / wt%	
	TE7 carbon beads	MIL-101
Linear	0.028	0.055
Rational	0.030	0.118
Power	0.030	0.118
Langmuir type	0.030	0.159
Constant with pressure and temperature	0.036	0.235

As observed from Table 4.5, the linear dependence of adsorbate density on pressure clearly has the greatest improvement on the quality of the fit to the isotherms for both the TE7 carbon beads and MIL-101. Therefore, the temperature dependence of the parameters in the linear dependence, the initial adsorbate density,  $\rho_A^0$ , and alpha,  $\alpha$ , were observed. Similarly to the linear pore volume dependence on pressure, alpha represents the incremental change in adsorbate density with pressure over the initial pore volume.

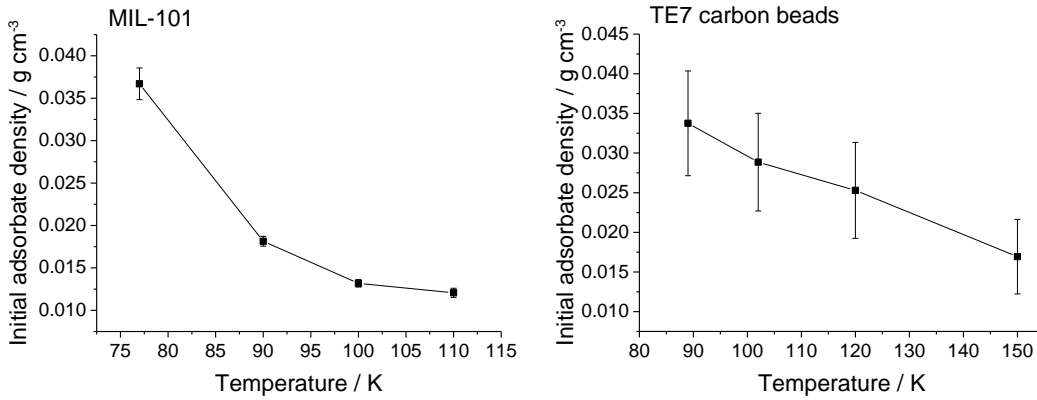


**Figure 4.33 - The initial adsorbate density dependencies on temperature for the TE7 carbon beads and MIL-101, assuming a linear-type dependence on adsorbate density with pressure. The y-error from the fitting is shown for each point. Lines are drawn to guide the eye.**

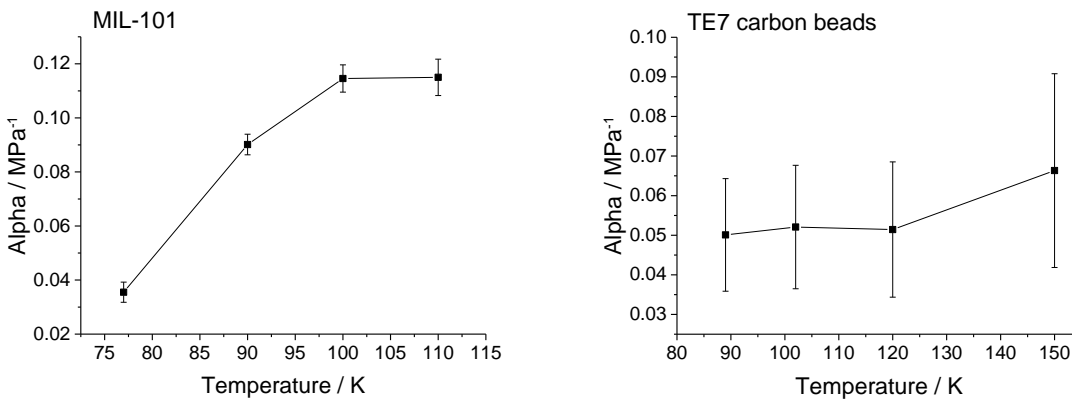


**Figure 4.34 - The dependencies of alpha on temperature for the TE7 carbon beads and MIL-101, assuming a linear-type dependence on adsorbate density with pressure. The y-error from the fitting is shown for each point. Lines are drawn to guide the eye.**

It can be observed from Figure 4.33 that both materials show a negative trend in the initial adsorbate density with temperature, both with relatively small error bars. This is exactly what would be expected as more hydrogen is stored at low temperatures, as explained in the background. The values are also within a realistic range for the initial density of hydrogen in an adsorbate, as they are much lower than that of liquid hydrogen (0.07 g cm<sup>-3</sup> at 20 K and 0.1 MPa). Figure 4.34 generally shows an upward trend in alpha with temperature for both materials, and with all alpha values being positive, implying that the adsorbate density increases with pressure at a more rapid rate at higher temperatures. This could be considered realistic as at higher temperatures the initial adsorbate density is less than that of the lower temperatures and so has the potential to increase to a greater extent.

When the initial adsorbate density and alpha are considered together at each temperature, the predicted linear adsorbate density trends with pressure can be calculated using Equation 4.27 (Figure 4.35).

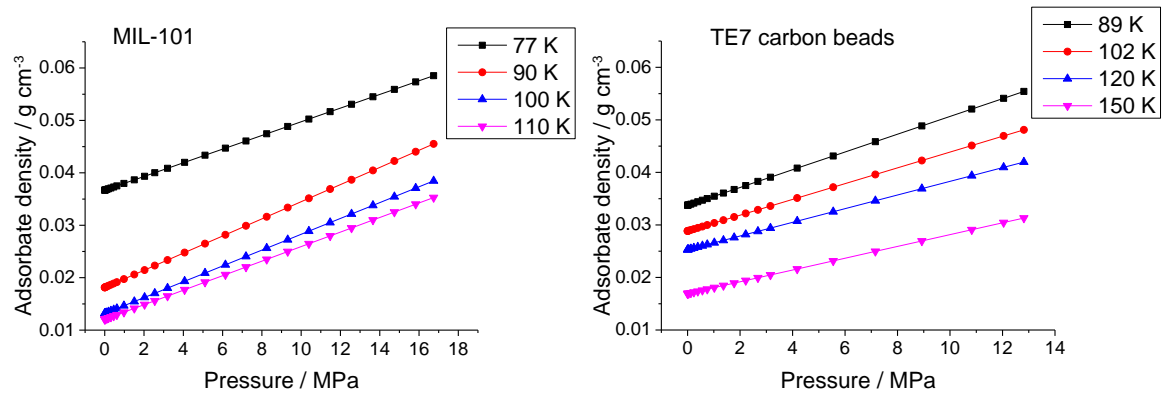


**Figure 4.35 - The predicted linear adsorbate density dependence on pressure from the values provided from the fitting for MIL-101 and the TE7 carbon beads.**

The values for the adsorbate density in Figure 4.35 appear to be realistic as they are within the range of densities expected for hydrogen within the adsorbate, they all follow a constant trend, and they follow the expected trend as shown from the computational results. Therefore, the same study was conducted on the other four materials to certify that the linear trend of adsorbate density with pressure is suitable for all materials. For MIL-101, TE7 carbon beads, AX-21 and MIL-53, the pressure range from the respective lowest temperature isotherm has been used, but for NOTT-101 and ZIF-8, this pressure range was extended so that the predicted adsorbate density values at high pressures could be observed.

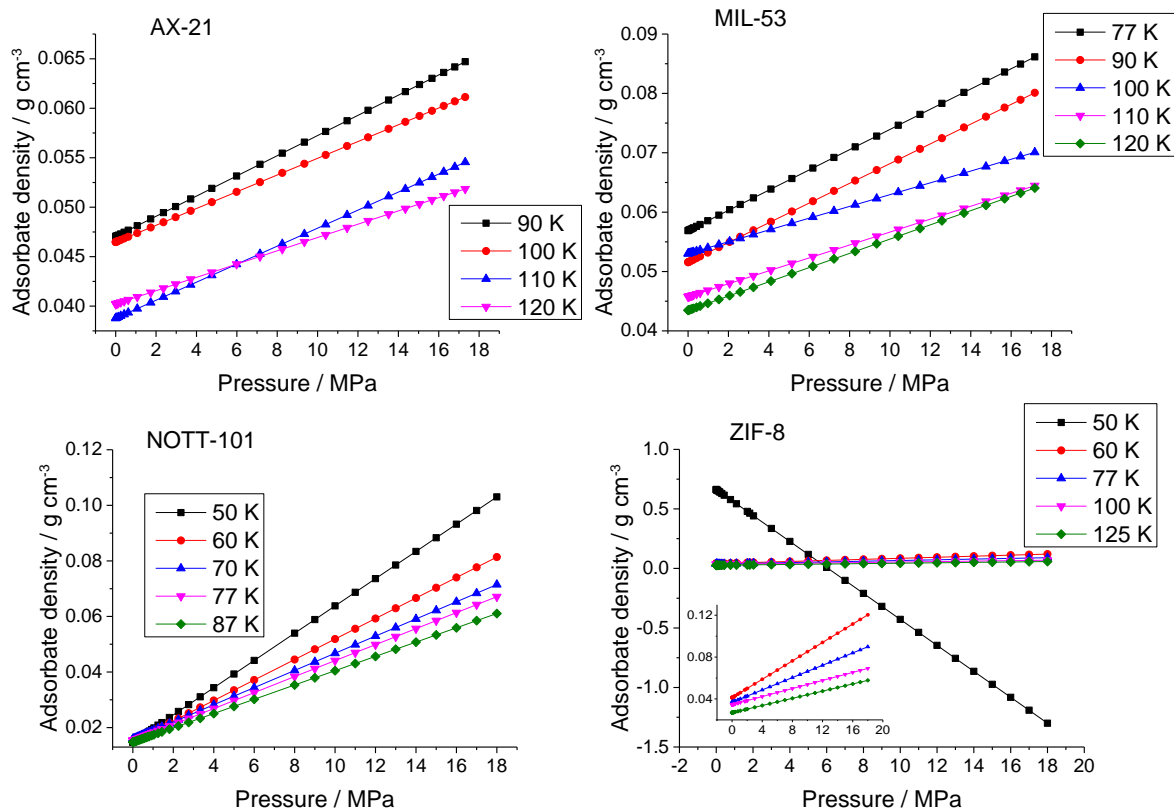


**Figure 4.36 - The predicted linear adsorbate density dependence on pressure from the values provided from the fitting for AX-21, MIL-53, NOTT-101 and ZIF-8. The inset in the graph for ZIF-8 is the same data excluding the 50 K.**

It can be observed from Figure 4.36 that predicting a linear adsorbate density dependence on pressure is not as successful for AX-21, MIL-53 and ZIF-8 as it is for the other three materials. AX-21 and MIL-53 both show a cross-over of the adsorbate density between different temperatures, which would not be expected to occur, as up until the maximum quantity adsorbed, no matter the pressure, lower temperatures should always result in more hydrogen being adsorbed. ZIF-8 shows a huge anomaly in the results with the 50 K data, spanning an entirely unrealistic range of adsorbate density values, and showing a negative trend in adsorbate density with pressure. However, the 50 K isotherm for ZIF-8 does only extend up to 2 MPa and so would be expected to produce less reliable results than the other temperatures.

Another factor to consider when introducing a linear dependence on adsorbate density with pressure into the DV model is how the values of the other parameters within the model are affected, as if they consequently become less realistic then it is not beneficial to include the linear dependence on adsorbate density. Therefore,

the pore volume was observed and compared for keeping a constant adsorbate density with pressure and temperature, and for introducing the linear dependence of adsorbate density. The pore volume was chosen for comparison as it is the value that is most likely to be directly influenced by the adsorbate density; the other unknown parameters,  $b$  and  $c$ , are more directly influenced by each other.

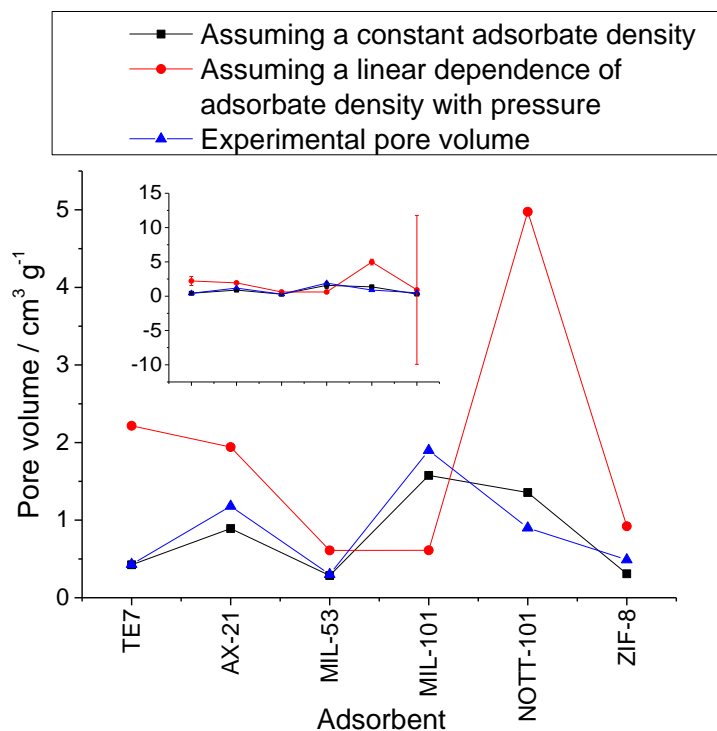


**Figure 4.37 - The pore volume values from fitting the DV model to each adsorbent assuming a constant adsorbate density (black), and assuming a linear dependence of adsorbate density with pressure (red). The experimental values of pore volume calculated as mentioned in the methodology are also included (blue). The lines joining the points are just to guide the eye. The inset is the same data using the same x-axis but including the y-error in the black and red data from the fitting.**

It can be observed from Figure 4.37 that assuming a constant adsorbate density within the DV model results in a particularly good match in pore volume values for all materials with that of the experimental values, whereas assuming a linear adsorbate density with pressure within the DV model results in more sporadic pore volume values, one with a very large y-error.

Therefore, it was concluded that even though introducing a linear adsorbate density with pressure increases the quality of the fit to the isotherms of the adsorbents, and produces realistic looking adsorbate density parameter values, it significantly reduces the accuracy of the pore volume values. Subsequently, the

adsorbate density was decided to be kept constant with pressure within the DV model.

#### 4.2.3.2 Adsorbate density dependence on temperature

The adsorbate density was then kept constant with pressure to observe if there was any trend with temperature. Again the pore volume was kept constant with pressure and temperature, but all other parameters were permitted to vary with temperature.

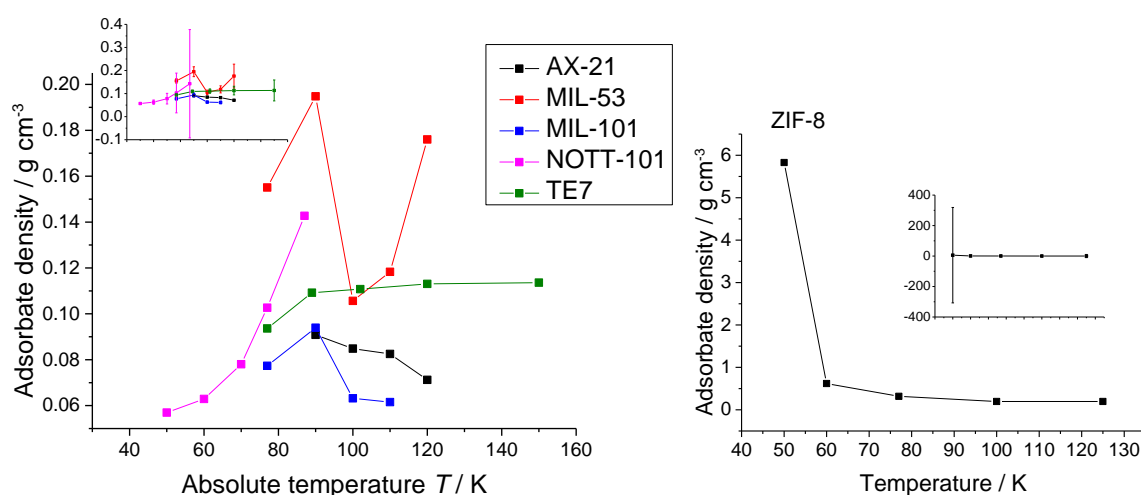


**Figure 4.38 - The adsorbate density dependence on temperature, keeping a constant pore volume. The ZIF-8 values were plotted on a separate graph (right) due to the vastly different values in adsorbate densities to the other materials. The insets on both graphs are the same data with the same x-axis but including the y-error from the fitting. Lines are drawn to guide the eye.**

It can be observed from Figure 4.38 that the adsorbate density variation with temperature is not systematic. Therefore, the adsorbate density was kept constant with both pressure and temperature when used within the DV model.

#### 4.2.4 Independence of the density variation model with pressure and temperature

In order to use the DV model to predict hydrogen uptakes at temperatures outside of those studied in the laboratory, each parameter is required to be independent of pressure and temperature. So far within the DV model, all of the parameters are independent of pressure, but there are six parameters which are dependent on temperature; the four parameters in the rational function approximation for the compressibility factor,  $a_z$  (MPa<sup>-1</sup>),  $b_z$  (MPa<sup>-2</sup>),  $c_z$  (MPa<sup>-1</sup>) and  $d_z$  (MPa<sup>-2</sup>), observed

in bold in Equation 4.31, and the two parameters in the Tóth equation,  $b$  (MPa<sup>-1</sup>) and  $c$  (-), observed in bold in Equation 4.32.

$$Z = \frac{1 + \mathbf{a}_Z P + \mathbf{b}_Z P^2}{1 + \mathbf{c}_Z P + \mathbf{d}_Z P^2} \quad 4.31$$

$$\Theta_A = \frac{\mathbf{b}P}{\left(1 + (\mathbf{b}P)^c\right)^{\frac{1}{c}}} \quad 4.32$$

Using the Tóth equation in global fits of the DV model to the isotherms of each material, and keeping the pore volume and adsorbate density constant with pressure and temperature, the temperature dependence of each of the parameters mentioned above were observed.

#### 4.2.4.1 Affinity parameter, $b$

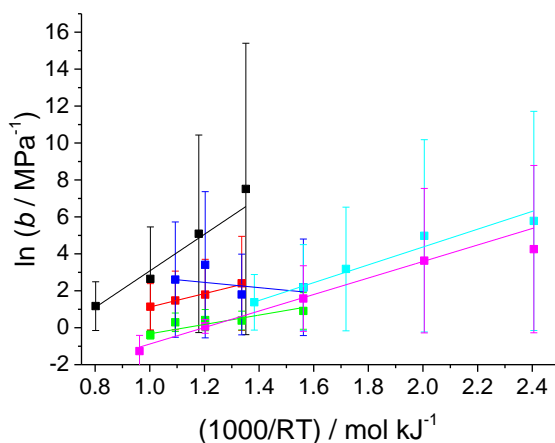
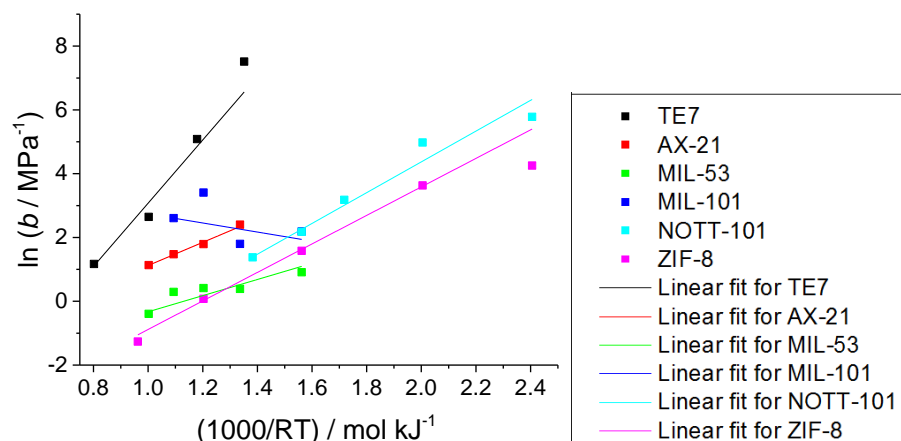
As mentioned in Section 2.4, the affinity parameter,  $b$ , is thought to follow an Arrhenius relationship with temperature.

$$b = A \exp\left(\frac{Q}{RT}\right) \quad 2.2$$

Equation 2.2 can be rearranged into the following form

$$\ln(b) = \frac{Q}{RT} + \ln(A) \quad 4.33$$

which can be used to plot graphs of  $\ln(b)$  vs  $1000/RT$ , resulting in a straight line with a gradient of  $Q$ , related to the heat flow, in kJ mol<sup>-1</sup> (if  $R$  is in MPa cm<sup>3</sup> K<sup>-1</sup> mol<sup>-1</sup>), and a y-intercept of  $\ln(A)$ , where  $A$  is the pre-exponential factor and relates to the entropy of the system [137] (Figure 4.39).



		Value	Standard Error
TE7	Intercept	-6.83698	1.19454
	Slope	9.91256	1.36676
AX-21	Intercept	-2.50634	0.25025
	Slope	3.62806	0.22643
MIL-53	Intercept	-2.862	0.76471
	Slope	2.53249	0.69704
MIL-101	Intercept	4.16101	2.63551
	Slope	-1.42183	1.95792
NOTT-101	Intercept	-5.27863	0.67949
	Slope	4.82437	0.43896
ZIF-8	Intercept	-5.35049	0.55031
	Slope	4.46811	0.45801

**Figure 4.39 - Values for  $\ln(b)$ , without  $y$ -error (top), with  $y$ -error (bottom left), and the values from the fitting (bottom right). The fitting on both graphs is a linear fit.**

The  $y$ -error shown in Figure 4.39 was calculated using propagation of errors, as follows

$$(\ln(b))_{error} = \ln(b) + \ln\left(1 + \frac{(b_{error})}{b}\right) \quad 4.34$$

From Figure 4.39, it can be observed that none of the materials show an exact linear trend in  $\ln(b)$  vs  $1000/RT$ , but that they are mostly not far off. It can also be observed that the  $y$ -error is relatively large for each material except for MIL-53. The values of  $Q$  can be determined from the fitting, and are highlighted in Table 4.6.

**Table 4.6 - The heat of adsorption observed in each material as calculated from the Arrhenius relationship between the affinity parameter,  $b$ , and temperature.  $Q$ , the parameter value relating to the heat of adsorption is given to two significant figures.**

Adsorbent	$Q / \text{kJ mol}^{-1}$ (2 s.f.)
TE7 carbon beads	9.9
AX-21	3.6
MIL-53	2.5
MIL-101	-1.4
NOTT-101	4.8
ZIF-8	4.5

All of the values highlighted in Table 4.6 are within the expected range for the heat of hydrogen adsorption, except for MIL-101, indicating that the use of the Arrhenius equation for the relationship between  $b$  and temperature roughly follows the predicted trends. Some heat of adsorption values also compare favourable to those reported in the literature, for example a value of  $4.5 \text{ kJ mol}^{-1}$  has been observed for ZIF-8 [168], and a range of 2 to  $6 \text{ kJ mol}^{-1}$  was suggested for NOTT-101 [131]. However, some are not as comparable, for example an average value of  $9.5 \text{ kJ mol}^{-1}$  has been calculated for MIL-101 [159].

Thus, if the rest of the parameters can be successfully made independent of temperature, the Arrhenius equation will be utilised for the temperature dependence of  $b$ . The negative value for MIL-101 cannot be explained, although repeating the calculations with more temperatures may improve this value. Due to the lack in accuracy of using the Arrhenius equation, it will not be used in the following studies for the temperature dependence of parameters, and  $b$  will be permitted to vary with temperature.

It has also been speculated that the pre-exponential factor,  $A$ , is dependent on temperature by the following equation [137].

$$A = \frac{\alpha}{k_d \sqrt{2\pi MRT}} \quad 4.35$$

where  $\alpha$  is the sticking coefficient, accounting for non-ideal sticking, and  $k_d$  is the rate of desorption [137]. Therefore, if a multifit is deemed possible for the DV model, the dependence of  $A$  on temperature will be studied.

#### 4.2.4.2 Heterogeneity parameter, $c$

The heterogeneity parameter would be expected to always exist between 0 and 1, with 1 indicating a homogeneous system, and so smaller values of  $c$  indicating more heterogeneous systems. It has been suggested in literature that the higher the temperature, the more homogeneous the system becomes and so the closer  $c$  comes to unity [137]. This is thought to be because at higher temperatures the rates of adsorption and desorption are much faster, and so the hydrogen does not favour the sites with a higher affinity to as large an extent as at lower temperatures.

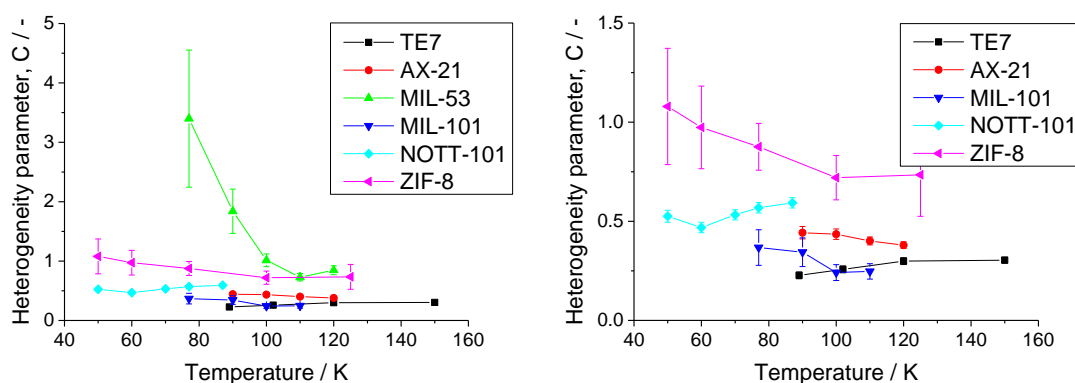


**Figure 4.40 - The heterogeneity parameter dependence on temperature for each material (left) and for each material excluding MIL-53 (right). Lines are drawn to guide the eye. The y-error observed is from the fitting.**

It can be observed from Figure 4.40 that there are no similar trends in  $c$  with temperature between the materials. MIL-53 and ZIF-8 both show values of  $c$  above 1, which should not be possible. All materials except for NOTT-101 and the TE7 carbon beads show a negative trend with temperature, also not expected to happen. However, NOTT-101 shows an initial negative trend in  $c$  followed by an upward trend, therefore the TE7 carbon beads are the only adsorbent showing the expected trend.

It would be possible to set a linear dependence of  $c$  with temperature if necessary, but it would not accurately represent the data presented in Figure 4.40. Therefore,

a linear trend in  $c$  would only be introduced within the DV model if a multifit was deemed possible from the other parameter dependencies on temperature.

#### 4.2.4.3 Compressibility factor parameters, $a_z$ , $b_z$ , $c_z$ and $d_z$

The parameters for the compressibility factor are calculated for a set temperature for each adsorbent as described in Supplementary Information A. They are purely empirical and exist in order to allow for the input of the compressibility factor into the DV model with ease, and so it is unknown what trend they would be expected to follow with temperature. However, they would be expected not to show sporadic values, but should display some sort of trend with temperature as the compressibility of hydrogen is affected by temperature, as hydrogen is thought to behave more like an ideal gas at low temperatures.

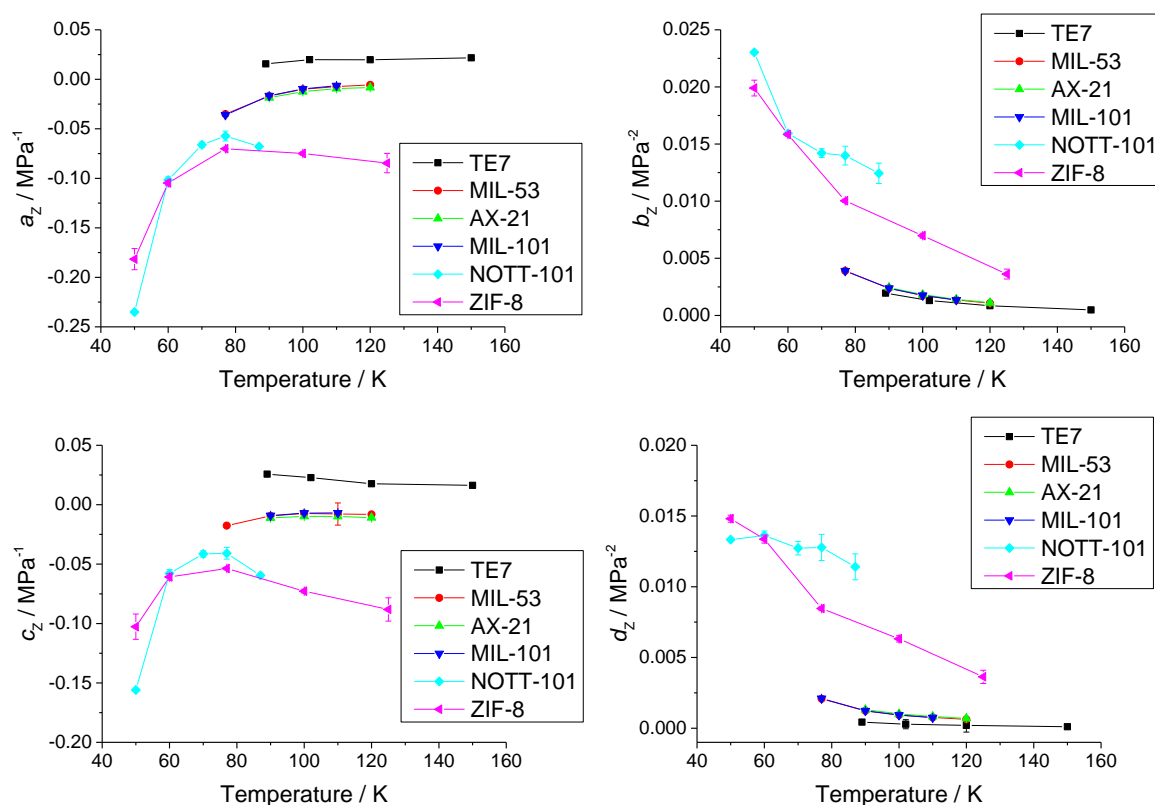


**Figure 4.41** - The dependence of the parameters within the compressibility factor with temperature for each adsorbent. Lines shown are just to guide the eye. The y-error is from the fitting of the rational function to the Leachman equation of state.

It can be observed from Figure 4.41 that even though  $b_z$  and  $d_z$  show a negative trend with temperature,  $a_z$  and  $c_z$  exhibit no real trend with temperature. Attempting to fit any trend onto each of these parameters within the DV model

would result in a very inaccurate representation of the values, and so potentially a much worse fit to the isotherms.

Therefore, due to the lack of trends for the  $c$  value in the Tóth equation with temperature, as well as for the parameters within the compressibility factor, it was determined that a multifit using the DV model would result in very inaccurate results, and so would not be conducted.

#### **4.2.5 Conclusion**

This section has studied each unknown parameter within the DV model in depth to infer whether they could be expanded and improved. A comparison of isotherm equations concluded that individually, they are sometimes better suited to different materials than others, but that overall the Tóth equation shows the best fit to the data. A study was conducted on the pressure and temperature dependence of the pore volume. Four different equations were initially studied for this purpose and input into the DV model, and from the results of the quality of the fits of the study, a linear dependence and a power dependence were deemed the most successful dependencies and so were observed in more detail. However, neither equation showed realistic parameter values or any certain trends with temperature, thus the pore volume was assumed constant with pressure. The temperature dependence of the pore volume was then observed, which again resulted in unrealistic parameter values. The results of this subsequently led to the pore volume in the DV model being set as constant with pressure and temperature.

A similar study on the pressure and temperature dependence of the adsorbate density showed that a linear dependence with pressure appeared to be quite successful in producing realistic parameter values as well as expected trends. However, as a consequence of introducing a linear dependence of adsorbate density with pressure, the values of the pore volume were observed to be much less realistic. Therefore, the adsorbate density was set as constant with pressure, and its dependence on temperature was observed. Yet again, this showed sporadic trends, and so the adsorbate density was also set as constant with temperature. The results of this subsequently led to the adsorbate density in the DV model also being set as constant with pressure and temperature.

Finally, the temperature dependence of the parameters within the DV model that were previously allowed to vary with temperature was conducted in order to determine if the entire DV model could be made independent with respect to temperature. This would allow the prediction of hydrogen uptake at different temperatures to those measured experimentally, but unfortunately was not deemed possible due to the lack of trends in the parameters with temperature.

The section has moulded the DV model, and henceforth, it will be used as shown in Equation 4.36.

$$m_E = \left(\rho_A - \frac{1}{Z} \frac{PM}{RT}\right) 100 v_P \frac{bP}{\left(1 + (bP)^c\right)^{\frac{1}{c}}} \quad 4.36$$

where  $\rho_A$  and  $v_P$  are constant with temperature, but  $b$  and  $c$  are allowed to vary with temperature.

### ***4.3 Verification of the density variation model***

This section will detail the two methods used to verify the DV model. The previous few sections of this thesis have shown that the model fits well to the excess isotherms, but a more substantial verification would be to compare the total and the absolute amounts of hydrogen in the system measured experimentally, and calculated using the DV model. This is because not only would it verify the derivation of the absolute and total uptake equations, but also when the model is fit to the experimental excess isotherms the parameters are allowed to take any value, and so could be completely inaccurate even though the model might appear to fit well to the data. When the model is used to calculate the absolute or total quantities of hydrogen, these parameters are utilised, and thus would verify how well the model has fit to the excess isotherms as well as how realistic the parameter values are.

As mentioned previously, the total and absolute quantities of hydrogen cannot easily be measured experimentally. One of the most suitable methods of probing the hydrogen at the conditions favoured for adsorption whilst negating the adsorbent is inelastic neutron scattering (INS). INS is a very successful technique for analysing hydrogen, which has a much larger cross-sectional area than any other element, allowing for the observation of the behaviour of the hydrogen by penetrating the surrounding material. Because INS can differentiate between the hydrogen in the adsorbate and the adsorptive, the absolute quantity of hydrogen can be determined. The INS work was led by Dr. Valeska Ting at the Rutherford Appleton Laboratories in Oxfordshire, details of which can be found in the methodology.

A suitable method of estimating the total quantity of hydrogen in a system is to use computer simulations. The types of computer simulations that can be used for this study are Grand Canonical Monte Carlo simulations. The simulation work was conducted in collaboration with the group led by Professor Suresh Bhatia at the University of Queensland, who, alongside his group, provided all of the necessary codes and help required to complete this study.

For both of these studies, the TE7 carbon beads were used as a reference material for the reasons stated within the methodology.

### 4.3.1 Inelastic neutron scattering

Neutrons are uncharged sub-atomic particles contained within the nuclei of atoms. The number of neutrons within an atom can vary, resulting in differing isotopes of that atom. For example, hydrogen has three naturally occurring isotopes; protium is the most common hydrogen isotope (over 99.98 % abundance) and consists of a single proton, deuterium consists of one proton and one neutron and is still relatively stable, and tritium consists of one proton and two neutrons, is radioactive, and has a half-life of 12.32 years [216].

Neutrons have been utilised in diffraction studies since the 1940s and in INS since the 1950s, with users ranging from chemists to physicists to biologists [217]. Neutrons are a successful tool for research for a variety of reasons. They are uncharged and so can penetrate matter and approach the nuclei (as opposed to X-rays which probe the electron cloud). Neutrons have a similar wavelength to that of interatomic distances and so can be used for atomic level studies. They can transfer the correct amount of energy to a sample to cause vibrational, translational or rotational excitations which can consequently be detected by the energy transfer. Neutrons can also have a magnetic moment resulting in potential interactions with unpaired electrons [218, 219].

Nuclear diffraction studies are used for determining structures whereas INS is utilised to study atomic vibrations and other excitations. The neutrons are generated in a neutron source *via* either nuclear fission or spallation. Nuclear fission is a chain reaction and consists of bombarding the nucleus of a heavy element, such as uranium, with a neutron which it absorbs, becomes unstable and breaks apart, consequently forming two lighter nuclei and releasing additional neutrons which are then able to be absorbed by another heavy nucleus, and so on [218]. Spallation initiates with the acceleration of negatively charged hydrogen ions using a linear accelerator. The two electrons from each hydrogen ion are then removed by passing through a foil, and the resulting proton is passed into a proton accumulator ring where it is accelerated to even higher speeds and accumulated into pulses. These pulses of high speed protons are then directed at a heavy metal where spallation occurs and the neutrons are released [218]. The neutrons can be slowed down in a moderator to a fixed energy and then aimed at the sample that is required to be tested. Detection is conducted by measuring the energy that is

transferred to the sample when the neutrons hit it, by calculating the difference in the energy of the neutron before and after it has hit the sample.

Neutron scattering is one of the few experimental techniques which can directly access information on the state of hydrogen within a porous material, due to the deeply penetrating nature of the neutrons and the high sensitivity that they have to the presence of hydrogen. Hydrogen has a very large incoherent neutron scattering cross section, enabling the analysis of the hydrogen within the material and in high-pressure *in-situ* sample environments, with the signals from the other elements being overridden.

INS studies are usually performed at low temperatures (<25 K) in order to maximize the resolution of the vibrational spectra [220, 221], however, in order to be comparable with the isotherms of the TE7 carbon beads so that the DV model can be verified, temperatures of 77 K were required.

The INS measurements were conducted on the TOSCA instrument at the ISIS neutron facility at the Rutherford Appleton Laboratories, UK. Recent modifications of the TOSCA instrument enabled high resolution measurements over a very wide range of energy transfer, including very low energies, which allowed for quantitative analysis of the elastic region (-3 to 3 meV) as a function of gas pressure, simultaneous to the inelastic region (3 to 500 meV). The elastic region measures the neutrons that transfer little or no energy to the target H<sub>2</sub> molecules, and so only shows information about the hydrogen in the adsorbate, whereas the inelastic region provides information about the hydrogen in the adsorbate and the adsorptive.

The elastic region was utilised for the comparison with the DV model due to the superior count statistics, and was tracked as a function of pressure at 77 K, at set pressures between 0.016 and 4.69 MPa. Due to the fact that the elastic region only shows adsorbed hydrogen, an absolute isotherm was produced by normalising the total neutron scattering in each spectrum to a standard number of neutron counts (i.e. normalising the peak area in the elastic region (Figure 4.43, A)), and then normalising to the lowest hydrogen loading. This was then compared to the absolute quantity of hydrogen (Equation 4.10) calculated using parameters predicted from fitting the DV model to the 77 K excess TE7 isotherm, which can be

observed in Figure 4.42. Details of the experimental methodology can be found in Section 3.2.6.

$$m_A = 100\rho_A v_P \Theta_A$$

4.10

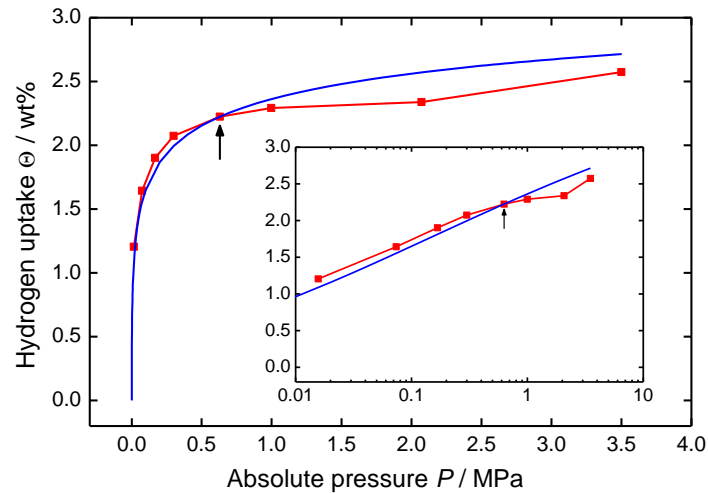


**Figure 4.42 - A comparison between the amount of densified hydrogen detected by INS (red squares), and calculated using parameters from fitting the DV model to the TE7 77 K isotherm (blue line). The red line joining the points is just to guide the eye. The inset is the same data on a logarithmic scale.**

It can be observed that there is quite a strong correlation between the two measurements, verifying that the model for the absolute amount of hydrogen in the adsorbate is a good estimation.

Throughout the INS experiment, another remarkable observation was made. For each different pressure that was measured, there appeared a distinctive peak in the inelastic spectrum at around 14.7 meV, corresponding to the *ortho-to-para* hydrogen conversion (Figure 4.43) [221]. The peak was modelled with a Gaussian distribution and spans approximately 2 meV. There is also a mode at approximately 30 meV, as observed in literature [221]. This is a very clear indication of strongly bound hydrogen that cannot rotate, vibrate or translate, relating to either hydrogen that is strongly bound to the surface of the material, or that has a density equivalent to solid-like hydrogen.

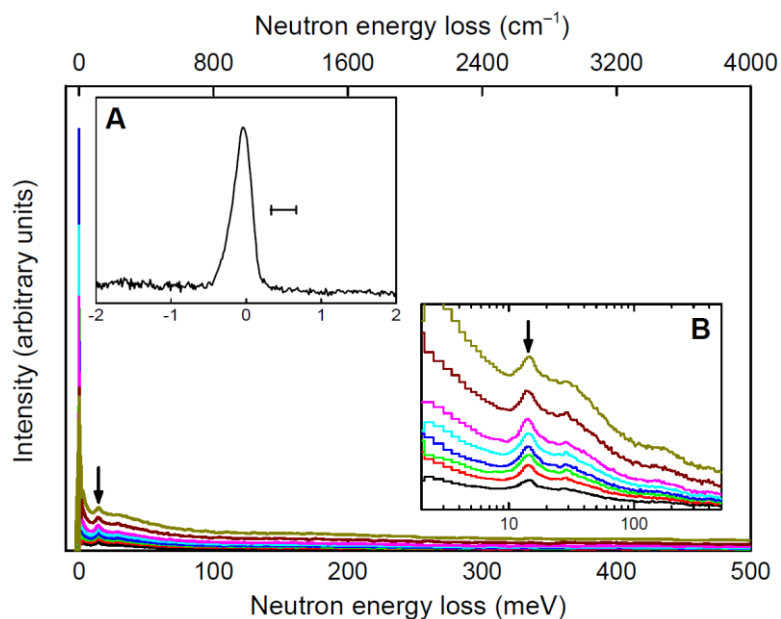


**Figure 4.43 – INS spectra, ascending pressures going from lowest to highest intensity in the main panel, and zoomed in the inset (B). (A) INS elastic spectrum at the lowest pressure [222].**

The elastic region also contains information of the state of the hydrogen within the pore, and because the full-width at half-maximum of the elastic peak was approximately the same as TOSCA's instrumental resolution (0.3 meV), *i.e.* there was no significant broadening of this peak (Figure 4.43 (A)), which would occur for liquid hydrogen due to its mobility [221], this also suggests that the hydrogen was immobilised, and hence solid-like. This, plus the value of the density of the hydrogen found from the DV model fitting as shown in Figure 4.42 being  $0.10 \text{ g cm}^{-3}$ , strongly indicates that there is solid-like hydrogen within the pores of the TE7 carbon beads. The density of solid hydrogen is considered to be  $0.087 \text{ g cm}^{-3}$ , making the value of  $0.10 \text{ g cm}^{-3}$  seem very high, however hydrogen is a highly compressible solid, as can be observed in Figure 4.44, highlighting that  $0.1 \text{ g cm}^{-3}$  is not an unrealistic value for the density of the adsorbate. This is not the first time that densities of this magnitude have been observed from fitting the DV model to the isotherms. In Section 4.2.1.3, when comparing isotherm equations for use within the DV model, the adsorbate density in Figure 4.12 was observed to be much higher than  $0.08 \text{ g cm}^{-3}$  for a range of temperatures and materials. When conducting global fits on each of the six materials using the Tóth isotherm equation within the DV model, and assuming a constant adsorbate density and pore volume with pressure and temperature, the adsorbate density values ranged

between  $0.06$  and  $0.13 \text{ g cm}^{-3}$ , with four out of the six materials showing adsorbate densities above  $0.08 \text{ g cm}^{-3}$ .

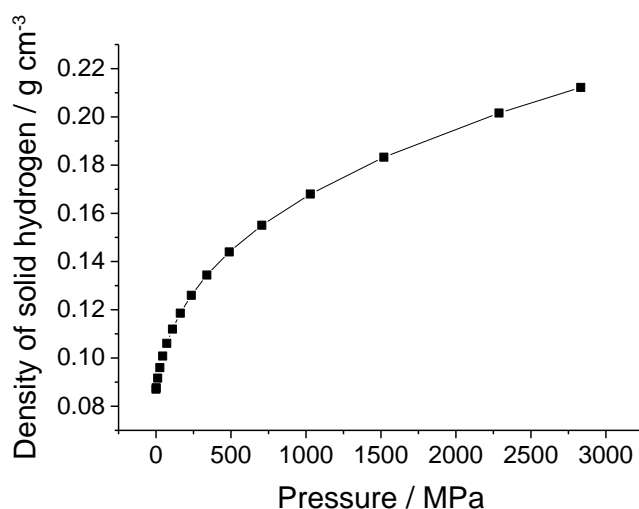


**Figure 4.44 – The density of solid para-hydrogen with pressure at 4 K. Data taken from Silvera [210].**

This is an astonishing result for hydrogen at 77 K, which is far above hydrogen's critical temperature of 33.2 K, and on a carbon surface which generally has weak interactions with the hydrogen, although densities of this type have been observed in literature previously using simulations [223, 224]. A scientific publication on these results is currently being written for submission to Nature Communications [222].

### **4.3.2 Computer simulations**

Computer simulations are a valuable technique for theoretically studying the properties of a molecular substance, the complexity of which makes it near impossible to accurately predict using any other method. They have been widely used for a variety of different topics, but particularly within materials science they are exceptionally useful for studying a materials characteristics and predicting the behaviour of atoms and molecules.

There are many different types of computer simulations, and for studying hydrogen adsorption the two main areas are molecular dynamics, in order to study the kinetics of adsorption and the diffusion of hydrogen, and equilibrium studies, in order to determine uptakes and densities within the pores. As the required output

of the simulation studies conducted was to determine the total uptake of the hydrogen, equilibrium studies were utilised, in particular GCMC simulations.

Monte Carlo refers to statistical sampling and the term was coined in 1945 through the link of statistical sampling within gambling in Monte Carlo [225]. There are many different types of Monte Carlo simulations that are used to date, each assuming different constant parameters within the system. GCMC simulations in particular assume a fixed temperature, volume and chemical potential. This allows for the number of particles to fluctuate throughout the simulation, resulting in a measurement of the amount of adsorbed material with pressure [226].

The acceptable trial moves within the system are the displacement of a molecule, the insertion of a molecule and the removal of a molecule. Each time the computer simulates one of these moves, the free energy of the system must fulfil a certain criteria for the move to be accepted, the acceptance criteria, with the aim of discovering the most energetically favourable position of particles. To do this, the system is required to create a random chain of states, called the Markov chain of states, which results in the random creation of new states, only dependent on the state immediately prior to them [227].

GCMC simulations have been used extensively for hydrogen adsorption within the literature [223, 228-232]. They were chosen for the verification of the DV model as they are able to predict the total hydrogen uptake in a system, which can be compared to the total uptake as predicted by the DV model. For this study, a slit pore model was selected with infinite width walls of pure graphene. The intention was to very basically mimic the structure of the TE7 carbon beads, and so pore widths of 0.7 nm were used (the main pore size in the TE7 carbon beads). The simulations were run as stated in the methodology, and the total amount of hydrogen was calculated using Equation 4.9, with the pore volume found from fitting the DV model to the excess isotherms.

$$m_T = m_E + 100\rho_B v_P \quad 4.9$$

In order to calculate the wt% hydrogen uptake from the simulations, an assumption was required as to the mass of carbon to include, as in the simulation the number of layers of graphene in the walls was set as infinite. Due to the weak

interactions between the hydrogen and the adsorbent, initially only two layers of carbon was assumed, one either side of the pore as depicted in Figure 4.45.

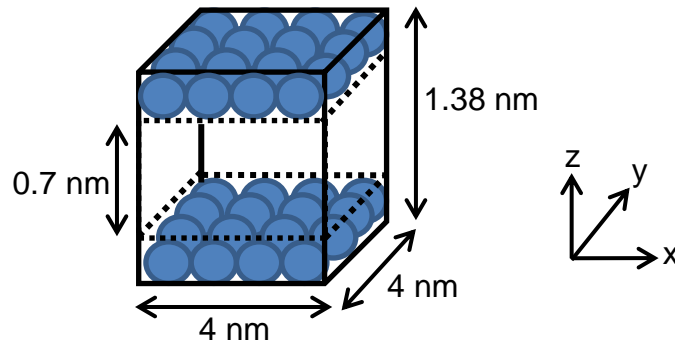


**Figure 4.45 – An illustration of the simulation box used when only assuming one layer of carbon either side of the pore. The blue balls represent the carbon atoms, but are not to scale with the rest of the diagram.**

The simulation box was limited at 4 nm in the x and y directions, the pore size was set as 0.7 nm, and each layer of carbon has a diameter of 0.34 nm [233]. Therefore, in order to calculate the total uptake of hydrogen in wt% from grams, the grams of carbon in the two layers were required. This was calculated by assuming 38.2 atoms of carbon per nm<sup>2</sup> [234] multiplied by the area of each layer, 4 nm<sup>2</sup>, to give the number of atoms of carbon in each layer. This was then divided by the Avogadro constant in order to convert to the number of moles, which was multiplied by the molecular mass of carbon to give the number of grams per layer of carbon. By using this method, the wt% can be calculated as in Equation 4.37.

$$m_H (\text{wt}\%) = \frac{m_H (\text{g})}{m_H (\text{g}) + m_C (\text{g})} \times 100 \quad 4.37$$

Where  $m_H$  is the total hydrogen uptake and  $m_C$  is the mass of carbon.

Figure 4.46 was produced by calculating the total amount of hydrogen from the simulations as explained above, and by comparing to the total amount of hydrogen from the modelling calculated using Equation 4.9.

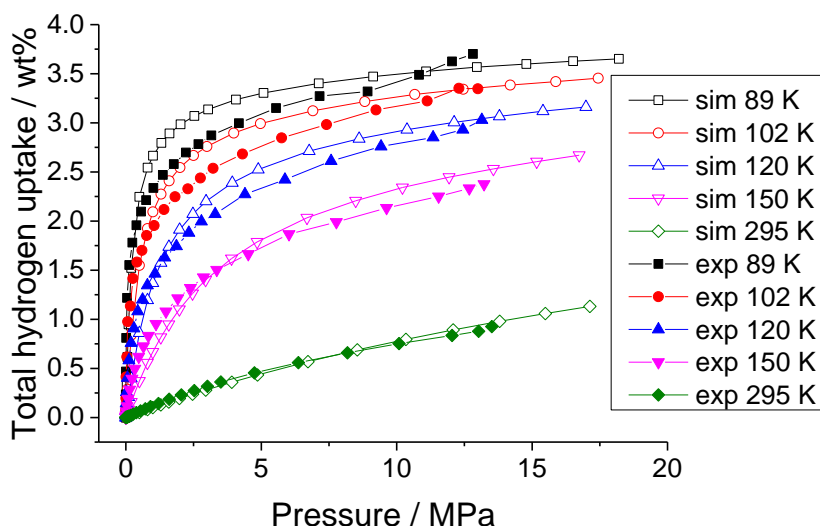


**Figure 4.46 - The total hydrogen uptake with pressure, calculated from simulations (“sim” in the legend), assuming only one layer of graphene either side of the pore for the calculation, and from modelling to experimental isotherms (“exp” in the legend).**

Figure 4.46 shows a very successful compatibility between the total hydrogen uptake calculated from Equation 4.9 using parameters from the DV model fit to TE7 carbon bead isotherms, and the simulated total uptake in a slit pore. This initially suggests that Equation 4.9 is successful at calculating the total uptake, and that the simulations present a good representation of the TE7 carbon beads, and that the assumption of the hydrogen only experiencing interactions with the outer layers of graphene is a correct one.

However, this is more accurate than would be expected, and there are many reasons as to why this should not be the case. Firstly, the simulations assumed an ideal structure, which is certainly not going to be the case for the TE7 carbon beads due to potential structural and chemical heterogeneities such as impurities, non-slit shaped pores, a differentiation of pore width throughout, different sized and shaped pores, irregularities in the adsorbent surface, etc. Also, within the simulations the pore was assumed to have an infinite wall thickness, potentially increasing the attractive forces of the adsorbent to the hydrogen which may not be the case for the TE7 carbon beads, although in the conversion of the simulation results to wt%, only two graphene layers were accounted for for the mass of the adsorbent.

Therefore, even though the results predict that the calculation for the total amount of hydrogen is successful, it is not the most accurate validation method due to the

potential errors mentioned above, and therefore care must be taken when relying on the results.

### **4.3.3 Conclusion**

To conclude this section, inelastic neutron scattering proved to be a successful method at verifying the absolute quantity of hydrogen calculated from the modelling. It also resulted in the discovery that the hydrogen within the pores of the TE7 carbon beads is immobile.

The computer simulations showed a very close fit between the total quantities of hydrogen calculated by simulations and from the modelling. However, this was not deemed a very successful methodology for comparison, due to the assumptions made throughout the simulation studies.

## **4.4 Comparison of hydrogen adsorption vs. compression in a tank**

This section of the thesis introduces a methodology which has been developed to compare the amount of hydrogen stored in a tank containing adsorbent to direct compression of hydrogen in a tank at the same conditions. We call this methodology *design curves*. This is especially important for assessing the benefits of hydrogen adsorption against other more mature methods, such as compression, and to see if there is a range of conditions at which adsorption can store more hydrogen than compression, potentially resulting in a less energy-intensive method of storing hydrogen.

The section starts with an introduction to design curves and an explanation of where they have been used previously within the literature. This will be followed by the derivation of a new equation used to calculate the design curves, introducing the same density variation within the pore as used within the DV model. The equation will be expanded to account for the amount of hydrogen stored per unit volume and per unit mass of the system, using the internal walls of the tank as the system boundary.

The section will show that there is a range of conditions within which adsorption stores more hydrogen than direct compression, but that for each material and temperature, there is a break-even pressure above which compression will always store more hydrogen than adsorption. This value will be shown to be independent on the amount of adsorbent in the tank.

### **4.4.1 History of design curves**

Design curves have been used in literature to compare the amount of hydrogen stored *via* adsorption and compression, and a break-even pressure has been observed, below which adsorption stores more hydrogen than compression, and above which compression stores more hydrogen than adsorption [120]. The break-even pressure is thought to exist due to the adsorbent occupying space that could otherwise contain hydrogen

The design curves were expanded within the literature to introduce a factor that accounts for different quantities of adsorbent in the tank [193]. It was concluded

from this study that the break-even pressure observed in previous work was independent of the amount of adsorbent in the tank.

However, the expansion conducted on the design curves utilised the original model, assuming a single density of hydrogen within the pore, as detailed in the background. The same principle for the design curves as previously shown in the literature was used within this section, but utilising the hydrogen density variation used within the DV model. The major benefit in including the density variation within the design curves is that it provides a value for the adsorbate density,  $\rho_A$ , which is required to input into the equation used to calculate the total amount of hydrogen, required for the design curves. The previous study within the literature required an estimate of the adsorbate density.

#### **4.4.2 Derivation of the new equation used for design curves**

The development of the model presented within this section includes a factor to account for the hydrogen in the intergranular space, as observed in Figure 4.47, where  $V_C$  ( $\text{cm}^3$ ) represents the volume of the container,  $V_B$  ( $\text{cm}^3$ ) is the volume of the bulk hydrogen,  $V_D$  ( $\text{cm}^3$ ) is the displaced volume,  $V_T$  ( $\text{cm}^3$ ) is the total volume of the adsorbent, and  $V_F$  ( $\text{cm}^3$ ) is the volume of the tank containing the adsorbent ( $V_T$  plus intergranular volume). The bulk hydrogen contribution can be separated into the following volumes:  $V_{BI}$  ( $\text{cm}^3$ ) is the volume of the bulk hydrogen in the interstitial sites between the adsorbent,  $V_{BC}$  ( $\text{cm}^3$ ) is the volume of the bulk hydrogen in the section of the container containing no adsorbent and  $V_{BP}$  ( $\text{cm}^3$ ) is the volume of the bulk hydrogen in the pores of the adsorbent. The skeletal volume of the adsorbent including the closed pores is  $V_S$  ( $\text{cm}^3$ ), the open pore volume is  $V_P$  ( $\text{cm}^3$ ), and the volume of the adsorbate is  $V_A$  ( $\text{cm}^3$ ).  $f$  (-) is the fill factor, indicating the ratio of the volume of the tank containing the adsorbent to the total volume of the tank,  $x$  (-) is the packing factor of the adsorbent, indicating the ratio of the total volume of the adsorbent to the total volume of the adsorbent plus intergranular space,  $\Theta_A$  (-) is the fractional filling of the pore *i.e.* the ratio of the adsorbate volume to the pore volume, and  $v_P$  ( $\text{cm}^3 \text{g}^{-1}$ ) is the pore volume per unit mass of the adsorbent,  $m_S$  (g), after degassing.

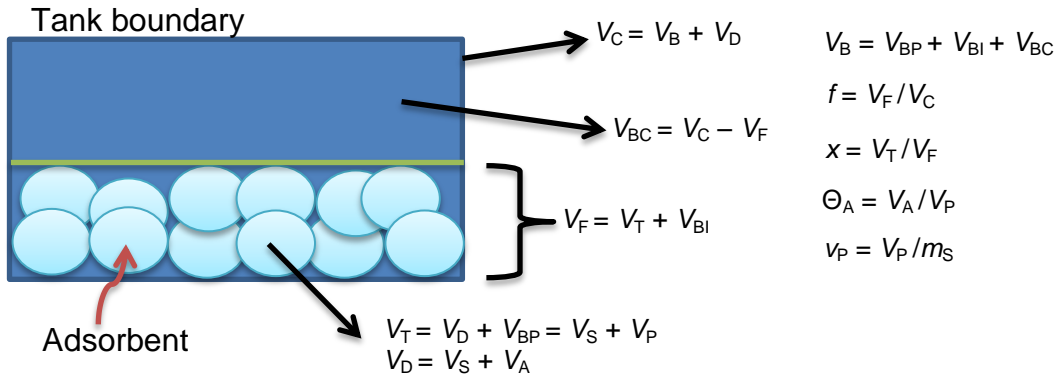


**Figure 4.47 – Representation of the nomenclature used to calculate the amount of hydrogen in a tank containing adsorbent.**

Using this nomenclature, the following derivation for the total amount of hydrogen within a tank containing adsorbent is achieved,

$$m_H = \rho_B V_B + \rho_A V_A \quad 4.38$$

where  $m_H$  (g) is the mass of hydrogen,  $\rho_B$  ( $\text{g cm}^{-3}$ ) is the density of bulk hydrogen and  $\rho_A$  ( $\text{g cm}^{-3}$ ) is the density of the adsorbate.

$$m_H = \rho_B V_{BC} + \rho_B V_{BI} + \rho_B V_{BP} + \rho_A V_A \quad 4.39$$

$$m_H = \rho_B (V_C - V_F) + \rho_B (V_F - V_T) + \rho_B (V_P - V_A) + \rho_A V_A \quad 4.40$$

$$m_H = \rho_B V_C (1 - f) + \rho_B (fV_C - x fV_C) + \rho_B (V_P - V_A) + \rho_A V_A \quad 4.41$$

$$m_H = \rho_B V_C (1 - fx) + \rho_B v_P m_S (1 - \Theta_A) + \rho_A v_P m_S \Theta_A \quad 4.42$$

The mass of the adsorbent can be varied and so the following substitution is required

$$m_S = \rho_S V_S \quad 4.43$$

where  $\rho_S$  ( $\text{g cm}^{-3}$ ) is the skeletal density

$$m_s = \rho_s(V_T - V_p) \quad 4.44$$

$$m_s = \rho_s(V_T - v_p m_s) \quad 4.45$$

Rearranging Equation 4.45 gives

$$m_s = \frac{V_T \rho_s}{1 + v_p \rho_s} \quad 4.46$$

Substituting Equation 4.46 into Equation 4.42 gives

$$m_H = \rho_B V_C (1 - fx) + \rho_B v_p \frac{V_T \rho_s}{1 + v_p \rho_s} (1 - \Theta_A) + \rho_A v_p \frac{V_T \rho_s}{1 + v_p \rho_s} \Theta_A \quad 4.47$$

$$m_H = \rho_B V_C (1 - fx) + \frac{v_p V_T \rho_s}{1 + v_p \rho_s} (\rho_B (1 - \Theta_A) + \rho_A \Theta_A) \quad 4.48$$

$$m_H = \rho_B V_C (1 - fx) + \frac{x f V_C v_p \rho_s}{1 + v_p \rho_s} (\rho_B (1 - \Theta_A) + \rho_A \Theta_A) \quad 4.49$$

As mentioned previously, prior work conducted within the literature showed the break-even pressure to be independent of  $f$ . This can also be proved for Equation 4.49, as it is known that at the break-even point, the mass of hydrogen in a tank containing adsorbent,  $m_H$ , is equal to the mass of hydrogen in a tank empty of adsorbent,  $m_H^0$ , *i.e.*

When

$$P = P_B \quad 4.50$$

$$\frac{m_H^0}{V_C} = \frac{m_H}{V_C} \quad 4.51$$

where  $P_B$  is the break-even pressure. It is also known that for a tank empty of adsorbent,

$$\frac{m_H^0}{V_C} = \rho_B \quad 4.52$$

Substituting Equations 4.49 and 4.52 into Equation 4.51 gives

$$(1 - fx)\rho_B + \frac{fxv_P\rho_s}{1 + v_P\rho_s}(\rho_B(1 - \Theta_A) + \rho_A\Theta_A) = \rho_B \quad 4.53$$

$$\rho_B - \rho_B fx + \frac{fxv_P\rho_s}{1 + v_P\rho_s}(\rho_B(1 - \Theta_A) + \rho_A\Theta_A) = \rho_B \quad 4.54$$

$$\frac{fxv_P\rho_s}{1 + v_P\rho_s}(\rho_B(1 - \Theta_A) + \rho_A\Theta_A) = \rho_B fx \quad 4.55$$

$$\frac{v_P\rho_s}{1 + v_P\rho_s}(\rho_B(1 - \Theta_A) + \rho_A\Theta_A) = \rho_B \quad 4.56$$

Therefore, it does not matter what the value of  $f$  is at  $P = P_B$ .

#### 4.4.3 Design curves per unit volume and per unit mass

Equation 4.49 gives the total amount of hydrogen in a tank of volume  $V_C$ . This can be easily rearranged to give the volumetric hydrogen capacity by dividing by the volume of the container

$$\frac{m_H}{V_C} = \rho_B(1 - fx) + \frac{fxv_P\rho_s}{1 + v_P\rho_s}(\rho_B(1 - \Theta_A) + \rho_A\Theta_A) \quad 4.57$$

The volumetric capacity is a useful comparison for adsorption vs. compression, as it is a quantity that is independent of the tank size.

Equation 4.49 can also be adjusted in order to calculate the amount of hydrogen stored per unit mass of the container, using the internal walls of the tank as the system boundary.

The mass of the contents of the tank,  $m_W$  (g), is

$$m_w = m_H + m_S \quad 4.58$$

where  $m_S$  (g) is the mass of the adsorbent and  $m_H$  (g) is the mass of the hydrogen. The mass of the hydrogen has been calculated (Equation 4.49) and the mass of the adsorbent is given in Equation 4.46. Substituting these into Equation 4.58 gives

$$m_w = \frac{xfV_C\rho_S}{1+v_P\rho_S} + \rho_B V_C(1-fx) + \frac{xfV_C v_P \rho_S}{1+v_P\rho_S} (\rho_B(1-\Theta_A) + \rho_A \Theta_A) \quad 4.59$$

$$m_w = \rho_B V_C(1-fx) + \frac{xfV_C\rho_S}{1+v_P\rho_S} (1+v_P\rho_B(1-\Theta_A) + v_P\rho_A \Theta_A) \quad 4.60$$

Equations 4.49 and 4.60 can be used to observe the amount of hydrogen per unit mass of the system

$$\frac{m_H}{m_w} = \frac{\rho_B V_C(1-fx) + \frac{xfV_C v_P \rho_S}{1+v_P\rho_S} (\rho_B(1-\Theta_A) + \rho_A \Theta_A)}{\rho_B V_C(1-fx) + \frac{xfV_C\rho_S}{1+v_P\rho_S} (1+v_P\rho_B(1-\Theta_A) + v_P\rho_A \Theta_A)} \quad 4.61$$

Equation 4.61 utilises the internal tank walls for the system boundary, and so when comparing adsorption to compression it is with the assumption that the same tank would be required for both. In reality, as the systems are being observed at equivalent conditions, the tank requirements would be the same for both.

#### 4.4.4 Adsorption vs. compression

The TE7 carbon beads were chosen as an example comparison between the amount of hydrogen stored *via* adsorption and *via* compression, and the Tóth isotherm equation was used. Parameters  $b$  and  $c$  from the Tóth isotherm equation were estimated using the DV model for a non-linear fit on the isotherms and were allowed to vary with temperature.  $\rho_A$  was also estimated from the fitting but assumed to be constant with temperature and pressure, and  $\rho_B$  was found using a rational function approximation to the Leachman equation of state.  $f$  and  $x$  are variables, and  $\rho_S$  and  $v_P$  were determined experimentally. For the gravimetric capacity, the tank was set as 30 litres.

Figure 4.48 shows the volumetric and gravimetric energy densities for a variety of pressures (0 - 22 MPa), temperatures (89 - 295 K) and amounts of adsorbate.

Arbitrary values were chosen for  $f$  and  $x$  to give a broad range of quantities of adsorbate; from direct compression of hydrogen ( $fx = 0$ ) to a combination of adsorption and direct compression of hydrogen ( $0 < fx < 1$ ) to complete adsorption of hydrogen ( $fx = 1$ ).

The 295 K isotherms for the TE7 carbon beads were also used here, unlike previous studies, due to the interest in the amount of hydrogen stored *via* adsorption and compression at room temperature, although care is taken when analysing the results due to the problems mentioned in Section 0.

It is also worth noting that a comparison with liquefied hydrogen was not included in this study as high pressures would not realistically be used, but the volumetric density of liquefied hydrogen is approximately  $0.07 \text{ g cm}^{-3}$ , way above that observed for adsorbed and compressed hydrogen in Figure 4.48, and the mass density would be the same as that of compression using the inner walls of the tank as the system boundary.

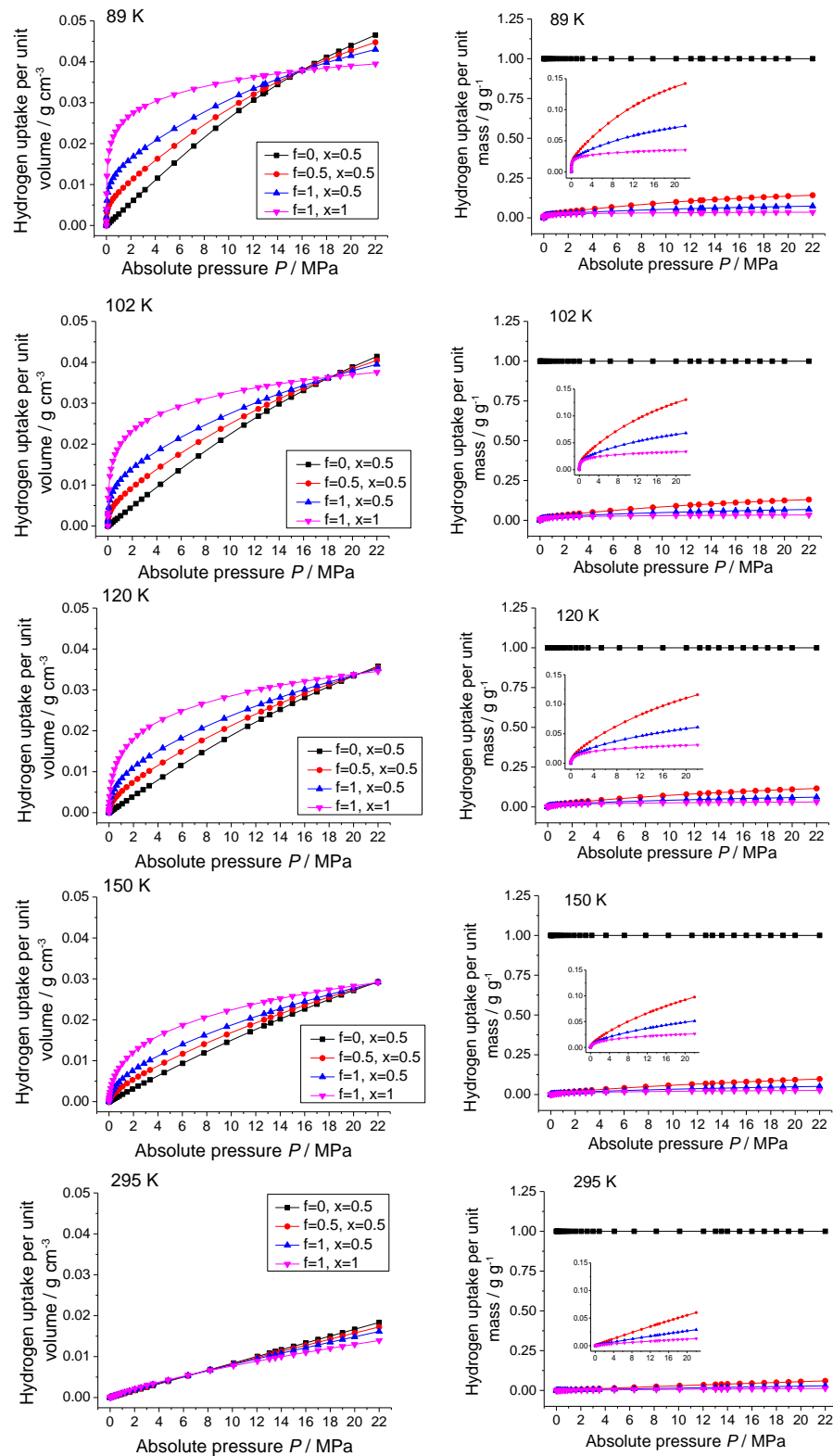
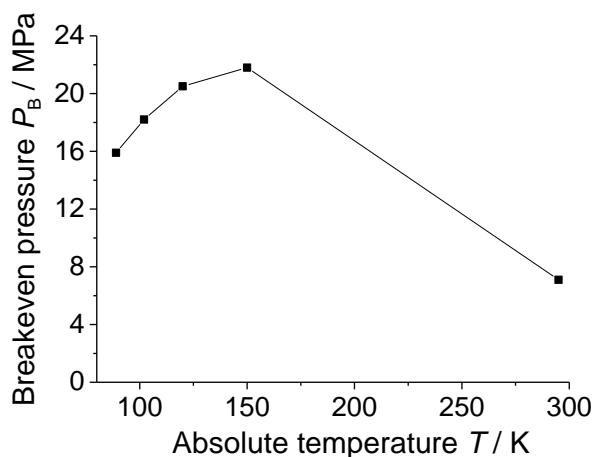


Figure 4.48 - The volumetric density (left) and the mass density (right) of hydrogen in a tank filled with varying quantities of TE7 carbon beads at different temperatures and pressures. The insets show zoomed regions of the same data.

To determine whether Equations 4.57 and 4.61 are accurate, the values calculated for direct compression ( $f = 0$ ) were compared to those found in literature [235].

Figure 4.49 shows break-even pressures,  $P_B$ , for the TE7 carbon beads, the pressure up until which adsorption has a higher energy density than compression.



**Figure 4.49 – The break-even pressures for TE7 carbon beads as a function of temperature. The lines joining the points are to guide the eye.**

As seen in Figure 4.49, when observing the volumetric density for the TE7 carbon beads there is an optimum temperature at which adsorption is favoured up to a higher pressure than direct compression, independent of the amount of adsorbent present, as also observed in our previous work [193].

When observing the mass density in Figure 4.48, compression is always favoured. However, if the system boundaries were broadened, for example including the weight of the tank, adsorption would become more favourable than compression at low pressures. This is because when just using the internal surface of the tank as the system boundary, almost all of the included weight in the system is that of the adsorbent which is not present in compression, whereas the broader the system boundary, the more weight that is relevant for compression as well as adsorption.

These calculations have also been performed for the other materials detailed in the methodology. The results of these calculations can be found in Supplementary Information H. When the break-even pressures found for the volumetric density of hydrogen in each material against temperature are compared, it can be observed that there does not appear to be an obvious trend (Figure 4.50).

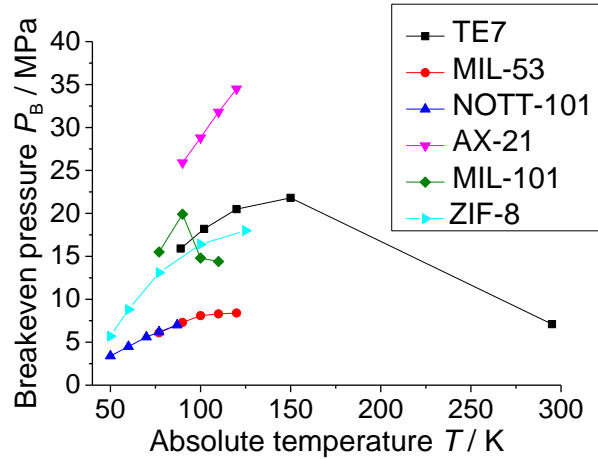


**Figure 4.50 – Break-even pressure as a function of temperature for a range of materials. The lines joining the points are to guide the eye.**

For AX-21 and NOTT-101, within the temperature range studied for these materials, there appears to be a fairly linear increase in break-even pressure with temperature. ZIF-8 and MIL-53 show more of a curve, and MIL-101 and the TE7 carbon beads both show an optimum temperature for the break-even pressure. This could indicate that if a broader range of temperatures was studied, there would always be an optimum temperature for the break-even pressure.

Figure 4.48, Figure 4.49, and Figure 4.50 suggest that, provided enough hydrogen per unit volume and per unit mass can be stored *via* adsorption below the break-even pressures, then adsorption is favourable to compression, as it diminishes the energy penalty of the storage system by using conditions closer to ambient. However, if more hydrogen is required to be stored than is possible *via* adsorption in a set tank volume, compression at higher pressures would be a more successful method. This is highlighted in Figure 4.51, which shows that if  $0.025 \text{ g cm}^{-3}$  was required in a tank full of TE7 carbon beads at 89 K, it would only need to be pressurised up to just over 1 MPa. If the same amount was required in a tank half full of adsorbent, 6.4 MPa would be needed, a tank quarter full would need a pressure of 8.2 MPa, and for direct compression, 9.6 MPa would be required.

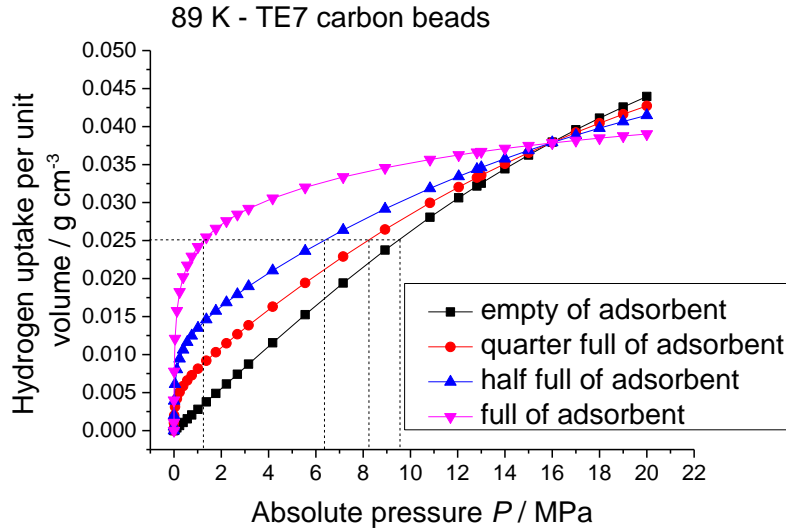


Figure 4.51 – The design curve for the TE7 carbon beads at 89 K, highlighting the different pressures that would be required to store  $0.025 \text{ g cm}^{-3}$  of hydrogen in a tank containing different amounts of adsorbent. The lines joining the points are to guide the eye.

#### 4.4.5 Conclusion

An equation has been successfully derived to calculate the volumetric density and mass density for the adsorption of hydrogen in a tank containing varying quantities of adsorbent at different temperatures and pressures. It has been observed that when using this equation to directly compare the adsorption and compression of hydrogen, the volumetric density of hydrogen stored *via* adsorption is always better than that of compression up to a certain pressure, which for the TE7 carbon beads at 150 K is approximately 21 MPa. Therefore, for applications where small quantities of stored hydrogen are required and where weight is not an issue, adsorption is preferable to compression as it can occur at pressures closer to ambient conditions.

## 4.5 Hydrogen adsorption in aviation

The previous section of this thesis highlighted a methodology for comparing the amount of hydrogen stored in a tank *via* adsorption and compression. In order to consider the use of hydrogen in aviation, this comparison needs to be extended to include other energy systems, including current jet fuel, in order to get an idea of the energy densities of hydrogen compared to other systems and to see if it shows potential as an alternative aviation fuel. Throughout the section the amount of energy per unit volume will be referred to as the energy density and the amount of energy per unit mass will be referred to as the specific energy.

Also, in order to consider hydrogen for use in aircraft, other factors aside from the energy density need to be considered. One preliminary study has been conducted on the potential of “cryo-charging” a tank in order to assess the benefits compared to directly compressing hydrogen to high pressures.

A small summary of alternative areas that are required to be regarded before adsorption of hydrogen can be considered for aviation is then presented.

### 4.5.1 Comparison to alternative energy systems

Equation 4.57, used to calculate the volumetric energy density in Section 4.4, can be further adjusted to calculate the energy available per unit volume instead of the quantity of hydrogen available per unit volume, providing an easier comparison with other systems such as batteries and kerosene. The energy is accounted as follows, assuming the production of H<sub>2</sub>O(g) and not H<sub>2</sub>O(l)

$$\frac{\Delta H_f(\text{H}_2\text{O}(\text{g}))}{M(\text{H}_2)} = \frac{241.8 \text{ kJ mol}^{-1}}{2.016 \text{ g mol}^{-1}} = 120 \text{ MJ kg}^{-1} \quad 4.62$$

Therefore, a factor of 120 can be used in order to convert Equation 4.57 from grams of hydrogen per cm<sup>3</sup> to mega joules of energy available,  $E_H$ , per litre.

$$\frac{E_H}{V_C} = 120 \left( \rho_B (1 - fx) + \frac{xfv_p \rho_S}{1 + v_p \rho_S} (\rho_B (1 - \Theta_A) + \rho_A \Theta_A) \right) \quad 4.63$$

In the same way, Equation 4.61 can be adjusted to account for the amount of energy per unit mass in MJ kg<sup>-1</sup> as opposed to the amount of hydrogen per unit mass in g g<sup>-1</sup>.

$$\frac{E_H}{m_w} = 120 \left( \frac{\rho_B V_C (1 - f\bar{x}) + \frac{xfV_C v_P \rho_S}{1 + v_P \rho_S} (\rho_B (1 - \Theta_A) + \rho_A \Theta_A)}{\rho_B V_C (1 - f\bar{x}) + \frac{xfV_C \rho_S}{1 + v_P \rho_S} (1 + v_P \rho_B (1 - \Theta_A) + v_P \rho_A \Theta_A)} \right) \quad 4.64$$

However, it is worth noting here that both Equations 4.63 and 4.64 employ the internal tank walls as the system boundary due to the uncertainty in the rest of the system, and so care must be taken in the comparison of hydrogen storage with other systems, as it will not account for the different weights or volumes required for the balance-of-plant. This limitation of the system boundary is particularly significant when comparing to systems such as batteries which do not require heavy tanks.

#### 4.5.1.1 Example calculation

A preliminary comparison between the energy density and specific energy *via* hydrogen storage and alternative energy technologies is shown, using the TE7 carbon beads as an adsorbent at 89 K. The data is the same as that used in Section 4.4, but using the energy stored per unit mass and volume instead of the amount of hydrogen, and includes the data for other energy systems (kerosene, lithium-ion batteries and lead-acid batteries).

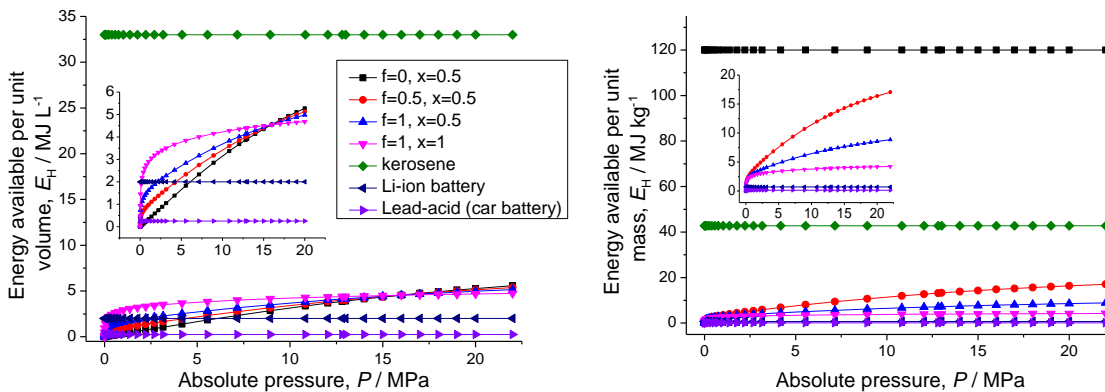


**Figure 4.52 - A comparison of the energy stored per unit volume (left) and per unit mass (right), for potential aviation energy technologies compared to hydrogen storage in a tank containing varying quantities of TE7 carbon beads at 89 K. The insets show zoomed regions of the same data. The lines joining the points are to guide the eye.**

Figure 4.52 shows that hydrogen adsorption in TE7 carbon beads at 89 K has a much lower energy density and specific energy than kerosene at all pressures calculated. Compressed hydrogen has a higher specific energy than kerosene, but a much lower energy density. At high pressures, adsorbed hydrogen shows a

higher energy density and specific energy than both battery technologies, but a complete comparison would require accounting for the full storage system. As mentioned previously, the system boundaries are particularly significant when comparing to battery storage, as no additional tank is required, making the quantities for adsorbed and compressed systems overrepresented in both graphs shown in Figure 4.52.

These trends are further confirmed in Figure 4.53, which depicts the comparison of the energy density and specific energy of various energy storage technologies. The change in energy density and specific energy when using the different adsorbents is fairly insignificant when comparing to other systems such as kerosene.

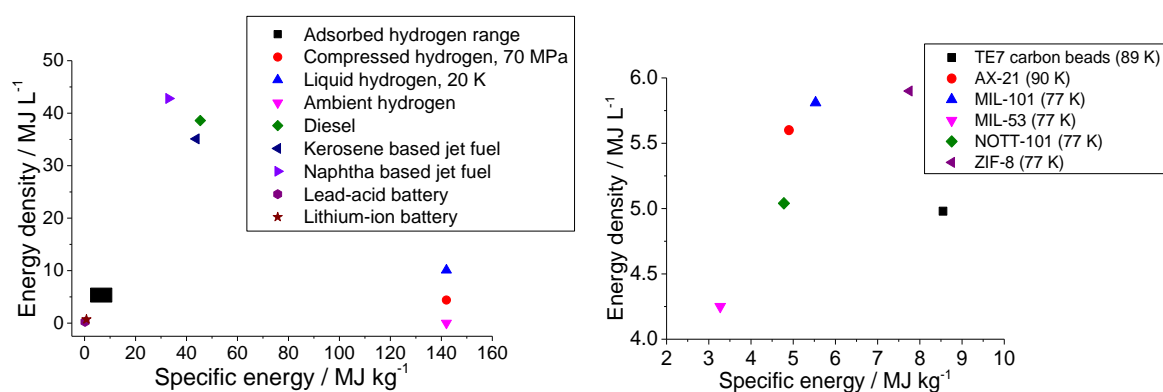


**Figure 4.53 - (Left) The energy density and specific energy of various energy storage technologies [236–238]. The adsorbed hydrogen range contains the same data observed in (right), which is zoomed in to the various hydrogen adsorption materials at 20 MPa in a tank half filled with adsorbent.**

To conclude, preliminary studies show compression and adsorption of hydrogen to be both deemed comparable to battery technologies in terms of energy density and specific energy, but cannot yet compete with standard jet fuels such as kerosene. For hydrogen to be utilised in aviation, materials with a higher hydrogen capacity are required in order to make the energy density and specific energy more comparable to current systems.

#### 4.5.2 Cryo-charging of hydrogen tanks

Comparing the energy density and specific energy of hydrogen to other systems is not the only consideration that needs to be studied to see how successful hydrogen could be for use in aircraft. One particular problem which needs to be considered is the most energetically favourable method of refuelling the tanks with

hydrogen. The theoretical energy required to compress hydrogen at a constant temperature from 2 MPa to 35 MPa or to 70 MPa is 1.05 kWh kg<sup>-1</sup> and 1.36 kWh kg<sup>-1</sup> respectively. To liquefy the hydrogen at 0.1 MPa from 300 K (including the conversion to para-LH<sub>2</sub>), much more energy is required at 3.9 kWh kg<sup>-1</sup> [239]. However, realistically greater energy requirements are necessary for compression and substantially higher energy requirements are needed for liquefaction due to inefficiencies within the processes. Therefore, a novel method of utilising an adsorbent in order to refill a hydrogen tank was studied in order to determine if it could be done at less energy than liquefaction and compression.

This method involves introducing a quantity of adsorbent into a tank, and filling the tank up with hydrogen at 77 K and low pressures, termed “cryo-charging”. The tank would then be allowed to heat up to room temperature, negating the requirement of a heavy liquid nitrogen system on-board to keep it cool. As the tank warms up to room temperature, a significant pressure increase would be expected, as suggested in Figure 4.54, which can be calculated and compared to direct compression.

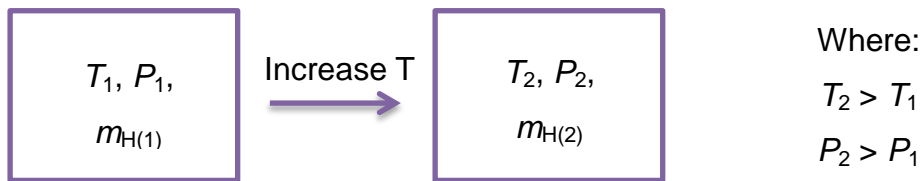


**Figure 4.54 – A representation of the nomenclature used to calculate the increase in pressure when allowing an increase in temperature in a closed tank containing an adsorbent.**

The adsorbent used for the study was the reference material, TE7 carbon beads. The calculation was based on the design curve equation assuming a density variation within the pore, Equation 4.57, and making the assumption that the mass of hydrogen per unit volume remains constant as the tank is allowed to heat up to room temperature. This way, the initial and final temperature can be set, and then only either the initial pressure, mass of hydrogen per unit volume, or the final pressure needs to be known in order to calculate the remaining two values.

$$\frac{m_H}{V_C} = \rho_B (1 - fx) + \frac{xfv_p \rho_S}{1 + v_p \rho_S} (\rho_B (1 - \Theta_A) + \rho_A \Theta_A) \quad 4.57$$

The values of the parameters were obtained the same way as in Section 4.4. Once all of the conditions were determined for the cryo-charging, a comparison could be made to direct compression by calculating the pressure required to store the same amount of hydrogen, using the gas laws (Equation 4.65).

$$P = \frac{(m_H / V_C)ZRT}{M} \quad 4.65$$

Three different types of calculation are going to be conducted in order to get a preliminary view on whether cryo-charging may be favourable to direct compression. All of them are conducted assuming varying quantities of adsorbent in the tank.

1. Firstly, the initial temperature and pressure were set as 77 K and 0.1 MPa. The temperature was then raised to 295 K, and the final pressure was calculated. This was then compared to the pressure that would be required to store the same amount of hydrogen *via* direct compression at 295 K.

**Table 4.7 - The final pressure reached in a tank charged with hydrogen at 77 K and 0.1 MPa following a rise in temperature to 295 K, the corresponding quantity of hydrogen per unit volume within the tank, and the pressure required to store that same quantity of hydrogen per unit volume *via* compression in a tank containing no adsorbent at 295 K. All values are given to 1dp.**

Ratio of adsorbent to free space in the tank ( <i>fx</i> )	Final pressure reached / MPa	Amount of hydrogen per unit volume / mg cm <sup>-3</sup>	Pressure required for direct compression at 295 K / MPa
0	0.4	0.32	0.4
0.2	3.9	3.3	4.0
0.4	7.7	6.4	7.7
0.6	12.1	9.4	11.4
0.8	17.5	12	15.0

The results shown in Table 4.7 highlight that when there are large quantities of adsorbent in the tank, specifically the TE7 carbon beads, higher pressures are required in order to hold the same quantity of hydrogen *via* cryo-charging than direct compression due to the additional space that the adsorbent takes up within the tank. It can also be observed from Table 4.7 that pressures over 17.5 MPa are

not likely to be reached in a tank containing TE7 carbon beads by cryo-charging from atmospheric pressures. Therefore, if only small quantities of hydrogen per unit volume are required, such as the quantities shown in Table 4.7, then cryo-charging could be competitive to direct compression depending on the work required to cool the hydrogen down to 77 K vs. the work required to compress to the pressures shown in the final column in Table 4.7.

2. Secondly, the final pressure was set at 70 MPa, which is of interest due to the current state of the art tanks which are designed to be kept at that pressure. The initial temperature was again set at 77 K and the final at 295 K. The results of this were again compared to the pressure required to store the same amount of hydrogen *via* direct compression at 295 K.

**Table 4.8 - The initial pressure required in a tank filled with hydrogen at 77 K to produce a pressure of 70 MPa following a rise in temperature to 295 K, the corresponding quantity of hydrogen per unit volume within the tank, and the pressure required to store that same quantity of hydrogen per unit volume *via* compression in a tank containing no adsorbent at 295 K. All values are given to 1dp.**

Ratio of adsorbent to free space in the tank ( <i>fx</i> )	Initial pressure required / MPa	Amount of hydrogen / mg cm <sup>-3</sup>	Pressure required for direct compression at 295 K / MPa
0	27	57.8	70
0.2	25	52.6	63.7
0.4	22.5	47.5	57.5
0.6	18.9	42.3	51.2
0.8	13.8	37.1	45

The results shown in Table 4.8 highlight that if a pressure of 70 MPa is required within a tank, it could be achieved by either compressing the hydrogen to 13.8 MPa at 77 K in a tank containing 80 % TE7 carbon beads, or by directly compressing the hydrogen to 70 MPa at room temperature in an empty tank. However, in the situation with the tank containing adsorbent, less hydrogen is stored. Therefore, for comparing cryo-compression and direct compression in a tank at 70 MPa and with the same quantity of hydrogen, a direct comparison would need to be made between compressing hydrogen to 27 MPa at 77 K or to 70 MPa at room temperature. Therefore, again cryo-charging could be competitive

with direct compression if the process of compressing to 27 MPa and cooling to 77 K is more energetically favourable than just compressing to 70 MPa at room temperature.

3. Thirdly, the mass of hydrogen per unit volume was set as the DOE volumetric target for 2015,  $0.04 \text{ g cm}^{-3}$  [54], and the initial pressure, final pressure, and pressure required for direct compression at 295 K were calculated.

**Table 4.9 - The initial and final pressures required in a tank at 77 K and 295 K respectively in order to hold  $0.04 \text{ g cm}^{-3}$  hydrogen, and the pressure required to store that same quantity of hydrogen per unit volume *via* compression in a tank containing no adsorbent at 295 K. All values are given to 1dp.**

Ratio of adsorbent to free space in the tank ( $f_x$ )	Initial pressure required / MPa	Final pressure reached / MPa	Pressure required for direct compression at 295 K / MPa
0	14	48.5	48.5
0.2	14.4	56.6	48.5
0.4	15	68.9	48.5
0.6	16.1	89.5	48.5
0.8	18.4	133	48.5

The results shown in Table 4.9 highlight that it is not worth having TE7 carbon beads in a tank when  $0.04 \text{ g cm}^{-3}$  of hydrogen is required. In an empty tank, this quantity of hydrogen can be reached *via* either compressing to 14 MPa at 77 K, or to 48.5 MPa at room temperature.

Cryo-charging could potentially be beneficial over direct compression, depending on the work required to cool the hydrogen to 77 K and then to compress to a lower pressure compared to compressing to a higher pressure at room temperature. Due to the inefficiency in cooling hydrogen to 77 K, it is initially thought that cryo-charging would not be beneficial over direct compression; however more research would be required to be conducted.

#### 4.5.3 Physisorption of hydrogen in aviation

The calculations conducted above are only a few areas which can aid in determining how suitable physisorption of hydrogen would be for use in aviation. Other aspects that could be considered include the comparison in tank requirements (dimensions, conditions, materials, etc.) for adsorption vs. compression of hydrogen; the recoverable quantity of hydrogen; the requirements of the synthesis, activation, safety and price of the adsorbents; the purity of the hydrogen required for the system and the subsequent number of storage cycles for the adsorbent; the time required to refuel the tank; the lifetime of the stored hydrogen; the most favourable conditions to discharge the hydrogen; more information into the efficiency of the system; and the different uses of the hydrogen on-board, e.g. propulsion vs. power. Initial consideration of these aspects has been conducted within the literature [108, 119, 120, 133, 237, 240-246], and would be fascinating to consider in more detail, as mentioned in the future work chapter of this thesis.

#### **4.5.4 Conclusion**

The design curves derived in Section 4.4 have been expanded to consider the energy available in a tank containing hydrogen, so that the comparison with other energy systems can be conducted. Overall, compression and adsorption of hydrogen have been deemed comparable to battery technologies in terms of energy density and specific energy, but cannot yet compete with standard jet fuels such as kerosene. Therefore, materials with a much higher hydrogen capacity are required in order to make hydrogen comparable to current aviation systems.

A method for recharging hydrogen tanks has been presented, entitled cryo-charging, which would allow tanks to be charged at lower pressures, but at 77 K. However, a comparison of the work required to compress hydrogen at high pressures and room temperature as opposed to compress it to lower pressures but at 77 K is required before cryo-charging can be deemed as a suitable alternative to the direct compression of hydrogen into a tank.

## **Chapter Five**

### **Concluding remarks**

## 5 Concluding remarks

### 5.1 Conclusions

The aim of this thesis was to improve the current method of modelling hydrogen adsorption in nanoporous materials, and to use the improved model to discern the potential of adsorbed hydrogen within aviation. The following conclusions can be drawn:

1. A new model has been derived to fit to experimental hydrogen excess isotherms that accounts for a density variation within the pores of materials, the DV model. The quality of the fits of this model to experimental isotherms has been shown to be comparable to the original model used in literature, and it has the added bonus of allowing for an estimated value of the density of the adsorbate.
2. The excess, absolute and total amounts of hydrogen have been distinguished, and equations to calculate each value have been derived and compared.
3. Each unknown parameter within the DV model has been studied in depth to infer whether they could be expanded and improved, and whether anything could be learnt about the fundamentals of the adsorption process from the expansion of each parameter.
4. A comparison of isotherm equations concluded that individually, they are sometimes better suited to certain materials than others, but that overall the Tóth equation shows the best fit to the data.
5. A study was conducted on the pressure and temperature dependence of the pore volume. Four different equations were initially studied for the pressure dependence of the pore volume, and input into the DV model. From the quality of the fits for each equation, a linear and a power dependence were deemed the most successful and so were observed in more detail. However, neither equation showed realistic parameter values

nor any trends with temperature, and so the pore volume was assumed constant with pressure. The temperature dependence of the pore volume was then observed, which again resulted in unrealistic parameter values. The conclusions of this study subsequently led to the pore volume in the DV model being set as constant with pressure and temperature.

6. A similar study on the pressure and temperature dependence of the adsorbate density showed that a linear dependence with pressure appeared to be quite successful in producing realistic parameter values as well as expected trends with temperature. However, as a consequence of introducing a linear dependence of adsorbate density with pressure, the values of the pore volume were observed to be much less realistic. Therefore, the adsorbate density was set as constant with pressure, and its dependence on temperature was observed. Yet again, this showed sporadic trends, and so the adsorbate density was also set as constant with temperature. The results of this subsequently led to the adsorbate density in the DV model also being set as constant with pressure and temperature.
7. The temperature dependence of the parameters in the DV model that were previously allowed to vary with temperature was conducted in order to determine if the DV model could be made independent of temperature, as this would allow the prediction of hydrogen uptake at different conditions to those studied experimentally. Unfortunately, this was not deemed possible due to the lack of trends in the parameters with temperature.
8. Two different techniques were used to verify the DV model by comparing the results to the total and absolute uptakes as calculated from the model. Inelastic neutron scattering proved to be a successful method at verifying the absolute quantity of hydrogen calculated from the modelling. It also resulted in the astonishing discovery that the hydrogen within the pores of the TE7 carbon beads has a density comparable to that of solid hydrogen. The second method utilised for the verification of the DV model was computer simulations, which showed a very close fit between the total quantities of hydrogen calculated by the simulations and from the

modelling. However, this was not deemed a very successful methodology for comparison, due to the assumptions made throughout the simulation study.

9. An equation has been successfully derived to calculate the energy density and specific energy for hydrogen in a tank containing varying quantities of adsorbent at different temperatures and pressures. It has been observed that when using this equation to directly compare the adsorption and compression of hydrogen, the energy density of hydrogen stored *via* adsorption is always better than that of compression up to a certain pressure, which for the TE7 carbon beads at 150 K is approximately 21 MPa. Therefore, for applications where small quantities of stored energy are required, adsorption is preferable to compression, as it can occur at pressures closer to ambient conditions.
  
10. The design curves were then expanded to consider the energy available in a tank containing hydrogen, so that comparisons with other energy systems could be conducted. Overall, compression and adsorption of hydrogen were deemed comparable to battery technologies in terms of energy density and specific energy, and yet are far off from competing with standard jet fuels such as kerosene. Therefore, materials with a much higher hydrogen capacity are required in order to make hydrogen comparable to current aviation fuel systems.
  
11. A method for recharging hydrogen tanks has been presented, cryo-charging, which would allow tanks to be charged at lower pressures, but at 77 K. However, a comparison of the work required to compress hydrogen at high pressures and room temperature as opposed to compress it to lower pressures but at 77 K is required before cryo-charging can be deemed as a suitable alternative to the direct compression of hydrogen into a tank.

## 5.2 Future work

Some areas of work that would be of particular interest to follow up and expand upon are highlighted below.

1. Even though the density variation within the pore chosen for the DV model was more realistic than just assuming a single density, and also allowed for the density of the adsorbate to be calculated, it still does not match with the expected density variation within the pore as measured *via* simulation studies. It would be very interesting to introduce a more realistic density distribution within the pore to see how the model would fit to excess hydrogen isotherms, and to observe how the parameter values provided would differ from those calculated using the DV model.
2. A repetition of the parameter dependencies on pressure and temperature would be interesting if the experimental error was included in the isotherms. This would expand the range of values that could result in a good quality of fit, and so potentially allow for realistic parameter values within some of the temperature and pressure dependencies selected.
3. The six materials chosen for the isotherm equation study were not enough to fully determine why some isotherm equations fit better to the isotherms of certain materials than others. Therefore, an expansion of this study including more materials at a broader range of temperatures might result in patterns which could determine why this may be. If this was the case, then suggestions could be made as to which isotherm equations should be used with which types of materials, resulting in a more accurate comparison of hydrogen uptakes within literature. The desirable materials would have a broad range of surface areas, micropore volumes and pore sizes.
4. A more successful measurement of the 77 K TE7 isotherm would be useful so that the 77 K data could be included in the temperature and pressure dependence of the parameters within the DV model. Also, a repetition of the measurement of the 89 K TE7 carbon bead isotherm, but submerged in liquid Argon instead of using liquid nitrogen in a cryofurnace, would be

interesting to determine if the kinks in the isotherms at high pressures was due to temperature fluctuations or something else.

5. A repetition of the ESRF study into the pore flexibility of MIL-53(Al) with hydrogen adsorption would be fascinating to determine if hydrogen adsorption does actually cause the material to flex, and if so, whether the inclusion of this pore volume dependence on pressure and temperature would improve the DV model. Also, a repetition of the measurement of the MIL-53 isotherms but starting with both the narrow pore and the large pore phases respectively, to observe any hysteresis and how the isotherms differ from each other. These observations could then be compared to those found by Liu *et al.* [164].
6. It would be very interesting to conduct more INS experiments on hydrogen adsorption in different materials containing different pore sizes to determine if the densities of solid hydrogen are reached for all materials, or just for certain pore sizes. This research is currently on-going, led by Dr. Valeska Ting at the University of Bath.
7. More simulation studies would be required in order to achieve a more accurate representation of the experimental system, so that fewer assumptions would be made. This could be done by inputting the coordinates of a material into the simulation, such as those determined by Farmahini *et al.* [247], or for crystalline materials such as MOFs, and comparing the total uptake to that calculated by fitting the DV model to the experimental isotherms of the material that was simulated.
8. The design curve studies could be expanded by introducing the isotherms from more materials at a broader range of pressures and temperatures. By doing this, the temperature dependence of the break-even pressure may result in certain trends which could be used to determine the optimum temperature at which adsorption stores more hydrogen than compression. Subsequently, this could be utilised to limit the conditions at which

adsorption of hydrogen is deemed useful, and so limit the conditions at which it is studied in detail.

9. The design curve study would also be improved by expanding the system boundaries used, to remove the bias from systems requiring large balance of plant, and for a more complete comparison between systems. In order to do this, knowledge would be required of all of the components for the balance of plant.
  
10. As mentioned in Section 4.5, the preliminary study on cryo-charging would be more complete if the work required for each system was to be calculated. This would involve complicated thermodynamics calculations that there has unfortunately not been time to complete so far.
  
11. As mentioned in Section 4.5, there are many areas within using the adsorption of hydrogen for aviation which would be fascinating to study in detail. In particular, the recoverable quantity of hydrogen could be determined by using the DV model to calculate the amount of hydrogen stored in a tank, and the amount of hydrogen remaining in the tank at the conditions of discharge. To do this, it would be useful to determine the efficiency of the entire system so that the percent of hydrogen actually being used as a fuel compared to the amount stored in a tank could be established.



## 6 References

1. World Bank. World Development Indicators. [http://data.worldbank.org/data-catalog/world-development-indicators?cid=GPD\\_WDI](http://data.worldbank.org/data-catalog/world-development-indicators?cid=GPD_WDI) (accessed 21/05/14).
2. BP, *BP Statistical Review of World Energy 2013*; 2013.
3. Smil, V., *Energy Transitions: History, Requirements, Prospects*, Praeger: California, 2010.
4. U.S. Census Bureau. Historical Estimates of World Population. [http://www.census.gov/population/international/data/worldpop/table\\_history.php](http://www.census.gov/population/international/data/worldpop/table_history.php) (accessed 21/05/14).
5. United Nations Department of Economic and Social Affairs. *The World at Six Billion*; New York, 1999.
6. United Nations Department of Economic and Social Affairs. *World economic and social survey 2013: Sustainable Development Challenges*; New York, 2013.
7. Soubbotina, T. P., World Population Growth. In *Beyond Economic Growth*, World Bank Publications: Washington, DC, 2004; p 205.
8. OECD. About the OECD. <http://www.oecd.org/about/> (accessed 21/05/14).
9. Müller-Steinhagen, H.; Nitsch, J. The Contribution of Renewable Energies to a Sustainable Energy Economy. *Process. Saf. Environ.* **2008**, 83 (B4), 285-297.
10. U.S. Energy Information Administration. *International Energy Outlook 2013*; 2013.
11. Barbir, F., Transition to Renewable Energy Systems with Hydrogen as an Energy Carrier. *Energy* **2009**, 34 (3), 308-312.
12. Central Intelligence Agency. The World Factbook. <https://www.cia.gov/library/publications/the-world-factbook/geos/xx.html> (accessed 29/05/14).
13. Chilingarian, G. V.; Yen, T. F. *Oil shale*. Elsevier: 2011.
14. American Shale oil Corp. Oil Shale Extraction Methods. <http://amso.net/about-oil-shale/oil-shale-extraction-methods/> (accessed 30/05/14).

15. Valkó, P.; Economides, M. J., *Hydraulic Fracture Mechanics*. Wiley: Chichester, UK, 1995.
16. Dorian, J. P.; Franssen, H. T.; Simbeck, D. R. Global Challenges in Energy. *Energ. policy* **2006**, *34* (15), 1984-1991.
17. Dincer, I. Environmental Impacts of Energy. *Energ. Policy* **1999**, *27* (14), 845-854.
18. Likens, G. E.; Herbert Bormann, F.; Johnson, N. M. Acid Rain. *Environment* **1972**, *14* (2) 33-40.
19. World Health Organization. 7 Million Premature Deaths Annually Linked to Air Pollution. <http://www.who.int/mediacentre/news/releases/2014/air-pollution/en/> (accessed 29/05/14).
20. Intergovernmental Panel on Climate Change, *Ipcc fifth assessment report: Climate change 2013*: 2013.
21. United States Environmental Protection Agency. Overview of Greenhouse Gases. <http://www.epa.gov/climatechange/ghgemissions/gases.html> (accessed 21/05/14).
22. Solomon, S.; Plattner, G.-K.; Knutti, R.; Friedlingstein, P. Irreversible Climate Change Due to Carbon Dioxide Emissions. *Proc. Natl. Acad. Sci. U. S. A.* **2009**, *106* (6), 1704-1709.
23. Rohde, R.; Muller, R. A.; Jacobsen, R.; Muller, E.; Perlmutter, S.; Rosenfeld, A.; Wurtele, J.; Groom, D.; Wickham, C. *A New Estimate of the Average Earth Surface Land Temperature Spanning 1753 to 2011*; Berkeley Earth Surface Temperature: Berkeley, 2012.
24. Legislation.gov.uk. Climate Change Act 2008. <http://www.legislation.gov.uk/ukpga/2008/27/contents> (accessed 22/05/14).
25. Steffen, W. *Climate Change 2009 - Faster Changes and More Serious Risks*; Australian Government Department of Climate Change and Energy Efficiency: 2009.

26. Nuclear Energy Institute. World statistics. [http://www.nei.org/resourcesandstats/nuclear\\_statistics/worldstatistics/](http://www.nei.org/resourcesandstats/nuclear_statistics/worldstatistics/) (accessed 22/05/14).
27. World Nuclear Association. Safety of Nuclear Power Reactors. <http://www.world-nuclear.org/info/Safety-and-Security/Safety-of-Plants/Safety-of-Nuclear-Power-Reactors/> (accessed 2/05/14).
28. BBC World Service. Opposition to Nuclear Energy Grows: Global Poll. [http://www.globescan.com/images/images/pressreleases/bbc2011\\_nuclear\\_energy/bbc2011\\_energy.pdf](http://www.globescan.com/images/images/pressreleases/bbc2011_nuclear_energy/bbc2011_energy.pdf) (accessed 19/07/14).
29. Renewable Energy Policy Network for the 21st Century. *Renewables 2013 - global status report*, 2013.
30. U.S. Energy Information Administration. Renewable Energy Explained. [http://www.eia.gov/energyexplained/index.cfm?page=renewable\\_home](http://www.eia.gov/energyexplained/index.cfm?page=renewable_home) (accessed 22/05/14).
31. U.S. Energy Information Administration *Annual Energy Outlook 2012, With Projections to 2035*; 2012.
32. Parliamentary Office of Science and Technology. *Electricity Storage*. <http://www.parliament.uk/documents/post/postpn306.pdf> (accessed 22/05/14).
33. Baker, J. New Technology and Possible Advances in Energy Storage. *Energ. Policy* **2008**, 36 (12), 4368-4373.
34. Ibrahim, H.; Ilinca, A.; Perron, J. Energy Storage Systems—Characteristics and Comparisons. *Renew. Sust. Energ. Rev.* **2008**, 12 (5), 1221-1250.
35. Hoffmann, P.; Harkin, T. *Tomorrow's Energy: Hydrogen, Fuel Cells, and the Prospects for a Cleaner Planet*. MIT Press: 2002.
36. Ramachandran, R.; Menon, R. K. An Overview of Industrial Uses of Hydrogen. *Int. J. Hydrogen Energ.* **1998**, 23 (7), 593-598.
37. Ekins, P. *Hydrogen Energy: Economic and Social Challenges*. Earthscan: 2010.

38. Schlapbach, L.; Züttel, A. Hydrogen-Storage Materials for Mobile Applications. *Nature* **2001**, *414* (6861), 353-358.
39. European Commission's Joint Research Council. *Trends in Global CO<sub>2</sub> Emissions: 2013 Report*. 2013.
40. Mazloomi, K.; Gomes, C. Hydrogen as an Energy Carrier: Prospects and Challenges. *Renew. Sust. Energ. Rev.* **2012**, *16* (5), 3024-3033.
41. Kalamaras, C. M. and Efstathiou, A. M. Hydrogen Production Technologies: Current State and Future Developments. *Conference Papers in Science* 2013, DOI: <http://dx.doi.org/10.1155/2013/690627>.
42. International Energy Agency. *Hydrogen Production and Storage*. <http://www.iea.org/publications/freepublications/publication/hydrogen.pdf> (accessed 22/05/14).
43. Zhou, L. Progress and Problems in Hydrogen Storage Methods. *Renew. Sust. Energ. Rev.* **2005**, *9*, 395-408.
44. BMW. BMW CleanEnergy. [http://www.bmw.com/com/en/insights/technology/efficient\\_dynamics/phase\\_2/clean\\_energy/bmw\\_hydrogen\\_7.html](http://www.bmw.com/com/en/insights/technology/efficient_dynamics/phase_2/clean_energy/bmw_hydrogen_7.html) (accessed 23/05/14).
45. Hyundai, Hyundai ix35 Hydrogen Fuel Cell Vehicle. <http://www.hyundai.co.uk/about-us/environment/hydrogen-fuel-cell> (accessed 19/07/14).
46. Honda, FCX Clarity. <http://automobiles.honda.com/fcx-clarity/> (accessed 19/07/14).
47. Mercedes-Benz. The B-Class F-Cell. [http://www2.mercedes-benz.co.uk/content/unitedkingdom/mpc/mpc\\_unitedkingdom\\_website/en/home\\_mpc/passengercars/home/new\\_cars/models/b-class/\\_w246/fascination/b-class-f-cell.html](http://www2.mercedes-benz.co.uk/content/unitedkingdom/mpc/mpc_unitedkingdom_website/en/home_mpc/passengercars/home/new_cars/models/b-class/_w246/fascination/b-class-f-cell.html) (accessed 19/07/14).
48. Transport For London. Bus Investment. <http://www.tfl.gov.uk/campaign/bus-investment> (accessed 19/07/14).

49. Toyota. Future vehicles. <http://www.toyotaforklift.com/pages/about-us/toyota-philosophy/environmental-focus/future-vehicles.aspx> (accessed 23/05/14).
50. Netinform. Hydrogen Filling Stations Worldwide. <http://www.netinform.net/h2/h2stations/Default.aspx> (19/07/14).
51. Schlapbach, L. *Hydrogen in Intermetallic Compounds ii: Surface and Dynamic Properties, Applications*. Springer: 1992.
52. Lennard-Jones, J. E., Processes of Adsorption and Diffusion on Solid Surfaces. *T. Faraday Soc.* **1932**, 28, 333-359.
53. Züttel, A.; Wenger, P.; Sudan, P.; Mauron, P.; Orimo, S. I. Hydrogen Density in Nanostructured Carbon, Metals and Complex Materials. *Mater. Sci. Eng. B* **2004**, 108 (1), 9-18.
54. U.S. Department of Energy. *Targets for onboard hydrogen storage systems for light-duty vehicles*. [http://energy.gov/sites/prod/files/2014/03/f11/targets\\_onboard\\_hydro\\_storage\\_explanation.pdf](http://energy.gov/sites/prod/files/2014/03/f11/targets_onboard_hydro_storage_explanation.pdf) (accessed 22/05/14).
55. Cella. Clean, Safe, Low Cost Energy. <http://cellaenergy.com/> (accessed 19/07/14).
56. Sing, K. S. W.; Everett, D. H.; Haul, R. A. W.; Moscou, L.; Pierotti, R. A.; Rouquerol, J.; Siemieniewska, T. Reporting Physisorption Data for Gas/Solid Systems with Special Reference to the Determination of Surface Area and Porosity. *Pure and Applied Chemistry* **1985**, 57 (4), 603-619.
57. James, S. L. Metal-Organic Frameworks. *Chem. Soc. Rev.* **2003**, 32 (5), 276-288.
58. MacGillivray, L. R. *Metal-Organic Frameworks: Design and Application*. John Wiley & Sons, Inc.: 2010.
59. Lee, J.; Farha, O. K.; Roberts, J.; Scheidt, K. A.; Nguyen, S. T.; Hupp, J. T. Metal-Organic Framework Materials as Catalysts. *Chem. Soc. Rev.* **2009**, 38 (5), 1450-1459.

60. Farrusseng, D.; Aguado, S.; Pinel, C. Metal–Organic Frameworks: Opportunities for Catalysis. *Angew. Chem. Int. Edit.* **2009**, *48* (41), 7502-7513.
61. Armstrong, G. Gas Separation: Marvellous MOFs. *Nat Chem* **2008**, DOI:10.1038/nchem.41.
62. Li, J.-R.; Kuppler, R. J.; Zhou, H.-C. Selective Gas Adsorption and Separation in Metal-Organic Frameworks. *Chem. Soc. Rev.* **2009**, *38* (5), 1477-1504.
63. Ma, S.; Zhou, H.-C. Gas Storage in Porous Metal-Organic Frameworks for Clean Energy Applications. *Chem. Commun.* **2010**, *46* (1), 44-53.
64. Hirscher, M.; Panella, B. Hydrogen Storage in Metal–Organic Frameworks. *Scripta Mater.* **2007**, *56* (10), 809-812.
65. Fletcher, A. J.; Thomas, M.; Rosseinsky, M. J. Flexibility in Metal-Organic Framework Materials: Impact on Sorption Properties. *J. Solid State Chem.* **2005**, *178* (8), 2491-2510.
66. Millange, F.; Serre, C.; Guillou, N.; Férey, G.; Walton, R. I. Structural Effects of Solvents on the Breathing of Metal–Organic Frameworks: an In Situ Diffraction Study. *Angew. Chem. Int. Edit.* **2008**, *47* (22), 4100-4105.
67. Neimark, A. V.; Coudert, F. X.; Boutin, A.; Fuchs, A. H. Stress-Based Model for the Breathing of Metal–Organic Frameworks. *J. Phys. Chem. Lett.* **2009**, *1* (1), 445-449.
68. Farha, O. K.; Özgür Yazaydın, A.; Eryazici, I.; Malliakas, C. D.; Hauser, B. G.; Kanatzidis, M. G.; Nguyen, S. T.; Snurr, R. Q.; Hupp, J. T. De Novo Synthesis of a Metal–Organic Framework Material Featuring Ultrahigh Surface Area and Gas Storage Capacities. *Nat. Chem.* **2010**, *2* (11), 944-948.
69. Dagani, R. Crystal Sponges. <http://pubs.acs.org/cen/topstory/8003/8003notw1.html> (accessed 20/07/14).
70. Ströbel, R.; Garche, J.; Moseley, P. T.; Jörissen, L.; Wolf, G. Hydrogen Storage by Carbon Materials. *J. Power Sources* **2006**, *159* (2), 781-801.

71. Weinberger, B.; Darkrim Lamari, F. High Pressure Cryo-storage of Hydrogen by Adsorption at 77 K and up to 50 MPa. *Int. J. Hydrogen Energ.* **2009**, *34* (7) 3058-3064.
72. Puritas. Activated Carbon Products. [http://www.puritas.lk/activated\\_carbon.html](http://www.puritas.lk/activated_carbon.html) (accessed 19/07/14).
73. Yürüm, Y.; Taralp, A.; Veziroglu, T. N. Storage of Hydrogen in Nanostructured Carbon Materials. *Int. J. Hydrogen Energ.* **2009**, *34* (9), 3784-3798.
74. Reilly, R. M. Carbon Nanotubes: Potential Benefits and Risks of Nanotechnology in Nuclear Medicine. *J. Nucl. Med.* **2007**, *48* (7) 1039-1042.
75. Sevilla, M.; Foulston, R.; Mokaya, R. Superactivated Carbide-Derived Carbons with High Hydrogen Storage Capacity, *Energ. Environ. Sci.* **2010**, *3*, 223-227.
76. Sevilla, M.; Mokaya, R. Activation of Carbide-Derived Carbons: A Route to Materials with Enhanced Gas and Energy Storage Properties. *J. Mater. Chem.* **2011**, *21*, 4727-4723.
77. Dimitrakakis, G. K.; Tylianakis, E.; Froudakis, G. E. Pillared Graphene: A New 3-D Network Nanostructure for Enhanced Hydrogen Storage. *Nano Lett.* **2008**, *8* (10) 3166-3170.
78. Paul, R. K.; Ghazinejad, M.; Penchev, M.; Lin, J.; Ozkan, M.; Ozkan, C. S. Synthesis of a Pillared Graphene Nanostructure: A Counterpart of Three-Dimensional Carbon Architectures. *Small* **2010**, *6* (20), 2309-2313.
79. Wang, H.; Gao, Q.; Hu, J. High Hydrogen Storage Capacity of Porous Carbons Prepared by Using Activated Carbon. *J. Am. Chem. Soc.* **2009**, *131* (20), 7016-7022.
80. Yang, S. J.; Kim, T.; Im, J. H.; Kim, Y. S.; Lee, K.; Jung, H.; Park, C. R., MOF-Derived Hierarchically Porous Carbon with Exceptional Porosity and Hydrogen Storage Capacity. *Chem. Mater.* **2012**, *24* (3), 464-470.
81. Bekkum, H. V. *Introduction to Zeolite Science and Practice*. Elsevier: 2001.

82. Davis, M. E. Zeolites and Molecular Sieves: Not Just Ordinary Catalysts. *Ind. Eng. Chem. Res.* **1991**, *30* (8), 1675-1683.
83. Sand, L. B.; Mumpton, F. A. *Natural Zeolites: Occurrence, Properties, and Use*; Pergamon Press, Inc; Elmsford, NY, 1978.
84. Langmi, H. W.; Book, D.; Walton, A.; Johnson, S. R.; Al-Mamouri, M. M.; Speight, J. D.; Edwards, P. P.; Harris, I. R.; Anderson, P. A. Hydrogen Storage in Ion-Exchanged Zeolites. *J. Alloy. Compd.* **2005**, *404–406* (0), 637-642.
85. Falcioni, M.; Deem, M. W. A Biased Monte Carlo Scheme for Zeolite Structure Solution. *J. Chem. Phys.* **1999**, *110*(3), 1754-1766.
86. McKeown, N. B.; Budd, P. M. Polymers of Intrinsic Microporosity (PIMS): Organic Materials for Membrane Separations, Heterogeneous Catalysis and Hydrogen Storage. *Chem. Soc. Rev.* **2006**, *35* (8), 675-683.
87. Yuan, D.; Lu, W.; Zhao, D.; Zhou, H.-C. Highly Stable Porous Polymer Networks with Exceptionally High Gas-Uptake Capacities. *Adv. Mater.* **2011**, *23* (32), 3723-3725.
88. Verboeken, D.; Pérez-Ramírez, J. Towards a Sustainable Manufacture of Hierarchical Zeolites. *ChemSusChem* **2014**, *7* (3), 753-764.
89. Sevilla, M.; Fuertes, A. B. Sustainable Porous Carbons with a Superior Performance for CO<sub>2</sub> Capture. *Energ. Environ. Sci.* **2011**, *4*, 1756-1771.
90. White, R. J.; Budarin, V.; Luque, R.; Clark, J. H.; Macquarrie, D. J. Tuneable Porous Carbonaceous Materials from Renewable Resources. *Chem. Soc. Rev.* **2009**, *38* (12), 3401-3418.
91. White, C. M.; Steeper, R. R.; Lutz, A. E. The Hydrogen-Fueled Internal Combustion Engine: A Technical Review. *Int. J. Hydrogen Energ.* **2006**, *31* (10), 1292-1305.
92. Das, L. M. Hydrogen Engines: A View of the Past and a Look into the Future. *Int. J. Hydrogen Energ.* **1990**, *15* (6), 425-443.

93. De Boer, P. C. T.; McLean, W. J.; Homan, H. S. Performance and Emissions of Hydrogen Fueled Internal Combustion Engines. *Int. J. Hydrogen Energ.* **1976**, *1* (2), 153-172.
94. U.S. Department of Energy. Challenges in Fuel Economy. [http://www.fueleconomy.gov/feg/fcv\\_challenges.shtml](http://www.fueleconomy.gov/feg/fcv_challenges.shtml) (accessed 23/05/14).
95. EG&G Technical Services Incorporation, *Fuel Cell Handbook (sixth edition)*. DIANE Publishing: 2002.
96. Trimm, D. L.; Önsan, Z. I. Onboard Fuel Conversion for Hydrogen-Fuel-Cell-Driven Vehicles. *Cataly. Rev.* **2001**, *43* (1-2), 31-84.
97. Faur Ghenciu, A. Review of Fuel Processing Catalysts for Hydrogen Production in PEM Fuel Cell Systems. *Curr. Opin. Solid St. M.* **2002**, *6* (5), 389-399.
98. Cheng, X.; Shi, Z.; Glass, N.; Zhang, L.; Zhang, J.; Song, D.; Liu, Z.-S.; Wang, H.; Shen, J. A Review of PEM Hydrogen Fuel Cell Contamination: Impacts, Mechanisms, and Mitigation. *J. Power Sources* **2007**, *165* (2), 739-756.
99. Hino, R.; Yan, X. L. *Nuclear Hydrogen Production Handbook*. Taylor & Francis: 2011.
100. Mercedes-Benz News New B-class F-cell. <http://news.mercedes-benz.co.uk/company-news/new-b-class-f-cell-could-revolutionise-mobility-industry.html> (accessed 07/09).
101. Intergovernmental Panel on Climate Change, *Aviation and the Global Atmosphere*. Cambridge University Press: Cambridge, 1999.
102. Lee, D. S.; Fahey, D. W.; Forster, P. M.; Newton, P. J.; Wit, R. C. N.; Lim, L. L.; Owen, B.; Sausen, R. Aviation and Global Climate Change in the 21st Century. *Atmos. Environ.* **2009**, *43* (22–23), 3520-3537.
103. . Lee, D. S.; Pitari, G.; Grewe, V.; Gierens, K.; Penner, J. E.; Petzold, A.; Prather, M. J.; Schumann, U.; Bais, A.; Berntsen, T.; Iachetti, D.; Lim, L. L.; Sausen, R. Transport Impacts on Atmosphere and Climate: Aviation. *Atmos. Environ.* **2010**, *44* (37), 4678-4734.

104. Vissering, H., *Zeppelin: The Story of a Great Achievement (illustrated edition)*. Echo Library: Gloucestershire, 2011.
105. Tupolev. Cryogenic Aircraft - Development of Cryogenic Fuel Aircraft. <http://www.tupolev.ru/English/Show.asp?SectionID=82> (accessed 12/12).
106. Westenberger, A. *Cryoplane – Hydrogen Aircraft*, Hamburg, 2003.
107. Guynn, M. D.; Freh, J. E.; Olson, E. D. *Evaluation of a Hydrogen Fuel Cell Powered Blended-Wing-Body Aircraft Concept for Reduced Noise and Emissions*; NASA: Hampton, Virginia 2004.
108. Bradley, T. H.; Moffitt, B. A.; Thomas, R. W.; Mavris, D.; Parekh, D. E. Development and Experimental Characterization of a Fuel Cell Powered Aircraft. *J. Power Sources* **2007**, *171*, 793-801.
109. Fuel Cell Works. Dlr Motor Glider Antares Takes off in Hamburg – Powered by a Fuel Cell. <http://fuelcellsworks.com/news/2009/07/07/dlr-motor-glider-antares-takes-off-in-hamburg-%E2%80%93-powered-by-a-fuel-cell/> (accessed 01/02/2012).
110. EADS. EADS Zehst High-Speed Transport Concept Study. <http://www.eads.com/eads/int/en/our-innovation/our-technologies/Advanced-Concepts/ZEHST-concept.html> (accessed 10/09).
111. Jackson, R.; Haddox, C. Phantom Eye High Altitude Long Endurance Aircraft Unveiled. [http://www.boeing.com/Features/2010/07/bds\\_feat\\_phantom\\_eye\\_07\\_12\\_10.html](http://www.boeing.com/Features/2010/07/bds_feat_phantom_eye_07_12_10.html) (accessed 26/01).
112. European Commission. World Records For EU-Funded Fuel Cell Powered Aircraft. [http://ec.europa.eu/research/transport/projects/items/world\\_records\\_for\\_eu\\_funded\\_fuel\\_cell\\_powered\\_aircraft\\_en.htm](http://ec.europa.eu/research/transport/projects/items/world_records_for_eu_funded_fuel_cell_powered_aircraft_en.htm) (accessed 01/02/2012).
113. AV. Aerovironment Stratospheric Persistent UAS: Global observer. [http://www.avinc.com/uas/stratospheric/global\\_observer/](http://www.avinc.com/uas/stratospheric/global_observer/) (accessed 01/02/2012).
114. Lange Aviation. Antares H3 - Lange and DLR Develop Second Generation Fuel-Cell Powered Aircraft. [http://www.lange-aviation.com/htm/english/products/antares\\_h3/antares\\_h3.html](http://www.lange-aviation.com/htm/english/products/antares_h3/antares_h3.html) (accessed 01/02/2012).

115. Daggett, D. L.; Hendricks, R. C.; Walther, R.; Corporan, E. *Alternative Fuels for use in Commercial Aircraft*, American Institute of Aeronautics and Astronautics: 2007.
116. Nojoumi, H.; Dincer, I.; Naterer, G. F. Greenhouse Gas Emissions Assessment of Hydrogen and Kerosene-Fueled Aircraft Propulsion. *Int. J. Hydrogen Energ.* **2009**, *34* (3), 1363-1369.
117. Lee, J. J. Can We Accelerate the Improvement of Energy Efficiency in Aircraft Systems? *Energ. Convers. Manage.* **2010**, *51* (1), 189-196.
118. Schumann, U. Formation, Properties and Climatic Effects of Contrails. *C. R. Phys.* **2005**, *6* (4-5), 549-565.
119. Ahluwalia, R K.; Peng, J K. Automotive Hydrogen Storage System Using Cryo-Adsorption on Activated Carbon. *Int. J. Hydrogen Energ.* **2009**, *34*, 5476-5487.
120. Hardy, B.; Corgnale, C.; Chahine, R.; Richard, M.A.; Garrison, S.; Tamburello, D.; Cossement, D.; Anton, D. Modeling of Adsorbent Based Hydrogen Storage Systems. *Int. J. Hydrogen Energ.* **2012**, *37* (7) 5691-5705.
121. Richard, M. A.; Bénard, P.; Chahine, R., Gas Adsorption Process in Activated Carbon over a Wide Temperature Range Above the Critical Point. Part 1: Modified Dubinin-Astakhov Model. *Adsorption* **2009**, *15* (1), 43-51.
122. Bénard, P.; Chahine, R. Modeling of Adsorption Storage of Hydrogen on Activated Carbons. *Int. J. Hydrogen Energ.* **2001**, *26* (8), 849-855.
123. Poirier, E.; Chahine, R.; Bose, T. K. Hydrogen adsorption in carbon nanostructures. *Int. J. Hydrogen Energ.* **2001**, *26* (8), 831-835.
124. Poirier, E.; Chahine, R.; Bénard, P.; Lafi, L.; Dorval-Douville, G.; Chandonia, P. A. Hydrogen Adsorption Measurements and Modeling on Metal-Organic Frameworks and Single-Walled Carbon Nanotubes. *Langmuir* **2006**, *22* (21), 8784-8789.

125. Bénard, P.; Chahine, R.; Chandonia, P. A.; Cossement, D.; Dorval-Douville, G.; Lafi, L.; Lachance, P.; Paggiaro, R.; Poirier, E. Comparison of Hydrogen Adsorption on Nanoporous Materials. *J. Alloy. Compd.* **2007**, *446*, 380-384.
126. Panella, B.; Hirscher, M.; Roth, S. Hydrogen Adsorption in Different Carbon Nanostructures. *Carbon* **2005**, *43* (10), 2209-2214.
127. Benard, P.; Chahine, R. Modeling of High-Pressure Adsorption Isotherms Above the Critical Temperature on Microporous Adsorbents: Application to Methane. *Langmuir* **1997**, *13* (4), 808-813.
128. Richard, M. A.; Bénard, P.; Chahine, R. Gas Adsorption Process in Activated Carbon over a Wide Temperature Range Above the Critical Point. Part 2: Conservation of Mass and Energy. *Adsorption* **2009**, *15* (1), 53-63.
129. Poirier, E.; Dailly, A. Investigation of the Hydrogen State in IRMOF-1 from Measurements and Modeling of Adsorption Isotherms at High Gas Densities. *J. Phys. Chem. C* **2008**, *112* (33) 13047-13052.
130. Poirier, E.; Dailly, A. Thermodynamics of Hydrogen Adsorption in MOF-177 at Low Temperatures: Measurements and Modelling. *Nanotechnology* **2009**, *20* (20), 204006.
131. Poirier, E.; Dailly, A. Thermodynamic Study of the Adsorbed Hydrogen Phase in Cu-Based Metal-Organic Frameworks at Cryogenic Temperatures. *Energ. Environ. Sci.* **2009**, *2* (4), 420-425.
132. Poirier, E.; Dailly, A. On the Nature of the Adsorbed Hydrogen Phase in Microporous Metal–Organic Frameworks at Supercritical Temperatures. *Langmuir* **2009**, *25* (20), 12169-12176.
133. Dailly, A.; Poirier, E. Evaluation of an Industrial Pilot Scale Densified MOF-177 Adsorbent as an On-Board Hydrogen Storage Medium. *Energ. Environ. Sci.* **2011**, *4* (9), 3527-3534.
134. Poirier, E.; Dailly, A. Saturation Properties of a Supercritical Gas Sorbed in Nanoporous Materials. *Phys. Chem. Chem. Phys.* **2012**, *14* (48), 16544-16551.

135. Langmuir, I. The Adsorption of Gases on Plane Surfaces of Glass, Mica and Platinum. *J. Am. Chem. Soc.* **1918**, 40 (9), 1361-1403.
136. Arrhenius, S. Über die Reaktionsgeschwindigkeit bei der Inversion von Rohrzucker Durch Säuren. *Z. Physik. Chem.* **1889**, 4, 226.
137. Do, D. D. *Adsorption Analysis: Equilibria and Kinetics*. Imperial College Press: 1998; Vol. 2.
138. Jaroniec, M.; Madey, R. *Physical adsorption on heterogeneous solids*. Elsevier: 1988.
139. Rouquerol, J.; Rouquerol, F.; Sing, K. S. W. *Absorption by Powders and Porous Solids*. Elsevier Science: 1998.
140. Glasstone, S. and Lewis, D. *Elements of Physical Chemistry*. New York : Van Nostrand, 1954.
141. Sips, R. On the structure of a catalyst surface. *J. Chem. Phys.* **1948**, 16, 490-495.
142. Toth, J. Gas-Dampf-Adsorption an Festen Oberflächen Inhomogener Aktivitäten. *Acta Chim. Acad. Sci. Hung.* **1962**, 30.
143. Gibbs, J. W. *The Collected Works of J. Willard Gibbs*; Longmans & Co., New York, 1928.
144. Rouquerol, F.; Rouquerol, J.; Sing, K. S. W. *Adsorption by Powders and Porous Solids: Principles, Methodology, and Applications*; Academic Press; San Diego, 1999.
145. Stolten, D. *Hydrogen and Fuel Cells: Fundamentals, Technologies and Applications*; John Wiley & Sons, 2010.
146. Neimark, A. V.; Ravikovitch, P. I. Calibration of Pore Volume in Adsorption Experiments and Theoretical Models. *Langmuir* **1997**, 13, 5148-5160.
147. Bimbo, N.; Ting, V. P.; Hruzewicz-Kolodziejczyk, A.; Mays, T. J. Analysis of Hydrogen Storage in Nanoporous Materials for Low Carbon Energy Applications. *Faraday Discuss.* **2011**, 151. 59-74.

148. Furukawa, H.; Miller, M. A.; Yaghi, O. M. Independent Verification of the Saturation Hydrogen Uptake in MOF-177 and Establishment of a Benchmark for Hydrogen Adsorption in Metal–Organic Frameworks. *J. Mater. Chem.* **2007**, *17* (30) 3197-3204.
149. Zhou, L.; Zhou, Y.; Sun, Y. Studies on the Mechanism and Capacity of Hydrogen Uptake by Physisorption-Based Materials. *Int. J. hydrogen energ.* **2006**, *31* (2) 259-264.
150. British Standards Institution. *Determination of the Specific Surface Area of Powders- Part 1: BET Method of Gas Adsorption for Solids (Including Porous Materials)*; [BS 4359-1, ISO 9277:1995] British Standards Institution: 1996.
151. Hruzewicz-Kołodziejczyk, A.; Ting, V. P.; Bimbo, N.; Mays, T. J. Improving Comparability of Hydrogen Storage Capacities of Nanoporous Materials. *Int. J. Hydrogen Energ.* **2012**, *37* (3), 2728-2736.
152. Dubinin, M. M. *Progress in Surface and Membrane Science*, Cadenhead, D. A., Ed.; Academic Press: New York, 1975.
153. Olivier, J. P., Modeling Physical Adsorption on Porous and Nonporous Solids Using Density Functional Theory. *J. Porous Mat.* **1995**, *2*, 9-17.
154. Kaganer, M. G. New Method for Determining the Specific Surface of Adsorbents and Other Finely Divided Substances. *Russ. J. Phys. Chem.* **1959**, *33* (10), 352-356.
155. Yao, J.; Zhao, L.; Fan, Z. H.; Zhou, Y. In *Estimation of Pore Size Distribution By CO<sub>2</sub> Adsorption and its Applications in Physical Activation of Precursors*, Adsorption Science and Technology: Proceedings of the Second Pacific Basin Conference on Adsorption Science and Technology, Brisbane, Australia, Do, D. D., Ed.; World Scientific: Brisbane, Australia, 2000.
156. Jiang, D.; Burrows, A. D.; Edler, K. J. Size-Controlled Synthesis of MIL-101(Cr) Nanoparticles with Enhanced Selectivity for CO<sub>2</sub> over N<sub>2</sub>. *Cryst. Eng. Comm.* **2011**, *13* (23), 6916-6919.

157. Hamon, L.; Serre, C.; Devic, T.; Loiseau, T.; Millange, F.; Férey, G.; De Weireld, G. Comparative Study of Hydrogen Sulfide Adsorption in the MIL-53(Al, Cr, Fe), MIL-47(V), MIL-100(Cr), and MIL-101(Cr) Metal-Organic Frameworks at Room Temperature. *J. Am. Chem. Soc.* **2009**, *131* (25), 8775-8777.
158. Férey, G.; Mellot-Draznieks, C.; Serre, C.; Millange, F.; Dutour, J.; Surblé, S.; Margiolaki, I. A Chromium Terephthalate-Based Solid with Unusually Large Pore Volumes and Surface Area. *Science* **2005**, *309* (5743), 2040-2042.
159. Latroche, M.; Surble, S.; Serre, C.; Mellot-Draznieks, C.; Llewellyn, P. L.; Lee, J-H.; Chang, J-S.; Jhung, S. H.; Férey, G. Hydrogen Storage in the Giant-Pore Metal-Organic Frameworks MIL-100 and MIL-101. *Angew. Chem. Int. Edit.* **2006**, *45* (48) 8227-8231.
160. Loiseau, T.; Serre, C.; Huguenard, C.; Fink, G.; Taulelle, F.; Henry, M.; Bataille, T.; Férey, G. A Rationale for the Large Breathing of the Porous Aluminum Terephthalate (MIL-53) upon Hydration. *Chem. Eur. J.* **2004**, *10* (6), 1373-1382.
161. Boutin, A.; Springuel-Huet, M.-A.; Nossov, A.; Gédéon, A.; Loiseau, T.; Volkringer, C.; Férey, G.; Coudert, F.-X.; Fuchs, A. H. Breathing Transitions in MIL-53(Al) Metal–Organic Framework upon Xenon Adsorption. *Angew. Chem. Int. Edit.* **2009**, *48* (44), 8314-8317.
162. Serre, C.; Burrelly, S.; Vimont, A.; Ramsahye, N. A.; Maurin, G.; Llewellyn, P. L.; Daturi, M.; Filinchuk, Y.; Leynaud, O.; Barnes, P.; Férey, G. An Explanation for the Very Large Breathing Effect of a Metal–Organic Framework During CO<sub>2</sub> Adsorption. *Adv. Mater.* **2007**, *19* (17), 2246-2251.
163. Neimark, A. V.; Coudert, F. o.-X.; Triguero, C.; Boutin, A.; Fuchs, A. H.; Beurroies, I.; Denoyel, R. Structural Transitions in MIL-53 (Cr): View from Outside and Inside. *Langmuir* **2011**, *27* (8), 4734-4741.
164. Liu, Y.; Her, J.-H.; Dailly, A.; Ramirez-Cuesta, A. J.; Neumann, D. A.; Brown, C. M. Reversible Structural Transition in MIL-53 with Large Temperature Hysteresis. *J. Am. Chem. Soc.* **2008**, *130* (35), 11813-11818.

165. Voskuilen, T. G.; Pourpoint, T. L.; Dailly, A. M. Hydrogen Adsorption on Microporous Materials at Ambient Temperatures and Pressures up to 50 MPa. *Adsorption* **2012**, *18* (3-4) 239-249.
166. Lin, X.; Jia, J.; Zhao, X.; Thomas, K. M.; Blake, A. J.; Walker, G. S.; Champness, N. R.; Hubberstey, P.; Schröder, M. High H<sub>2</sub> Adsorption by Coordination-Framework Materials. *Angew. Chem. Int. Edit.* **2006**, *45* (44), 7358-7364.
167. Park, K. S.; Ni, Z.; Côté, A. P.; Choi, J. Y.; Huang, R.; Uribe-Romo, F. J.; Chae, H. K.; O'Keeffe, M.; Yaghi, O. M. Exceptional Chemical and Thermal Stability of Zeolitic Imidazolate Frameworks. *P. Natl. A. Sci.* **2006**, *103* (27), 10186-10191.
168. Zhou, W.; Wu, H.; Hartman, M. R.; Yildirim, T. Hydrogen and Methane Adsorption in Metal–Organic Frameworks: A high-Pressure Volumetric Study. *J. Phys. Chem. C* **2007**, *111* (44), 16131-16137.
169. Warren, B. E., *X-Ray Diffraction*; Courier Dover Publications, 1969.
170. Bragg, W. H., & Bragg, W. L. The Reflection of X-Rays by Crystals. *P. R. Soc. Lond. Ser. A* **1913**, *88* (605), 428-438.
171. Brunauer, S.; Emmett, P. H.; Teller, E. Adsorption of Gases in Multimolecular Layers. *J. Am. Chem. Soc.* **1938**, *60* (2), 309-319.
172. Mantid. Mantid <http://www.mantidproject.org> (accessed 09/06/14).
173. Marquardt, D. W. An Algorithm for Least-Squares Estimation of Nonlinear Parameters. *J. Soc. Ind. Appl. Math.* **1963**, *11* (2), 431-441.
174. Gavin, H. *The Levenberg-Marquardt Method for Nonlinear Least Squares Curve-Fitting Problems*; Duke University: Durham, NC, 2011.
175. Arfken, G. The Method of Steepest Descents. In *Mathematical Methods for Physicists*, 3rd ed., Academic Press: Orlando, FL, 1985; pp 428-436.
176. Nelder, J. A.; Mead, R. A Simplex Method for Function Minimization. *Comput. J.* **1965**, *7*, 308-313.

177. Tatham, S., *PuTTY*, 2013 [Computer software] Available from: <http://www.chiark.greenend.org.uk/~sgtatham/putty/> (accessed 19/01/14).
178. Microsoft., Microsoft Visual Studio, 2008 [Computer software] Available from: <http://www.microsoft.com/en-us/download/details.aspx?id=7873> (accessed 19/01/14).
179. Přikryl, M., WinSCP, 2013 [Computer software] Available from: <http://winscp.net/eng/index.php> (accessed 19/01/14).
180. Cohen, J.; Gullingsrud, J.; Stone, J., Visual Molecular Dynamics, 2012 [Computer software] Available from: <http://www.ks.uiuc.edu/Research/vmd/> (accessed 19/01/14).
181. Cracknell, R. F. Molecular Simulation of Hydrogen Adsorption in Graphitic Nanofibres. *Phys. Chem. Chem. Phys.* **2001**, 3 (11), 2091-2097.
182. Rowland, R. S.; Taylor, R. Intermolecular Nonbonded Contact Distances in Organic Crystal Structures: Comparison with Distances Expected from van der Waals Radii. *J. Phys. Chem.* **1996**, 100 (18) 7384-7391.
183. Sharpe, J. E.; Bimbo, N.; Ting, V. P.; Burrows, A. D.; Jiang, D.; Mays, T. J. Supercritical Hydrogen Adsorption in Nanostructured Solids with Hydrogen Density Variation in Pores. *Adsorption* **2013**, 19 (2-4), 643-652.
184. Wang, Q.; Johnson, J. K. Molecular Simulation of Hydrogen Adsorption in Single-Walled Carbon Nanotubes and Idealized Carbon Slit Pores. *J. Chem. Phys.* **1999**, 110 (1) 577-586.
185. Wang, Q.; Johnson, J. K. Computer Simulations of Hydrogen Adsorption on Graphite Nanofibers. *J. Phys. Chem. B* **1998**, 103 (2), 277-281.
186. Zhang, X.; Cao, D.; Chen, J. Hydrogen Adsorption Storage on Single-Walled Carbon Nanotube Arrays by a Combination of Classical Potential and Density Functional Theory. *J. Phys. Chem. B* **2003**, 107 (21), 4942-4950.
187. Laudisio, G.; Dash, R.K.; Singer, J.P.; Yushin, G.; Gogotsi, Y.; Fischer, J.E. Carbide-Derived Carbons: A Comparative Study of Porosity Based on Small-Angle Scattering and Adsorption Isotherms. *Langmuir*, **2006**, 22, 8945-8950.

188. Yushin, G.; Dash, R.; Jagiello, J.; Fischer, J.E.; Gogotsi, Y. Carbide-Derived Carbons: Effect of Pore Size on Hydrogen Uptake and Heat of Adsorption. *Adv. Funct. Mater.* **2006**, *16*, 2288-2293.
189. Yang, Z. X.; Xia, Y. D.; Mokaya, R. Enhanced Hydrogen Storage Capacity of High Surface Area Zeolite-like Carbon Materials. *J. Am. Chem. Soc.* **2007**, *129*, 1673-1679.
190. Leachman, J. W.; Jacobsen, R. T.; Penoncello, S. G.; Lemmon, E. W. Fundamental Equations of State for Parahydrogen, Normal Hydrogen, and Orthohydrogen *J. Phys. Chem. Ref. Data* **2009**, *38* (721).
191. Lemmon, E. W.; Huber, M. L.; McLinden, M. O. NIST Standard Reference Database 23: Reference Fluid Thermodynamic and Transport Properties - REFPROP, Version 8.0., National Institute of Standards and Technology, Standard Reference Data Program, Gaithersburg, 2007.
192. National Institute of Standards and Technology, 2011, NIST Chemistry WebBook. <http://webbook.nist.gov/> (accessed 28/05/14).
193. Bimbo, N.; Ting, V. P.; Sharpe, J. E.; Mays, T. J. Analysis of Optimal Conditions for Adsorptive Hydrogen Storage in Microporous Solids. *Colloid. Surface. A* **2013**, *437*, 113-119.
194. Broom, D. P. *Hydrogen Storage Materials: The Characterisation of their Storage Properties*; Springer; London, 2011.
195. Züttel, A., Sudan, P., Mauron, P. & Wenger, P. Model for the Hydrogen Adsorption on Carbon Nanostructures. *Appl. Phys. A-Mater.* **2004**, *78*, 941-946.
196. Saha, D.; Wei, Z.; Deng, S. Equilibrium, Kinetics and Enthalpy of Hydrogen Adsorption in MOF-177. *Int. J. Hydrogen Energ.* **2008**, *33* (24), 7479-7488.
197. Saha, D.; Zacharia, R.; Lafi, L.; Cossement, D.; Chahine, R. Synthesis, Characterization and Hydrogen Adsorption on Metal-Organic Frameworks Al, Cr, Fe and Ga-BTB. *Chem. Eng. J.* **2011**, *171* (2), 517-525.
198. Lin, X.; Telepeni, I.; Blake, A. J.; Dailly, A.; Brown, C. M.; Simmons, J. M.; Zoppi, M.; Walker, G. S.; Thomas, M.; Mays, T. J.; Hubberstey, P.; Champness, N.

- R.; Shroder, M. High Capacity Hydrogen Adsorption in Cu(II) Tetracarboxylate Framework Materials: The Role of Pore Size, Ligand Functionalization, and Exposed Metal Sites. *J. Am. Chem. Soc.* **2009**, *131* (6), 2159-2171.
199. Kaye, S. S.; Long, J. R. Hydrogen Storage in the Dehydrated Prussian Blue Analogues  $M_3[Co(CN)_6]_2$  (M = Mn, Fe, Co, Ni, Cu, Zn). . *J. Am. Chem. Soc.* **2005**, *127* (18), 6506-6507.
200. Encyclopaedia Britannica. Ockham's razor. <http://www.britannica.com/EBchecked/topic/424706/Ockhams-razor> (accessed 13/09).
201. Freundlich, H., *Colloid and Capillary Chemistry*. Methuen and Co. Ltd.; London, 3rd. Edn. 1926.
202. Sips, R., On the structure of a catalyst surface. li. *J. Chem. Phys.* **1950**, *18* (8).
203. Quiñones, I.; Guiochon, G. Derivation and Application of a Jovanovic–Freundlich Isotherm Model for Single-Component Adsorption on Heterogeneous Surfaces. *J. Colloid Interf. Sci.* **1996**, *183* (1), 57-67.
204. Jovanovic, D. S. Physical Adsorption of Gases. 1. Isotherms for Monolayer and Multilayer Adsorption. *Colloid Polym. Sci.* **1970**, *235*, 1203-1214.
205. Dubinin, M. M.; Zaverina, E. D.; Radushkevich, L. V. Sorption and Structure of Active Carbons. I. Adsorption of Organic Vapors. *Zh. Fiz. Khimii* **1947**, *21*, 1351-1362.
206. Amankwah, K.A.G.; Schwarz, J.A. A Modified Approach for Estimating Pseudo-Vapor Pressure in the Application of the Dubinin-Astakhov Equation. *Carbon* **1995**, *33*. 1313-1319.
207. Hu, X.; Do, D. D. Effect of Surface Energetic Heterogeneity on the Kinetics of Adsorption of Gases in Microporous Activated Carbon. *Langmuir* **1993**, *9* (10), 2530-2536.
208. Wilson, M. C.; Galwey, A. K. Compensation Effect in Heterogeneous Catalytic Reactions Including Hydrocarbon Formation on Clays. *Nature* **1973**, *243* (5407), 402-404.

209. McPherson, G. *Applying and interpreting statistics: A comprehensive guide*. Springer: 2001.
210. Silvera, I. F. The Solid Molecular Hydrogens in the Condensed Phase: Fundamentals and Static Properties. *Rev. Mod. Phys.* **1980**, 52 (2), 393.
211. Hyndman, R. J.; Koehler, A. B., Another Look at Measures of Forecast Accuracy. *Int. J. Forecasting* **2006**, 22 (4), 679-688.
212. Sartbaeva, A.; Wells, S. A.; Treacy, M. M. J.; Thorpe, M. F. The Flexibility Window in Zeolites. *Nat. Mater.* **2006**, 5, 962-965.
213. Boutin, A.; Coudert, F.-X.; Springuel-Huet, M.-A.; Neimark, A. V.; Férey, G.; Fuchs, A. H. The Behaviour of Flexible MIL-53(Al) upon CH<sub>4</sub> and CO<sub>2</sub> Adsorption. *J. Phys. Chem. C* **2010**, 114, 22237-22244.
214. Férey, G.; Latroche, M.; Serre, C.; Millange, F.; Loiseau, T.; Percheron-Guégan, A. Hydrogen Adsorption in the Nanoporous Metal-Benzenedicarboxylate M(OH)(O<sub>2</sub>C-C<sub>6</sub>H<sub>4</sub>-CO<sub>2</sub>)(M= Al<sup>3+</sup>, Cr<sup>3+</sup>), MIL-53. *Chem. Comm.* **2003**, 24, 2976-2977.
215. Lee, H.; Choi, Y. N.; Choi, S. B.; Kim, J.; Kim, D.; Jung, D. H.; Park, Y. S.; Yoon, K. B. Liquid-Like Hydrogen Stored in Nanoporous Materials at 50 K Observed by in Situ Neutron Diffraction Experiments. *J. Phys. Chem. C* **2013**, 117 (6), 3177-3184
216. Clayton, D., *Handbook of Isotopes in the Cosmos: Hydrogen to Gallium*; Cambridge University Press, 2003.
217. Celotta, R. *Neutron Scattering*. Price, D. L.; Skold, K. Ed.; Academic Press, 1987.
218. Angelo, J. A. *Nuclear Technology*; Greenwood Publishing Group, 2004.
219. Squires, G. L. *Introduction to the Theory of Thermal Neutron Scattering*; Cambridge University Press; Cambridge, 1978.
220. Ramirez-Cuesta, A. J.; Jones, M. O.; David, W. I. F. Neutron Scattering and Hydrogen Storage. *Mater. Today* **2009**, 12, 54-61.

221. Mitchell, P. C. H.; Parker, S. F.; Ramirez-Cuesta, A.; Tomkinson, J. *Vibrational Spectroscopy with Neutrons: with Applications in Chemistry, Biology, Materials Science and Catalysis. Series on Neutron Techniques and Applications*; World Scientific; Hackensack, NJ, 2005.
222. Ting, V. P.; Ramirez-Cuesta, A. J.; Bimbo, N.; Sharpe, J. E.; Mays, T. J., Direct Evidence for Accumulation of Solid-like H<sub>2</sub> in a Microporous Hydrogen Storage Material. *Nature Communications* (to be submitted)
223. Wang, Q.; Johnson, J. K. Computer Simulations of Hydrogen Adsorption on Graphite Nanofibers. *J. Phys. Chem. B* **1998**, *103* (2), 277-281.
224. Jagiello, J.; Ansón, A.; Martínez, M. T. DFT-Based Prediction of High-Pressure H<sub>2</sub> Adsorption on Porous Carbons at Ambient Temperatures from Low-Pressure Adsorption Data Measured at 77 K. *J. Phys. Chem. B* **2006**, *110* (10), 4531-4534.
225. Metropolis, N. The Beginning of the Monte Carlo Method. *Los Alamos Science*, **1987**, *15* (584), 125-130.
226. Frenkel, D.; Smit, B. *Understanding Molecular Simulation: From Algorithms to Applications*; Academic Press, 2001.
227. Newman, M. E. J.; Barkema, G. T. *Monte Carlo Methods in Statistical Physics*; Clarendon Press; Oxford University Press, Oxford, New York, 1999.
228. Yang, Q.; Zhong, C. Understanding Hydrogen Adsorption in Metal-Organic Frameworks with Open Metal Sites: A Computational Study. *J. Phys. Chem. B* **2006**, *110* (2), 655-658.
229. Wang, Q.; Johnson, J. K. Molecular Simulation of Hydrogen Adsorption in Single-Walled Carbon Nanotubes and Idealized Carbon Slit Pores. *J. Chem. Phys.* **1999**, *110* (1), 577-586.
230. Wang, Q.; Johnson, J. K. Optimization of Carbon Nanotube Arrays for Hydrogen Adsorption. *J. Phys. Chem. B* **1999**, *103* (23), 4809-4813.

231. Simonyan, V. V.; Diep, P.; Johnson, J. K. Molecular Simulation of Hydrogen Adsorption in Charged Single-Walled Carbon Nanotubes. *J. Chem. Phys.* **1999**, *111* (21), 9778-9783.
232. Cheng, J.; Yuan, X.; Zhao, L.; Huang, D.; Zhao, M.; Dai, L.; Ding, R. GCMC Simulation of Hydrogen Physisorption on Carbon Nanotubes and Nanotube Arrays. *Carbon* **2004**, *42* (10), 2019-2024.
233. Batsanov, S. S. Van der Waals Radii of Elements. *Inorg. Mater.* **2001**, *37* (9), 871-885.
234. Tascón, J. M., ed. *Novel carbon adsorbents*; Elsevier, 2012.
235. Hosseini, M.; Dincer, I.; Naterer, G. F.; Rosen, M.A. Thermodynamic Analysis of Filling Compressed Gaseous Hydrogen Storage Tanks. *Int. J. Hydrogen Energ.* **2012**, *37* (6), 5063-5071.
236. Demirel, Y. *Energy: Production, Conversion, Storage, Conservation, and Coupling*; Springer 2012.
237. Al-Hallaj, S.; Kiszynski, K. *Hybrid Hydrogen Systems: Stationary and Transportation Applications*; Springer 2011.
238. Goswami, D. Y.; Kreith, F. *Energy Conversion*; Taylor & Francis 2007.
239. DOE Hydrogen and Fuel Cells Program Record. Energy Requirements for Hydrogen Gas Compression and Liquefaction as Related to Vehicle Storage Needs. [http://www.hydrogen.energy.gov/pdfs/9013\\_energy\\_requirements\\_for\\_hydrogen\\_gas\\_compression.pdf](http://www.hydrogen.energy.gov/pdfs/9013_energy_requirements_for_hydrogen_gas_compression.pdf) (accessed 12/08/14).
240. Richard, M. A.; Cossement, D.; Chandonia, P. A.; Chahine, R.; Mori, D.; Hirose, K. Preliminary Evaluation of the Performance of an Adsorption-Based Hydrogen Storage System. *AIChE J.* **2009**, *55* (11), 2985-2996.
241. Vasiliev, L. L.; Kanonchik, L. E.; Kulakov, A. G.; Babenko, V. A. Hydrogen Storage System Based on Novel Carbon Materials and Heat Pipe Heat Exchanger. *Int. J. Therm. Sci.* **2007**, *46* (9), 914-925.

242. Ye, F.; Xiao, J.; Hu, B.; Benard, P.; Chahine, R. Implementation for Model of Adsorptive Hydrogen Storage Using UDF in Fluent. *Physics Procedia* **2012**, *24*, 793-800.
243. Xiao, J.; Liu, Y.; Wang, J.; Bénard, P.; Chahine, R. Finite Element Simulation of Heat and Mass Transfer in Activated Carbon Hydrogen Storage Tank. *Int. J. Heat Mass Tran.* **2012**, *55* (23), 6864-6872.
244. Xiao, J.; Yang, H.; Cossement, D.; Bénard, P.; Chahine, R. Improvement of Heat Transfer Model for Adsorptive Hydrogen Storage System. *Int. J. Hydrogen Energ.* **2013**, *38* (25), 10889-10895.
245. Xiao, J.; Zhou, Z.; Cossement, D.; Bénard, P.; Chahine, R. Lumped Parameter Model for Charge–Discharge Cycle of Adsorptive Hydrogen Storage System. *Int. J. Heat Mass Tran.* **2013**, *64*, 245-253.
246. Xiao, J.; Hu, M.; Bénard, P.; Chahine, R., Simulation of Hydrogen Storage Tank Packed with Metal-Organic Framework. *Int. J. Hydrogen Energ.* **2013**, *38* (29), 13000-13010.
247. Farmahini, A. H.; Opletal, G.; & Bhatia, S. K. Structural Modelling of Silicon Carbide-Derived Nanoporous Carbon by Hybrid Reverse Monte Carlo Simulation. *J. Phys. Chem. C* **2013**, *117* (27), 14081-14094.

## **Supplementary information (in electronic format)**

### **Supplementary Information A**

An explanation of the methodology used to calculate the compressibility factor,  $Z$ .

### **Supplementary Information B**

A comparison of the initial and the developed models when using the other isotherm equations within the DV model on the isotherms of the TE7 carbon beads, and for when using the Tóth model on the isotherms of the other materials.

### **Supplementary Information C**

Further information on the Unilan- $b$  equation.

### **Supplementary Information D**

Residuals and bias when comparing the use of different isotherm equations within the DV model.

### **Supplementary Information E**

Global fits for all of the materials when comparing the use of different isotherm equations within the DV model.

### **Supplementary Information F**

Fits of the DV model on isotherms of the TE7 carbon beads and MIL-53, when introducing different pore volume dependencies within the DV model.

### **Supplementary Information G**

Fits of the DV model on isotherms of the TE7 carbon beads and MIL-101, when introducing different adsorbate density dependencies within the DV model.

### **Supplementary Information H**

Design curves per unit volume and per unit mass for all of the materials.